

Electronic Thesis and Dissertation Repository

---

8-24-2020 11:00 AM

## Parametric Study of the Cutting Process and Surface Formation during Elliptical Vibration Assisted Single Point Cutting

Nikolai D. Farrus, *The University of Western Ontario*

Supervisor: Tutunea-Fatan, Remus, *The University of Western Ontario*

Co-Supervisor: Bordatchev, Evgueni, *National Research Council of Canada*

A thesis submitted in partial fulfillment of the requirements for the Master of Engineering Science degree in Mechanical and Materials Engineering

© Nikolai D. Farrus 2020

Follow this and additional works at: <https://ir.lib.uwo.ca/etd>



Part of the [Manufacturing Commons](#)

---

### Recommended Citation

Farrus, Nikolai D., "Parametric Study of the Cutting Process and Surface Formation during Elliptical Vibration Assisted Single Point Cutting" (2020). *Electronic Thesis and Dissertation Repository*. 7242. <https://ir.lib.uwo.ca/etd/7242>

This Dissertation/Thesis is brought to you for free and open access by Scholarship@Western. It has been accepted for inclusion in Electronic Thesis and Dissertation Repository by an authorized administrator of Scholarship@Western. For more information, please contact [wlsadmin@uwo.ca](mailto:wlsadmin@uwo.ca).

## **Abstract**

Elliptical vibration cutting has enabled the fabrication of numerous functional surfaces such as optical quality surface finishes, micro/nano surface texturing, and improved cutting force reduction on ferrous and other hard-to-cut materials. This wide range of capabilities comes from the high-frequency elliptical vibrations produced at the tool tip, ultimately introducing discontinuous contact between the cutting tool and workpiece. However, despite the relative use of this technology, there has been limited investigation on the overarching parametric influence that its cutting parameters have on process outcomes such as cutting forces and surface roughness formation.

The current thesis addresses this research gap with the development of a parametric study for elliptical vibration assisted single point cutting. More specifically, the study encompasses analytical, experimental and finite element method analyses of the cutting forces and surface roughness. Ultimately, the results indicate the functional dependence between elliptical vibration process parameters and the resulting cutting forces and surface roughness. Cumulatively, this contribution enables effective recommendations for future enhancements involving user-required cutting force reduction and/or surface quality improvements.

## **Keywords**

Elliptical vibration cutting, single point cutting, microfabrication, process parameters, cutting forces, surface topography, V-grooves, parametric study, finite element analysis.

## Summary for Lay Audience

Various surface functionalities such as the control of friction, wettability, aerodynamics, and aesthetics have demonstrated the attributes of high-quality/precision parts. Such tooling components are demanded in fields such as automotive, biomedical, defense, aerospace, photonics, and security applications. Therefore, cost-effective ultra-precision microfabrication technologies for micro/nano-texturing and structuring of functional surfaces are typically regarded as both a “key enabler” and a “game changer” in today’s knowledge-driven advanced manufacturing. Along these lines, elliptical vibration assisted single point cutting (EVASPC) is one of the emerging technologies that relies on intermittent contact between the tool and workpiece, facilitating the generation of high quality surfaces on ferrous and/or hard-to-cut materials, and accounts for reduced cutting forces, surface roughness, tool wear, and enhanced free-form surface accuracy, to name a few.

Elliptical vibration cutting has enabled the fabrication of numerous functional applications such as optical quality surface finishes, micro/nano surface texturing, and improved cutting force reduction on ferrous and other hard-to-cut materials. This flexibility comes directly from the high-frequency elliptical vibrations and discontinuous tool-workpiece contact. However, despite the use of this technology, there has been limited investigation on the overarching parametric influence that cutting parameters have on process outcomes such as cutting forces and surface quality.

Consequently, this thesis develops a parametric study for elliptical vibration assisted single point cutting in order to analyze the influence that certain input parameters have on cutting process outcomes. Furthermore, this study includes analytical, experimental and finite element-based analysis of the cutting forces and surface roughness formation. The results indicate the functional dependence between elliptical vibration process parameters and the resulting cutting forces and surface quality. Cumulatively, this contribution allows for effective recommendations to be made based on user-required cutting force reduction and/or surface quality improvements. Furthermore, the methodologies conceived in the following thesis aim to improve micromachining process efficiency, predictability, and precision.

## **Co-Authorship Statement**

- Chapter 1: Nikolai Farrus – wrote manuscript.
- Chapter 2: Nikolai Farrus – designed study, completed background research, analyzed results, wrote manuscript; Remus Tutunea-Fatan – supervised study, revised manuscript; Evgueni Bordatchev – supervised study, revised manuscript.
- Chapter 3: Nikolai Farrus – designed study, completed background research, performed experiments, analyzed results, wrote manuscript; Nicolas Milliken – contributed to machining tasks; Remus Tutunea-Fatan – supervised study, revised manuscript; Evgueni Bordatchev – directed study, revised manuscript.
- Chapter 4: Nikolai Farrus – designed study, completed background research, performed experiments, analyzed results, wrote manuscript; Nicolas Milliken – contributed to machining tasks; Remus Tutunea-Fatan – supervised study, revised manuscript; Evgueni Bordatchev – directed study, revised manuscript.
- Chapter 5: Nikolai Farrus – wrote manuscript; Remus Tutunea-Fatan – advised results and future directions, revised manuscript; Evgueni Bordatchev – evaluated summary, directed future directions, revised manuscript.

## **Acknowledgments**

There is no way I will be able to communicate all of the support, encouragement and opportunities I have been given throughout my graduate studies, however, I will do my best. I would like to begin by thanking all of the people who have supported me throughout my studies, none of this would have been possible without you. First and foremost, I would like to thank my supervisors, Dr. Remus Tutunea-Fatan and Dr. Evgueni Bordatchev, for the invaluable opportunity you granted me to earn my master's degree under your guidance and expertise. I am grateful for the limitless support that Dr. Remus Tutunea-Fatan provided me; from your extensive dedication, to your swift assistance, and your overall willingness to help me succeed, no matter the cost. Dr. Evgueni Bordatchev, thank you for your relentless and caring assistance and wisdom. Your dedication to research, technical work and attention-to-detail is contagious and is something I greatly appreciate you teaching me. Your innovative mindset and research methodologies are admirable, and something I will continue to strive towards.

I would also like to thank my research colleagues, Nicolas Milliken and Delfim Joao for their endless patience, mentorship, and overall friendship. Nicolas, thank you for the countless time and effort you designated to helping me in the machining lab, designing experiments, analyzing results, and walking me through countless other tasks. Your mentorship, assistance, and friendship is something I will always be grateful for. Delfim, thank you for your endless help, wisdom and patience with technical analysis, writing, and computer simulations. It was a pleasure working alongside you and learning from you.

Finally, I would like to thank my family, friends, and loved ones for the endless support you have given me throughout my endeavors. Without your love, support, and encouragement, there is no way I would have been able to achieve what I have. Thank you.

# Table of Contents

Abstract .....	ii
Summary for Lay Audience .....	iii
Co-Authorship Statement.....	iv
Acknowledgments.....	v
Table of Contents .....	vi
List of Tables .....	ix
List of Figures .....	x
List of Abbreviations .....	xiv
List of Symbols .....	xv
Chapter 1 .....	1
1 Introduction .....	2
1.1 Conventional single point cutting method .....	2
1.2 Elliptical vibration assisted single point cutting .....	4
1.3 Suitability of single point cutting tool .....	6
1.4 Applications of EVASPC .....	8
1.4.1 Optical quality surface finishing.....	8
1.4.2 Functional surface texturing .....	9
1.4.3 Cutting force reduction .....	12
1.5 Motivation.....	14
1.6 Objectives .....	15
1.7 Contributions.....	16
1.8 Thesis overview .....	16
Chapter 2.....	19
2 Classification and Geometrical Modeling of EVASPC Processes .....	20
2.1 Background.....	20

2.2 Geometrical modeling of EVASPC kinematics.....	21
2.3 Implementations and applications of EVASPC.....	25
2.4 EVASPC cutting force model.....	28
2.5 Summary and conclusions .....	33
Chapter 3.....	34
3 Cutting Force Reduction by Elliptical Vibration Assisted Cutting.....	35
3.1 Overview.....	35
3.2 Background.....	35
3.3 Axial strategy for single point cutting of V-grooves with constant cutting area..	37
3.4 Experimental setup and data processing methodology.....	40
3.5 Cutting forces during multi-pass micromachining of V - grooves performed with and without EVC motions.....	44
3.6 Summary and conclusions .....	51
Chapter 4.....	53
4 Parametric Analysis of EVASPC Characteristics and their Effect on Process Performance .....	54
4.1 Overview.....	54
4.2 Background.....	54
4.3 Parametric study of experiments.....	56
4.4 Experimental procedure .....	63
4.4.1 Cutting force measurement and analysis procedure .....	69
4.4.2 Surface topography measurement and analysis procedure .....	70
4.5 Cutting force results.....	71
4.6 Surface quality results.....	78
4.7 Functional dependence analysis.....	85
4.8 Finite element modeling .....	90
4.8.1 General setup .....	90

4.8.2	Material parameters .....	91
4.8.3	Instance meshing.....	93
4.8.4	Boundary conditions .....	95
4.8.5	Friction consideration .....	98
4.8.6	ABAQUS Results and analysis.....	99
4.9	Summary and conclusions .....	103
Chapter 5	.....	105
5	Summary, Conclusions, and Future Directions.....	106
5.1	Summary and conclusions .....	106
5.2	Research limitations.....	107
5.3	Future directions .....	109
References	.....	111
Curriculum Vitae	.....	117



## List of Tables

Table 2.1: Possible EVASPC implementations. ....	25
Table 3.1: Elliptical vibration amplitude experiment parameters. ....	44
Table 3.2: Cutting trial parameters. ....	45
Table 4.1: Matrix of experimental EV amplitudes along with fixed cutting parameters. ....	62
Table 4.2: Cutting trial parameters. ....	68
Table 4.3: Cutting tool properties. ....	92
Table 4.4: Workpiece properties. ....	92
Table 4.5: Johnson-Cook damage criteria. ....	92

# List of Figures

Figure 1.1: Schematic of conventional single point cutting method .....	2
Figure 1.2: Diamond tool graphitization.....	3
Figure 1.3: Elliptical vibration assisted single point cutting (EVASPC) controlled by elliptical vibration motion vector ( $h_{EVC}(t)$ ), cutting speed ( $V_{SPC}$ ), and depth-of-cut ( $DoC$ ). ....	5
Figure 1.4: Schematic of elliptical vibration assisted single point cutting .....	5
Figure 1.5: Significant features of primary single point cutting tools .....	7
Figure 1.6: Optical surface quality enhancements through EVASPC at the NRC-CNRC.....	9
Figure 1.7 Paint-free colouring using EVC .....	11
Figure 1.8: Original cutting force model proposed by Zhang <i>et al.</i> [28].....	13
Figure 1.9: Cutting force model using an advanced Merchant's Circle .....	13
Figure 2.1: EVASPC kinematics obtained through the superposition of SPC and EVC. ....	21
Figure 2.2: EVASPC motion characteristics .....	23
Figure 2.3: Flow diagram of the EVASPC kinematics.....	24
Figure 2.4: Constant cutting conditions (Implementation 1).....	26
Figure 2.5: Modulated cutting speed (Implementation 2). ....	26
Figure 2.6: Modulated EV amplitudes (Implementation 3).....	27
Figure 2.7: Modulated phase shift (Implementation 4). ....	28
Figure 2.8: Cutting force model for conventional SPC .....	29
Figure 2.9: The two EVC phases/tool motion intervals.....	31
Figure 2.10: Cutting forces in the kinetic friction phase of EVC .....	31

Figure 2.11: Cutting forces in the reversed friction phase of EVC .....	32
Figure 3.1: Cutting kinematics of V-groove fabrication via SPC.....	37
Figure 3.2: Modified Merchant’s Circle method for representing V-groove fabrication .....	38
Figure 3.3: Cutting forces in the kinetic friction phase of EVC .....	39
Figure 3.4: Cutting forces in the reversed friction phase of EVC .....	39
Figure 3.5: Experimental setup and data processing workflow.....	41
Figure 3.6: Triangular monocrystalline single point diamond cutting tool [59].....	43
Figure 3.7: V-groove fabrication overview .....	43
Figure 3.8: Average cutting forces for each experiment.....	46
Figure 3.9: Evolution of cutting forces during no-EVC vs with-EVC V-groove cutting characterized by $A_y = 6 \mu\text{m}$ and $A_z = 2 \mu\text{m}$ .....	47
Figure 3.10: V-groove surface quality .....	50
Figure 4.1: EVASPC process flow diagram. ....	56
Figure 4.2: Step-by-step EVASPC study methodology.....	57
Figure 4.3: Elliptical vibration amplitude orientations, tool trajectory and cutting force profile .....	58
Figure 4.4: EV amplitude influence on depth-of-cut.....	61
Figure 4.5: Experimental setup and data processing workflow.....	63
Figure 4.6: Orthogonal monocrystalline single point diamond cutting tool.....	64
Figure 4.7: Multi-ribbed Aluminum T-6061 workpiece used for experiment.....	65
Figure 4.8: Experimental setup. ....	66

Figure 4.9: Cutting kinematics of rib fabrication via orthogonal EVASPC .....	67
Figure 4.10: Cutting force measurement and analysis procedure. ....	70
Figure 4.11: Surface profile measurement and analysis procedure. ....	71
Figure 4.12: Detailed cutting force results comparing conventional orthogonal cutting to EVASPC .....	72
Figure 4.13: Summary of EV amplitude influence on cutting force generation ( $F_y$ ). ....	75
Figure 4.14: Cutting process duty cycle (%). ....	77
Figure 4.15: Ellipse area for each cutting experiment. ....	78
Figure 4.16: Experimental validation of cutting parameters .....	79
Figure 4.17: Raw surface FFT analysis in MATLAB .....	80
Figure 4.18: EVASPC surface roughness ( $S_a$ ) for orthogonal cutting experiment characterized by $A_y = 6 \mu\text{m}$ and $A_z = 2 \mu\text{m}$ .....	81
Figure 4.19: Summary of EV amplitude influence on surface roughness ( $S_a$ ). ....	83
Figure 4.20: Physical demonstration of EV amplitude influence on surface quality using second workpiece from orthogonal EVASPC experiment. ....	84
Figure 4.21: Comparative parametric study plot .....	86
Figure 4.22: Cutting force ( $F_y$ ) regression model .....	87
Figure 4.23: Surface roughness ( $S_a$ ) regression model .....	89
Figure 4.24: FEM meshed assembly setup with tool and workpiece. ....	93
Figure 4.25: FEM model assembly setup with tool and workpiece BC .....	95
Figure 4.26: Conventional SPC boundary conditions. ....	96

Figure 4.27: EVC and SPC boundary conditions that produce governing EVASPC motion trajectory. ....	97
Figure 4.28: FEM simulation results. ....	99
Figure 4.29: SPC FEM simulation results .....	100
Figure 4.30: EVASPC FEM simulation results .....	101

## List of Abbreviations

CC	Conventional Cutting
SPC	Single Point Cutting
CNC	Computer Numeric Control
EVC	Elliptical Vibration Cutting
EVASPC	Elliptical Vibration Assisted Single Point Cutting
HTC	Hard-to-Cut
FEM	Finite Element Method
EV	Elliptical Vibrations
USPC	Ultra-precise Single Point Cutting

## List of Symbols

$DoC_{cc}$	Conventional SPC depth-of-cut
$DoC_{EVC}$	Elliptical Vibration Cutting depth-of-cut
$DoC_{total}$	Total depth-of-cut
$V_{SPC}$	Single Point Cutting Speed
$A_y, A_z$	Horizontal amplitude, Vertical amplitude
$\omega$	Vibrational Frequency
$\phi_y, \phi_z$	Horizontal Phase Shift, Vertical Phase Shift
$\theta$	Feed Angle
$\mathbf{h}_{SPC}(t)$	Single Point Cutting Motion Vector
$\mathbf{h}_{EVC}(t)$	Elliptical Vibration Cutting Motion Vector

# Chapter 1

## Introduction



# 1 Introduction

This chapter will provide a brief introduction to elliptical vibration cutting and the advantages it poses over conventional single point cutting methods. In addition, a literature review will outline the major implementations and applications provided by this technology. This will be followed by a detailed description of the thesis motivations, objectives, and contributions, and will conclude with a brief outline of each chapter.

## 1.1 Conventional single point cutting method

When one is concerned with the single point diamond cutting of metals to achieve ultra-precise surface structures and optical quality surface finishes that are accurate, repeatable, and affordable, the consideration of the tool-material interaction is vital. Traditionally, 3D objects are fabricated using a subtractive manufacturing method called conventional cutting (CC) in order to incrementally remove bulk workpiece material based on the user requirements. One example of CC is single point cutting using a CNC machine, and is defined by the continuous contact maintained between the traveling cutting tool and fixed workpiece, Figure 1.1. This form of CC is typically controlled by a select number of process parameters: cutting speed ( $V_{SPC}$ ), depth-of-cut ( $DoC_{cc}$ ), tool material and geometry, as well as workpiece material and geometry. More specifically, single point cutting (SPC) is defined by a single cutting edge used as the primary feature for material removal (tool-workpiece contact point in Figure 1.1(b)).

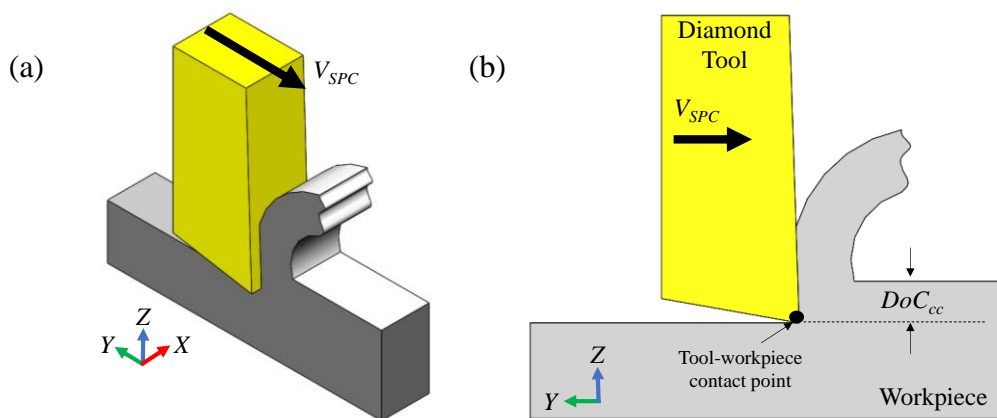


**Figure 1.1:** Schematic of conventional single point cutting method: (a) Isometric view of tool motion, and (b) side view with user-defined process parameters.

Conventional SPC is simple, fast, and inexpensive, however, when it comes to ultra-precision machining, this primitive cutting method continuously shows limitations in workpiece quality, accuracy, and process efficiency. Such complications come from the interaction between the tool and workpiece materials, as well as the limited flexibility in process parameters.

Typically, the creation of ultra-precise components using CC is negatively impacted by the continuous contact maintained between the tool and the workpiece, and this is especially prominent when using a diamond cutting tool for applications on ferrous metals and other hard-to-cut (HTC) materials. When the diamond tool maintains continuous contact with the ferrous or HTC material, high contact pressure at the tool-workpiece interface leads to overwhelming cutting temperatures, causing the diamond tool to graphitize. Graphitization is a thermochemical reaction that occurs between the tool's diamond material and the ferrous workpiece material, Figure 1.2.

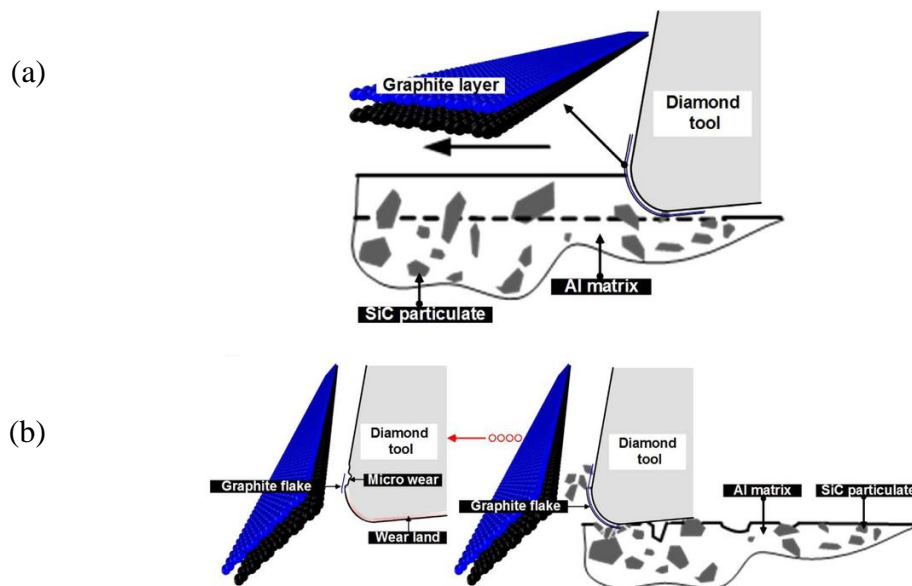


**Figure 1.2:** Diamond tool graphitization: (a) Conventional cutting using a diamond tool, and (b) diamond tool graphitization leading to tool deterioration and workpiece imperfections [1].

More specifically, this phenomenon occurs when the carbon crystals in the diamond are converted to graphite as a result of exceptionally high contact pressure and temperature at the cutting interface—exceeding around 1000 K [2]. Furthermore, Zou *et al.* observed

that as the temperature increases past this threshold the graphitization rate increases as well. The phenomenon of tool graphitization ultimately leads to the eventual build-up, solidification, and adherence of carbon to the tool tip, resulting in unacceptable errors in topographical dimensionality and compromised surface quality, Figure 1.2(b).

Ultimately, conventional SPC is unacceptable for precision-machining applications, especially when using a diamond tool on ferrous and other HTC materials, due to accelerated and unpredictable tool wear, poor surface quality, and enlarged cutting forces [3].

## 1.2 Elliptical vibration assisted single point cutting

Hence, the introduction of elliptical vibration cutting (EVC). This method has been used dating back to the early 20<sup>th</sup> century, where the introduction of ultrasonic vibrations was seen to enhance cutting forces and surface finish, when compared to its predecessor, static conventional cutting [4, 5]. More recently, 1994, Shamoto *et al.* implemented EVC with the intent of improving single point diamond cutting on ferrous and other HTC materials [6]. Since its conception, EVC has been used for numerous high-precision cutting methods (turning, milling, broaching, lathing, and single point orthogonal cutting) as well as its application on various workpiece materials (aluminum alloy, tungsten alloy, titanium alloys, acrylic, carbon fiber reinforced plastics (CFRP), and glass).

Contrary to CC, this novel method relies on the discontinuous contact between the tool and the workpiece across the cutting length, Figure 1.3. This is achieved through the high frequency elliptical motion of the tool tip ( $\mathbf{h}_{EVC}(t)$ ), powered by two synchronized piezoelectric transducers (PZT) that vibrate in a sinusoidal manner based on the PZT resonant modes [7]. Each PZT is orientated such that they vibrate at angle of 45° with respect to the vertical axis (Z-axis), Figure 1.4(a). This orientation allows for maximum control of the elliptical locus shape and amplitude in both the vertical direction (Z-axis) and the horizontal direction (Y-axis).

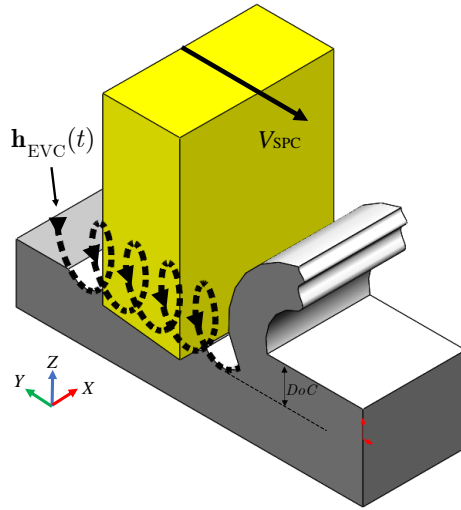


**Figure 1.3:** Elliptical vibration assisted single point cutting (EVASPC) controlled by elliptical vibration motion vector ( $\mathbf{h}_{EVC}(t)$ ), cutting speed ( $V_{SPC}$ ), and depth-of-cut ( $DoC$ ).

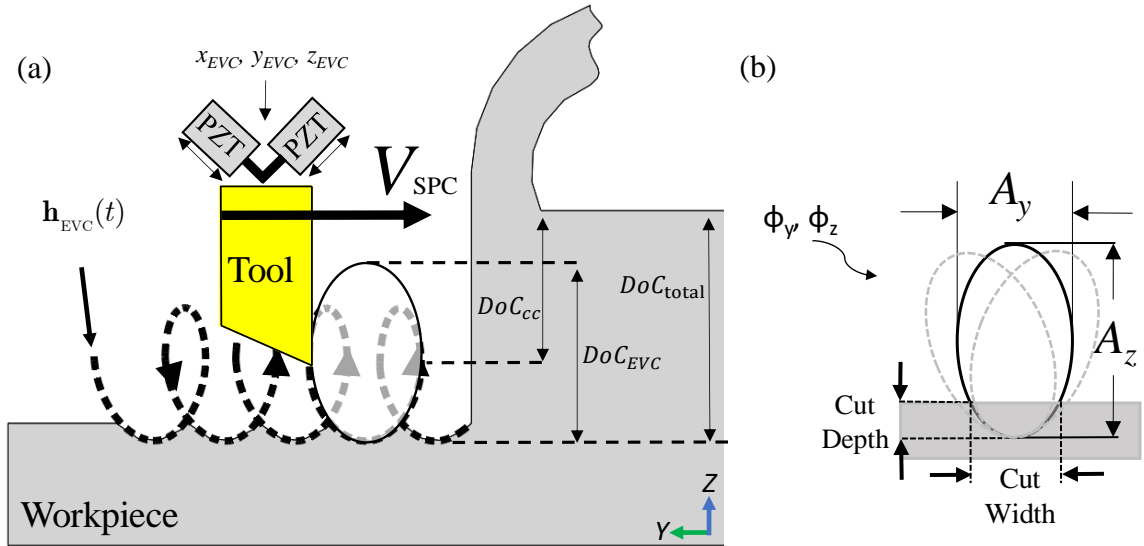


**Figure 1.4:** Schematic of elliptical vibration assisted single point cutting: (a) EVASPC tool motion defined by  $\mathbf{h}_{EVC}(t)$ , and (b) EVASPC horizontal and vertical amplitudes,  $A_y$  and  $A_z$ , respectively.

More specifically, as a result of these high-frequency elliptical vibrations (up to 40kHz [8]), the tool tip periodically displaces from its neutral position ( $DoC_{cc}$ ) as it travels along the cutting path, producing the so-called “surface cusps”. The magnitude of this deviation

from  $DoC_{cc}$  is based on the chosen horizontal and vertical amplitudes ( $A_y$  and  $A_z$ , respectively) Figure 1.4(b), and can range anywhere from 1  $\mu\text{m}$  to nearly 10  $\mu\text{m}$ , based on apparatus capabilities.

Contrary to the limited list of cutting parameters provided by CC ( $V_{SPC}$  and  $DoC_{cc}$ ), EVC provides enhanced capabilities through the introduction of additional cutting variables, Figure 1.4. The ultrafast EV motion is defined by three primary parameters: horizontal and vertical amplitudes ( $A_y$  and  $A_z$ , respectively), the elliptical vibration frequency ( $\omega$ ), and the phase shift ( $\phi_y, \phi_z$ ) that defines the relative spatial orientation between  $A_y$  and  $A_z$ . Furthermore, the ratio between the cutting speed ( $V_{SPC}$ ) and the vibrational frequency ( $\omega$ ), termed the cusp width, will show significant functionality throughout this thesis,

Figure 1.4(a). In essence, this ratio ( $\frac{V_{SPC}}{\omega}$ ) defines the periodic spacing between each EVC-induced cusp [9].

Ultimately, the combination of conventional SPC and ultrasonic EVC, as well as the relative positioning between the planes in which they occur, cause the tip of the cutting tool to follow a trochoidal path as it travels across the workpiece (Figure 1.3). This integration of SPC and EVC is referred to as elliptical vibration assisted single point cutting (EVASPC), and will be the primary fabrication method used throughout this thesis.

### 1.3 Suitability of single point cutting tool

In addition to the EVC tool motion trajectory, this thesis utilizes ultra-precise single point cutting (SPC) as its primary machining method [10]. EVC adds complexity to the cutting process through the introduction of unique EV cutting motion kinematics, however, single point cutting can simplify analysis dramatically. SPC is defined by a single cutting edge used as the primary feature for material removal, while the secondary tool characteristics provide a supporting role in the cutting process, Figure 1.5. Consequently, this process produces chips that travel in the direction parallel to the feed direction [11], and tends to limit the primary force components to two directions: the cutting direction

(Y-axis) and the thrust direction (Z-axis) [12]. This cutting method pairs nicely with EVASPC and reduces the number of cutting force components required for analysis.

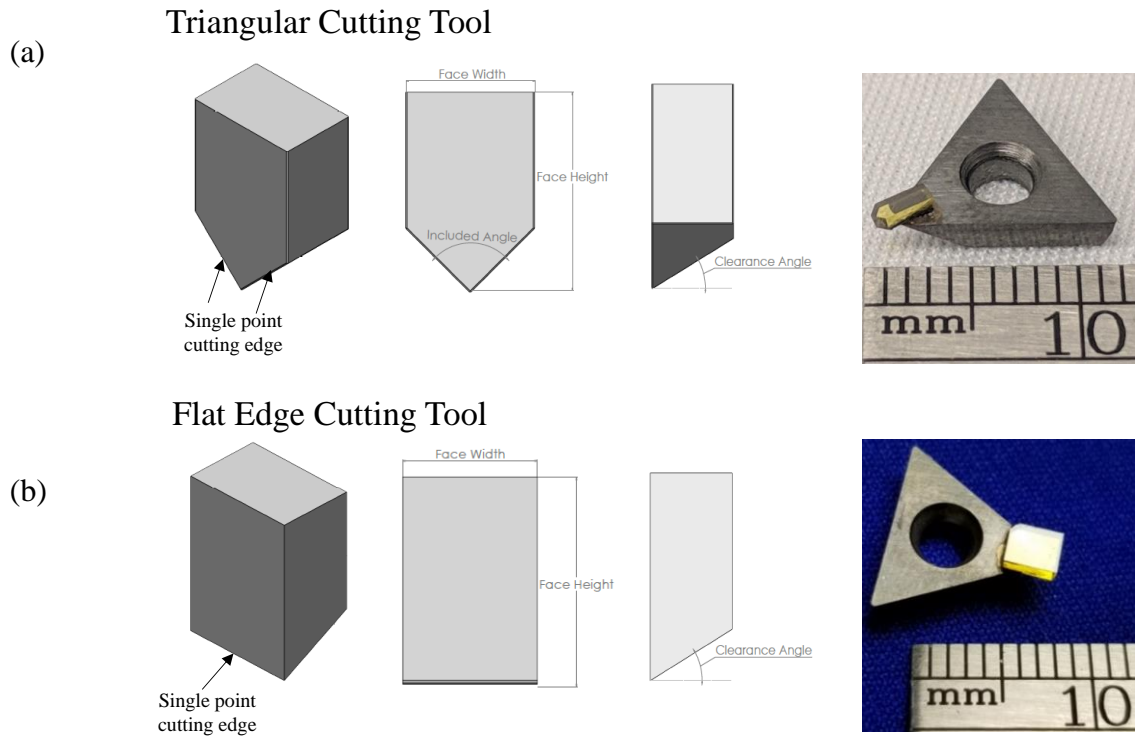


**Figure 1.5:** Significant features of primary single point cutting tools: (a) Triangular cutting tool, and (b) flat edge cutting tool.

On this note, the overall geometry of the cutting tool can impact the effectiveness of SPC. To simplify the analysis of cutting results, there were two types of tool geometries used for experimentation, however this is by no means an exhaustive list of available tools. The two primary tool geometries considered throughout this thesis consist of a triangular cutting tool (Figure 1.5(a)) and a flat edged cutting tool (Figure 1.5(b)). The triangular cutting tool is typically assumed to have a completely sharp cutting point with geometry defined by its face height and width, included angle and clearance angle. On the other hand, the flat edge orthogonal cutting tool is defined by the geometrical cutting face width, height, and clearance angle. In addition to their geometry, both tools used for experimentation were made of from a synthetic monocrystalline diamond material which is crucial for the fabrication of ultra-precise surfaces on ferrous and HTC materials, and goes hand-in-hand with EVASPC [13].

## 1.4 Applications of EVASPC

The applications of EVASPC are directly related to the variation of one or more specific cutting parameters chosen by the user. This being said, the consistent theme surrounding EVASPC continues to stress micro/nano-fabrication of ferrous and other hard-to-cut materials. This typically includes one of three overarching applications: high quality optical surface finishing, micro/nano surface texturing, and cutting force reduction. More generally, EVASPC has applicability in a number of industries: from medicine, to aerospace, optical component fabrication, and security encryption. Such industries rely on precision-machining to achieve industry standards and tolerances that guarantee safety and functionality, all the while fabricating their products in a time and cost effective manner.

### 1.4.1 *Optical quality surface finishing*

Right from its conception, EVC has demonstrated the capability of achieving optical quality surface finishing using a diamond cutting tool on ferrous and other hard-to-cut (HTC) materials, something that was deemed impossible until Shamoto *et al.* [6].

Following their initial discovery, Shamoto *et al.* persisted to demonstrate the consistently high surface quality provided through EVC for the fabrication of hardened die steels, measuring surface roughness less than  $0.05\ \mu\text{m}$  [14]. For reference purposes, the industry standard for mirror-like surface finish is  $R_a < 0.1\ \mu\text{m}$ , while superfinishing—the hallmark surface finishing process—is capable of  $R_a \approx 0.025\text{--}0.2\ \mu\text{m}$  [15].

This application is typically characterized through constant/fixed cutting parameters, such that the spatial consistency of the EVC motion assists in creating a uniform surface with high-accuracy, dimensionality, and low surface roughness.

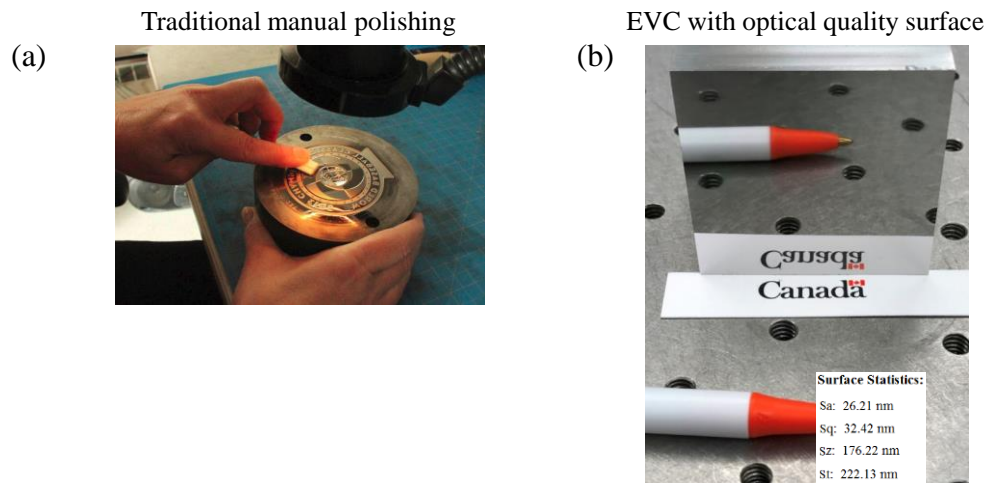


**Figure 1.6:** Optical surface quality enhancements through EVASPC at the NRC-CNRC:(a) Traditional manual polishing, and (b) EVC-induced optical surface.

One practical application of EVASPC, and one that has been tested at the National Research Council of Canada (NRC-CNRC), is the elimination of manual polishing following machining. Traditionally, in order to achieve optical quality surfaces, the post-processing requirement of manual polishing was used to buff the workpiece in order to improve surface roughness and compensate for the machining inaccuracies, Figure 1.6(a). This process of manual polishing is flawed through additional processing time, the introduction of human error, and further removal of material such that final dimensionality of the workpiece is negatively affected. Therefore, with the introduction of EVC motion it is possible to fabricate a surface with micron-scale surface structures that achieve acceptable optical functionality—reiterated in Figure 1.6(b) where EVC cutting shows mirror-like qualities with areal roughness of  $S_a = 26.21$  nm.

#### 1.4.2 Functional surface texturing

Contrary to optical surface finishing where roughness is minimized, EVC can also take advantage of the generated surface cusps and their unique structuration. Such applications are typically possible through the modulation of certain EVC parameters such as the cutting speed ( $V_{SPC}$ ), the EV amplitudes ( $A_y$  and  $A_z$ ), and/or the phase shift ( $\phi_y, \phi_z$ ). As a result, the tool motion trajectory changes either the orientation, depth or spacing between each consecutive surface cusp. This in turn produces micro or even nano-scale functional



surface structures used for texturing and functionality applications, such as surface wettability and microfluidic systems, micro-dimpling, paint-free surface colouring, and holographic structuration.

Some of the first demonstrations of EVC-generated surface texturing was done using orthogonal EVASPC to generate functional surface micro/nano-structures through periodic EV amplitude control (changing  $A_y$  and  $A_z$ ), ranging from 30–100 Hz. Ultimately, this translated into sinusoidal, ramp, or zig-zag tool paths with peak-to-valley heights ranging from , 0.81  $\mu\text{m}$  to 1.00  $\mu\text{m}$  [16].

More recently, Guo *et al.* used this methodology to mimic the hydrophobic characteristics of a rice leaf by creating parallel channels of hierarchical surface structures with the assistance of EVC [17]. The phenomenon of hydrophobicity stems from the reduced contact angle between the liquid droplet and surface [18], and has seen applicability in microfluidic devices [19], self-cleaning surfaces, low adhesion surfaces, and drag reduction [20]. Guo *et al.* accomplished this functionality through the generation of slanted surface texturing via tilted EV ellipse orientations ( $\phi_y = 95^\circ$ ). Ultimately producing EV micro-channels that reduced the contact angle from  $90^\circ$  to  $63^\circ$ , and therefore increased anisotropic/hydrophobic effects. A similar principle was used by Zhang *et al.*, however they used individual micro-dimpling to achieve such surface wettability [21].

Finally, one of the most recent surface texturing implementations of EVC comes through its ability to create paint-free colouring of metallic surfaces. This application is dependent on the fundamental optical properties of diffraction gratings, in which incoming white light (from sources such as incandescent bulbs, sunlight, etc) is separated into a spectrum of wavelengths, and their corresponding colours [22]. Off-axis micro-grooves have been used for this technology, such that the angular-dependent geometry of the groove offers diffractive characteristics. More specifically, the wavelength (and therefore the colour) seen by the viewer is contingent on the angle of each sequential groove, such that shorter wavelengths are diffracted at smaller angles and longer wavelengths are diffracted at

larger angles, Figure 1.7(a) [23]. Ultimately, colour comes as a function of the fabricated groove angle and/or incoming/outgoing angle of light.

This implementation of EVC has been reproduced at the National Research Council of Canada through the modulation in cutting speed ( $V_{SPC}$ ), such that the spatial frequency between surface cusps matches the wavelength of visible light, Figure 1.7(b).

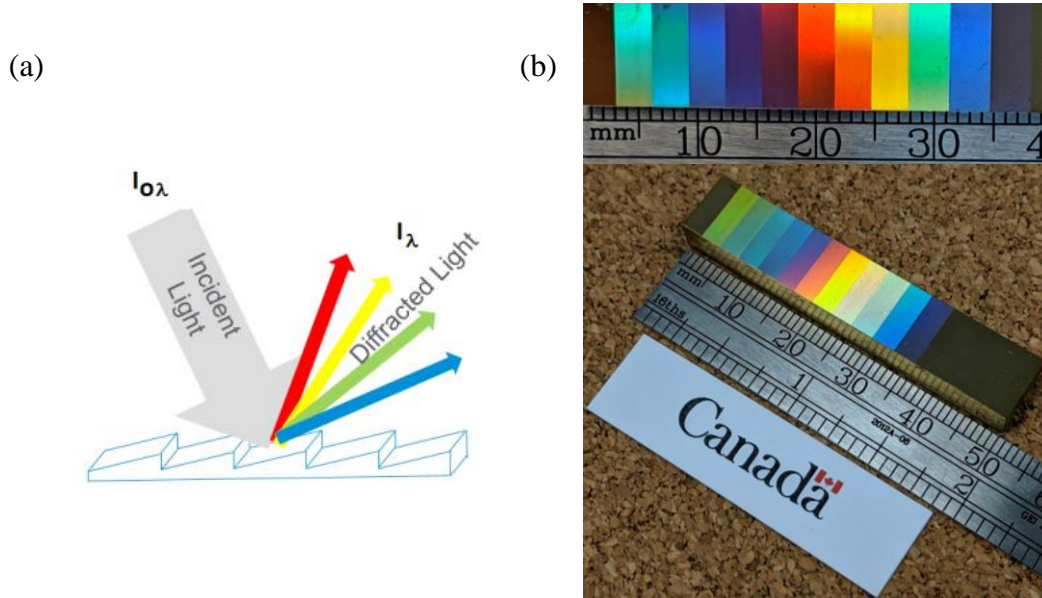


**Figure 1.7** Paint-free colouring using EVC: (a) Reflective diffraction gratings [23], and (b) EVC-induced diffraction gratings for surface colouration.

This being said, surface colouration has also been achieved through the variation of EV amplitudes ( $A_y$  and  $A_z$ ) and/or phase shift ( $\phi_y, \phi_z$ ). Yang and Guo have specialized in this field as recently as the last three years. Their study in 2017 demonstrated the core feasibility of using EVC for surface colouration [24]. This was done by phasing the periodicity of the EVC-induced surface cusps with the visible light range (400 nm to 760 nm), such that the diffraction of visible light was achieved [25]. Furthermore, tool path optimization, by means variable phase shift ( $\phi_y = 45^\circ, 90^\circ, 135^\circ$ ), enhanced the control and flexibility of colour markings such that paint-free pictures were created [26]. More specifically, the variation in phase shift accurately controlled the geometric structure of each groove, such that diffraction was consistently and accurately established.

Although this implementation of EVC motion is relatively new, there are a variety of future applications for surface colouration such as bio-mimicry, holographic structuring, and security encryption.

### 1.4.3 *Cutting force reduction*

Elliptical vibration diamond cutting on ferrous and HTC materials has also shown tremendous cutting force reduction and stabilization when compared to conventional no-EVC cutting. Shamoto *et al.* demonstrated this occurrence following the fabrication of hardened die steels in early testing [14]. This being said, further analysis would be needed to understand why and where this force reduction originates. Ma *et al.* took the first step through the development of a thrust cutting force model for the EVC turning process. This model mathematically demonstrated that the transient thrust force component in EVC assists in the chip flow and frictional force reduction. More specifically, this is because of the reversal in thrust force direction as the tool follows its velocity-varying elliptical path [27]. This being said, Ma *et al.* were still unsure of the precise formulation that described their observations.

It was not until 2012 that an analytical model of orthogonal EVC was developed [28]. This model stated that the overall cutting force generation relies on three cutting process factors: the transient thickness of cut ( $T_oC$ ), the transient shear angle ( $\phi_c$ ), and the reversed friction zone. Following Zhang's path, Bai *et al.* continued this analysis using the minimum energy principle for orthogonal EVC turning applications [29].

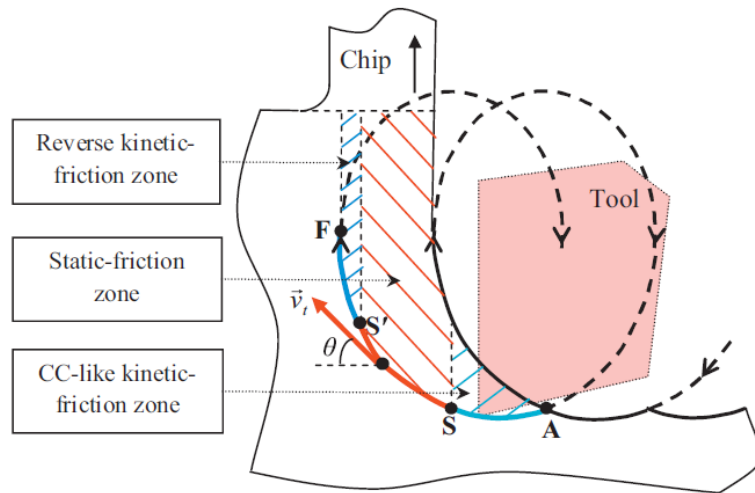


**Figure 1.8:** Original cutting force model proposed by Zhang *et al.* [28].

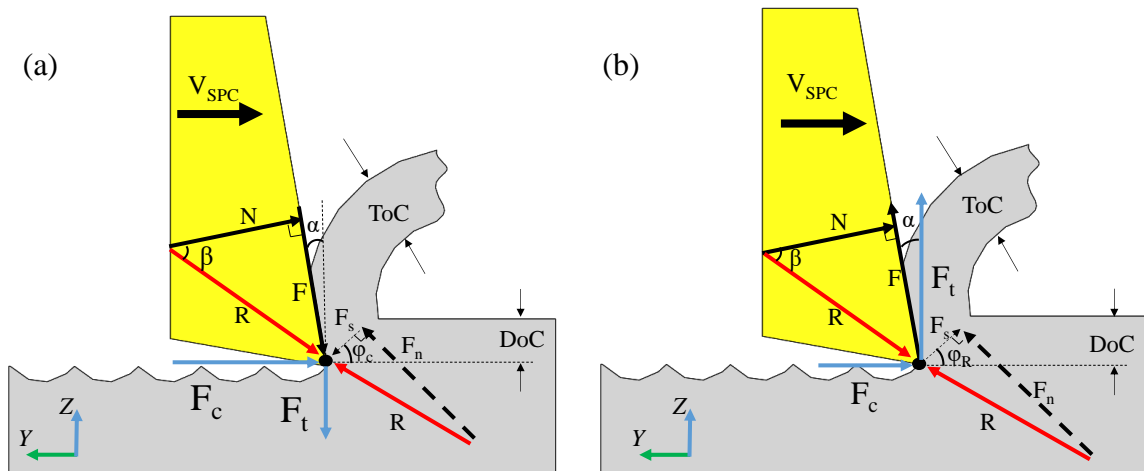


**Figure 1.9:** Cutting force model using an advanced Merchant's Circle: (a) CC kinetic friction zone, and (b) the reversed kinetic friction zone.

More specifically, both Zhang and Bai use a modified form of the Merchant's Circle, in which a single elliptical revolution of the tool is broken into sequential phases that demonstrate the effect that EVC has on transient force vectors (Figure 1.8) [30]. This cutting force model will be discussed in further depth throughout this thesis, however in general terms it consists of two phases. The first phase, CC-like kinetic friction zone, is synonymous with conventional cutting, in which the thrust force ( $F_t$ ) lays in the direction opposite to the chip velocity, Figure 1.9(a). This opposition in motion increases frictional

forces between the tool and workpiece, ultimately producing high resultant cutting forces ( $F_c$ ). Conversely, the force-reduction characterized by EVC occurs as the tool continues along its trajectory and into the reversed kinetic friction zone, triggered at point  $S'$  in Figure 1.8. In this phase, the tool velocity is now in the same direction as the chip flow. As a result, the thrust and friction force vectors now point in the same direction, assisting one another in chip removal and overall cutting force reduction, Figure 1.9(b).

Ultimately, the modified Merchant's Circle CF analysis provides a theoretical explanation of the EVC-induced cutting force reduction based on the tool-workpiece interaction via shear deformation properties of the material, along with the influence that cutting parameters have on force vector orientations.

## 1.5 Motivation

Elliptical vibration diamond cutting represents one of the few fabrication methods capable of achieving ultra-precise surface quality on ferrous metals and other hard-to-cut materials. In addition to this, EVC has also demonstrated its ability to reduce tool wear and cutting forces, all the while introducing greater cutting process flexibility. This comes as a direct result of high-frequency EVC motion kinematics characterized by the discontinuous contact between the diamond cutting tool and the workpiece. As seen through literature, intense research has gone into understanding the principle cutting mechanics of EVC as well as the various applications it is capable of [29].

However, publications have revealed that most studies focus on an individual EVC parameter and the effect it has on the cutting process. For example, Shamoto *et al.* fixed all EVC parameters in order to obtain an optical quality surface [31], whereas Guo *et al.* and Yang *et al.* manipulated only the phase shift in order to achieve a super-hydrophobic surface [17] and metallic surface colouration [26], respectively. In addition, it is apparent that certain EVC parameters prove more crucial for certain applications, while others seem to have either minimal or even harmful effects on the overall cutting process. While such characteristics might be sufficient for conventional and mundane metal fabrication, high-precision EVASPC is sensitive to the smallest change in cutting parameters and the result can lead to vastly different surface quality and functionality.

Ultimately, there appears to be an absence of information regarding the parametric effect of EVC parameters on single point diamond cutting processes, making this a primary field of exploration. This issue is critical when it comes to determining the influence that a given EVC parameter has on the cutting process. Consequently, such a parametric study would be capable of suggesting the appropriate EVC parameter values based on the machining apparatus capabilities and the user-desired application. In addition, a reoccurring motivation when it comes to micromachining aims to enhance EVASPC processes for the purpose of improved tool wear, overall cutting process stabilization, and predictability.

## 1.6 Objectives

EVASPC is a novel cutting technology that is pushing the boundaries of ultra-precise micro/nano-fabrication. The primary objective of this study will be to isolate and analyze the influence of EVC motion on the cutting process. In order to do so, the objectives have been split into three categories: (1) EVC's role in tool tip trajectory, (2) EVC's role in the cutting process, and (3) EVC's role in final workpiece surface topography.

The following chapters will each provide a specific contribution to the overall objectives of this thesis. Furthermore, this thesis will:

- Develop an analytical description of EVC motion kinematics and cutting force generation.
- Demonstrate the effect of elliptical vibrations on cutting force reduction, stabilization, and overall SPC process enhancement.
- Develop a parametric study that links the variability of EV amplitudes ( $A_y$  and  $A_z$ ) to both the cutting force production and topographical surface formations. Thus, understanding the functional dependence between input EVC parameters and output metrics.

These objectives will be achieved through the completion of analytical, numerical, and experimental analysis, and will conclude with a discussion of completed work followed by proposed future steps required to further develop this manufacturing process.

## 1.7 Contributions

The overall role of this thesis contributes to the field of ultra-precise elliptical vibration assisted single point diamond cutting when being used to improve cutting force reduction and surface quality. The specific contributions to this technology go hand-in-hand with the objectives previously outlined: namely, the development of geometrical modeling, mechanical modeling, experimental methodology and post-processing analysis, functional dependence modeling, and finite element modeling.

The geometrical modeling of EVC tool motion trajectory and cutting force generation creates a firm understanding of EVASPC cutting mechanics. Consequently, these kinematic models are beneficial when developing precise cutting strategies, analyzing EVC-assisted process results, and ultimately, maintaining stable, predictable, and repeatable cutting conditions. Consequently, such models assist in the development of novel experimental methodologies, post-processing procedures and supportive finite element models that allow for accurate analysis of key EVASPC outcomes, namely the cutting force magnitudes and surface roughness of EVC-induced microstructures.

On this note, the technological contribution of this thesis is concerned with the established parametric study. The preceding contributions ultimately allow for the correlative analysis between EVC parameter manipulation and cutting process outcomes. This preliminary investigation allows for EVC parameter recommendations to be made based on cutting force reduction and/or surface quality improvements. Ultimately, the methodologies conceived in the following thesis aim to improve EVASPC process efficiency, predictability, and precision.

## 1.8 Thesis overview

The overall organization of this thesis will follow the three sequential objectives and the chapter configuration will follow an identical structure.

Chapter 2 describes elliptical vibration cutting in terms two primary analytical models. The first introduces a geometric representation of the EVASPC kinematic motion which originates from the advanced elliptical tool trajectory. This section begins with the

definition of EVASPC's governing equations of motion, followed by a description of each process parameter along with their contribution to the cutting motion. Four implementations of this technology are then introduced, each one based on the variation of a specific cutting parameter. The second half of this chapter details the modified Merchant's Circle cutting force model. This analytical model provides a theoretical explanation of the EVC-induced cutting force reduction based on tool-workpiece interaction.

Chapter 3 builds on a study that exemplifies the capabilities of ultra-precise single point cutting (USPC) [32]. More specifically, a multi-pass axial cutting strategy is performed with constant cutting area in order to fabricate high-accuracy V-grooves. In this regard, the ultimate objective of this study is to demonstrate the effect that elliptical vibrations have on cutting force reduction. The first section of this chapter develops the cutting mechanics along with a brief description of the modified Merchant's Circle cutting force model that describes EVC-induced force reduction. From here the experimental setup is presented, followed by a detailed comparative analysis between cutting forces generated with and without EVC, along with a discussion of these results.

Chapter 4 presents a parametric study that utilizes orthogonal single point cutting integrated with elliptical vibrations to isolate a pair of linked cutting parameters—EV horizontal and vertical amplitudes. The main objective being to analyze the influence that their relationship has on the cutting forces and surface quality results. The first section develops the experimental methodology and EV cutting mechanics. Sixteen experiments were then conceived—fifteen consisted of unique EV amplitude pairs, while the final experiment was done in the absence of EVC. From here the extensive experimental setup is described, followed by a detailed comparative analysis of cutting force and surface quality results. The determination of a so-called functional dependence model is also achieved through the creation of a parametric regression model; ultimately, defining the transition from a machining process that prioritizes cutting force reduction to one that prioritizes surface quality improvement. To wrap up this chapter, the introduction of an FEM model provides a supporting role when demonstrating the cutting force reduction offered by EVASPC.



Chapter 5 outlines the discoveries presented in this thesis and provides a summary of the achievements and advancements made in the analysis of EVASPC for ultra-precision manufacturing. To conclude, the observations made throughout the previous chapters will prove significant for future work and recommendations.

## Chapter 2

### Classification and Geometrical Modeling of EVASPC Processes

A revised version of this chapter has been accepted as: Farrus, N., Tutunea-Fatan, O.R., & Bordatchev, E. V., 2019. CAD/CAM Framework for Generation of Surface Microstructures through Elliptical Vibration Assisted Single Point Cutting. Accepted for publication in *Computer-Aided Design and Applications*.

A revised version of this chapter has been accepted as: Farrus, N., Joao, D., Milliken, N., Tutunea-Fatan, O.R., & Bordatchev, E. V., 2019. Reduction of cutting forces by elliptical vibration in multi-pass ultraprecise single point axial cutting of V-grooves. *Procedia Manufacturing*, 48, pp. 570-578.

## 2 Classification and Geometrical Modeling of EVASPC Processes

### 2.1 Background

Recent years have shown an increased demand for SPC methods that are capable of generating surfaces characterized by a broad range of functionalities, such as improved optical surface quality [14], paint-free coloring [24], surface wettability [17], and micro-surface texturing [21]. While such functionalities can be obtained, conventional SPC poses limitations that continue to hinder further developments. Among them, the dimensional barrier (i.e., the capability to produce precise micro/nano-structures) as well as the ability to machine ferrous and other hard-to-cut (HTC) materials by means of diamond tooling. To address these challenges, EVC is introduced as a technology capable of augmenting the previously proposed ultra-precise SPC [10]. Consequently, a combination of SPC and EVC motions constitutes elliptical vibration assisted single point cutting (EVASPC).

The mathematical formulation of EVASPC tool trajectory motion kinematics forms the foundation for predictable and repeatable implementations, and is also important in the rendering of CAD/CAM models. In the past, EVASPC-focused studies provided ‘local’ solutions to a research-specific cutting kinematics problem. For instance, a study presented by Zhang *et al.* demonstrated the impact that tool edge radius has on the surface profile through the development of a 2D model that simulates the corresponding surface topography [33]. Similarly, work detailed by Jianguo *et al.* demonstrated the effectiveness of cutting compensation methods in the general context of EVASPC [34]. More generally, researchers have relied on 2D and 3D simulations of surface topography in order to compare them with their physical correspondents [35]. Nonetheless, the proposed analytical/theoretical models all rely on the mathematical formulation of cutting tool path trajectory.

Building on this, the main objective of this chapter is to demonstrate the mathematical framework capable of integrating EVASPC. This framework is based on a geometrical representation of the tool motion, and will be used to generate geometric models of the

resulting surface topography and tool-workpiece cutting force interactions. The kinematic formulations will encompass the general equations of motion for EVC, essentially determined by the superposition between the slow motion of the CNC stage (SPC) and the ultrafast EV motions (EVC). Based on this, four different EVASPC implementations will be introduced, each driven by a different set of motion control parameters. Finally, an overview of the EVASPC cutting force model will be demonstrated through the detailed analysis of a modified Merchant's Circle model, providing the theoretical reasoning behind EVASPC's hypothesized cutting force reduction.

## 2.2 Geometrical modeling of EVASPC kinematics

EVASPC can be described through the mathematical formulation of the tool tip kinematics. There are two primary motions that form EVASPC—the CNC motion and the EVC motion. The multi-axis stage of the five-axis CNC machine is used to generate slow motion SPC kinematics that are characteristic of conventional cutting without EVC. The SPC is controlled by two main parameters, the cutting speed ( $V_{SPC}$ ) and the depth-of-cut ( $DOC$ ). By contrast, EVC motions are controlled externally by the EVC unit, generating elliptical motions with micron-scale amplitudes at kHz-scale frequencies.

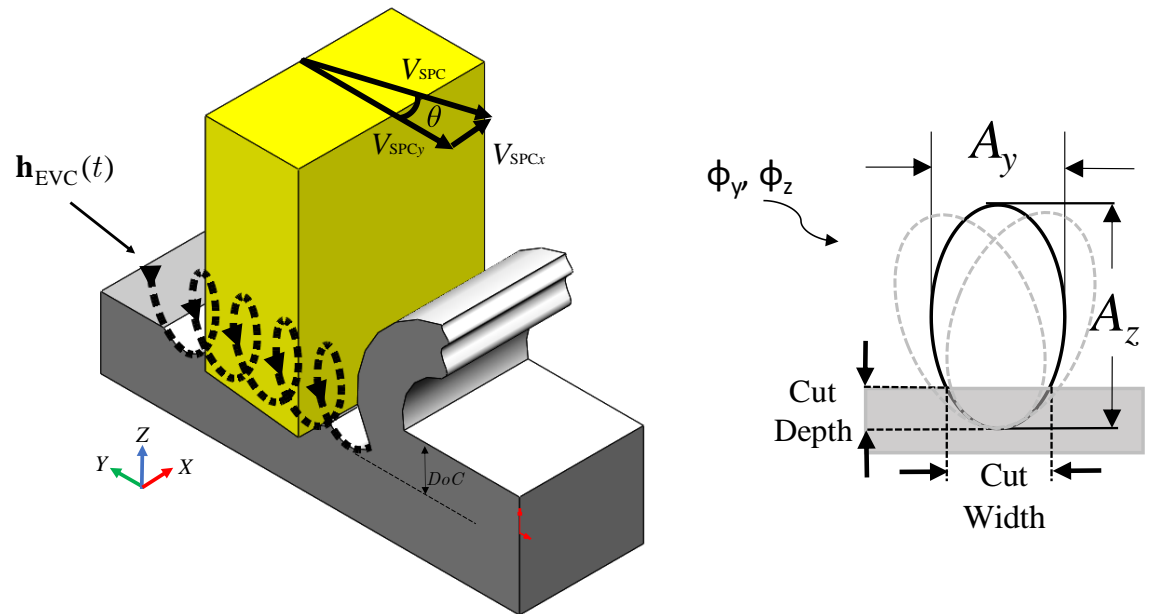


**Figure 2.1:** EVASPC kinematics obtained through the superposition of SPC and EVC.

The main role of the fast EVC motion is to introduce discontinuities in the tool-workpiece contact, and thereby convert the continuous cutting into a discontinuous one. The intermittent tool-workpiece contact ultimately leads to smaller cutting forces, reduced tool wear, and temperature gradients, all factors that essentially extend the applicability of EVC to ferrous and/or hard-to-cut materials.

The SPC components of motion,  $\mathbf{h}_{SPC}(t)$ , are detailed in Equation 2.1, where  $t$  represents time,

$$\mathbf{h}_{SPC}(t) = \begin{Bmatrix} x_{SPC}(t) \\ y_{SPC}(t) \\ z_{SPC}(t) \end{Bmatrix} = \begin{Bmatrix} V_{SPC} \cdot \sin(\theta) \cdot t \\ V_{SPC} \cdot \cos(\theta) \cdot t \\ DoC \end{Bmatrix} \quad (2.1)$$

The cutting speed ( $V_{SPC}$ ) is defined as the rate at which the SPC tool travels across the workpiece, and can either be constant or variable with respect of time. Similarly, the depth-of-cut ( $DoC$ ) refers to the depth at which the tool penetrates the workpiece in the  $-Z$  direction with-respect-to the uncut surface. An additional—yet rarely used—parameter termed as feed angle ( $\theta$ ) is defined between the direction of  $V_{SPC}$  and that of the plane containing the EV motion.

By contrast, the ultrafast EV motion component  $\mathbf{h}_{EVC}(t)$ , Figure 2.1, is introduced by means of an external motion generator as follows:

$$\mathbf{h}_{EVC}(t) = \begin{Bmatrix} x_{EVC}(t) \\ y_{EVC}(t) \\ z_{EVC}(t) \end{Bmatrix} = \begin{Bmatrix} 0 \\ A_y \cos(2\pi\omega t + \phi_y) \\ A_z \sin(2\pi\omega t + \phi_z) \end{Bmatrix} \quad (2.2)$$

According to Equation 2.2, EVC is a planar motion that remains in the  $Y$ - $Z$  plane, and is defined by three primary parameters. The horizontal and vertical amplitudes ( $A_y$  and  $A_z$ , respectively) are the primary variables associated with the elliptical motion. More specifically, the horizontal amplitude ( $A_y$ ) represents the amplitude in the direction parallel to the feed ( $V_{SPC}$ ), whereas the vertical amplitude ( $A_z$ ) is perpendicular to the feed, Figure 2.1. Both amplitudes can be constant in time (thus yielding uniform ellipses), or can be variable (thus enabling the amplitude modulation of EV motion). In addition to

the two amplitudes, the vibrational frequency of the EV motion ( $\omega$ ) is a parameter that is based on capabilities of the EV generator. Finally, the third defining parameter of the EV motion is the phase angle ( $\phi_y, \phi_z$ ) that defines the relative spatial orientation between  $A_y$  and  $A_z$ .

The combination of SPC and EVC as well as the relative positioning between the planes in which they occur cause the tip of the cutting tool to follow a trochoidal path Figure 2.1. Furthermore, Equation 2.3 integrates these two motions into a set of governing equations that covers all possible variants offered in this cutting technology.

$$\mathbf{h}(t) = \mathbf{h}_{SPC}(t) + \mathbf{h}_{EVC}(t) = \begin{Bmatrix} x(t) \\ y(t) \\ z(t) \end{Bmatrix} = \begin{Bmatrix} V_{SPC} \cdot \sin(\theta) \cdot t \\ V_{SPC} \cdot \cos(\theta) \cdot t + A_y \cos(2\pi\omega t + \phi_y) \\ DoC + A_z \sin(2\pi\omega t + \phi_z) \end{Bmatrix} \quad (2.3)$$

The overlap between SPC and EVC can be graphically represented as depicted in Figure 2.2.

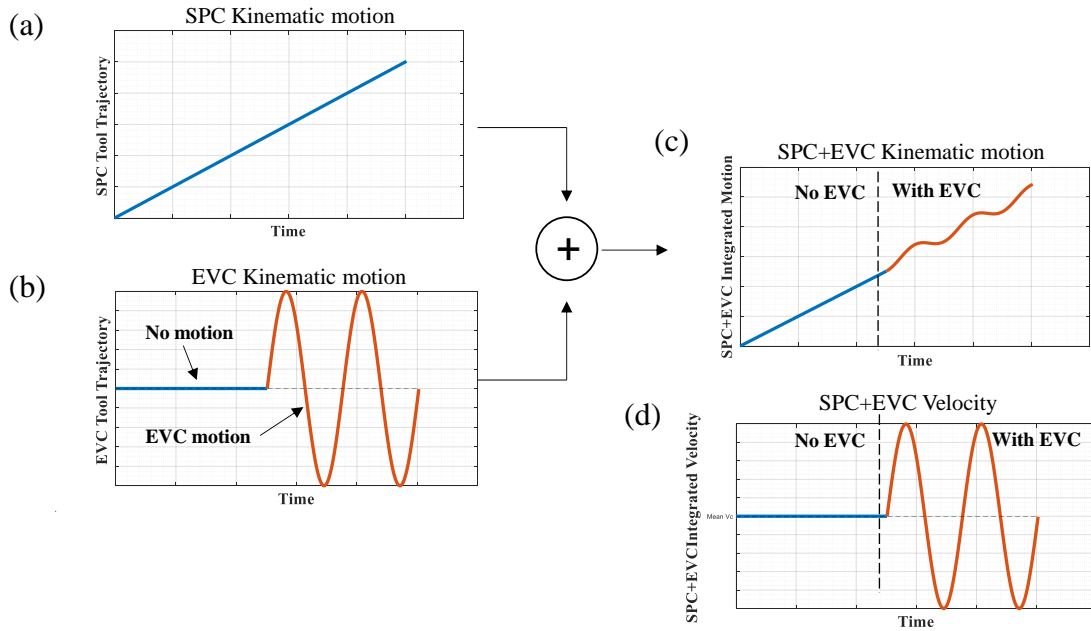


**Figure 2.2:** EVASPC motion characteristics: (a) No-EVC SPC kinematics, (b) EVC kinematics, (c) integrated EVASPC kinematics, and (d) integrated EVASPC velocity.

The summation of SPC and EVC motions in Figure 2.2(c) is transferred to the cutting tool tip, resulting in the overarching tool trajectory for EVASPC. Analysis of Figure 2.3

suggests three main phases of the EVASPC process, all modeled in the space domain, essentially as a function of length. The conversion between time ( $t$ ) and space ( $l$ ) domains is required because the final surface profile remains a space, rather than time characteristic. The first phase of the framework is responsible for the summation of the slow (SPC) and ultrafast (EVC) components of the motion that can be represented graphically through the trochoid shown in Figure 2.3

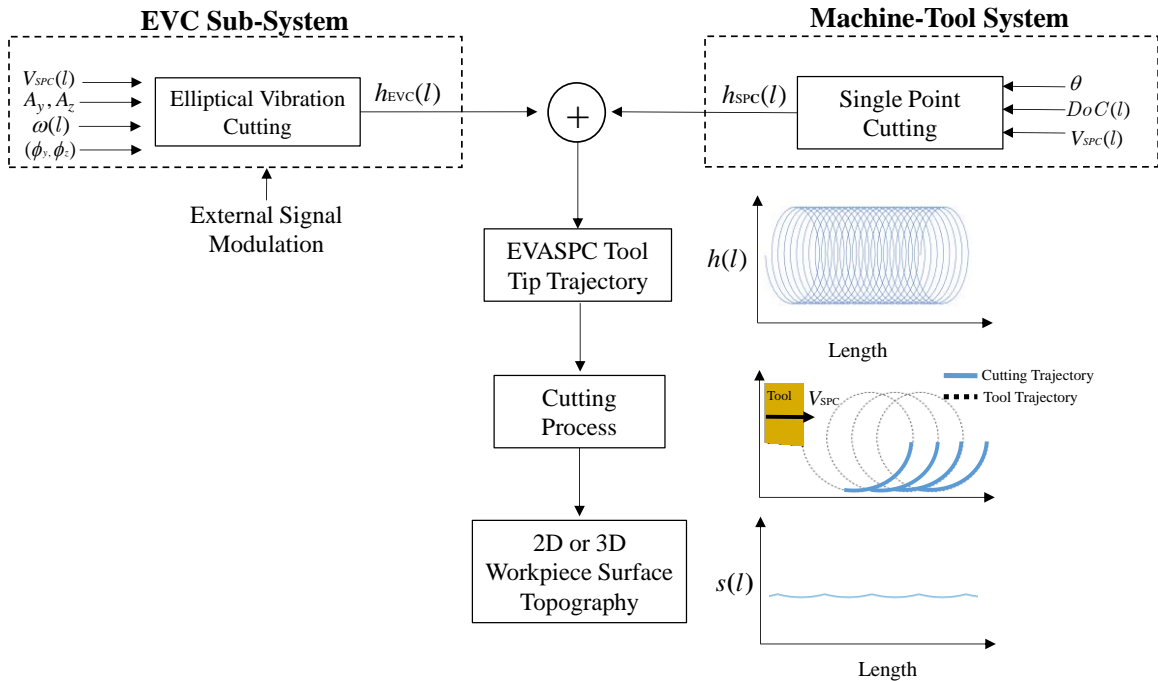


**Figure 2.3:** Flow diagram of the EVASPC kinematics.

Of note, the simple summation of terms ( $\mathbf{h}(l) = \mathbf{h}_{SPC}(l) + \mathbf{h}_{EVC}(l)$ ) used throughout the current study represents in fact only a simple geometric approximation that disregards the effect of cutting process stability on resulting surface topography. Additional complexity in the tool motion could be introduced through the consideration of transient tool-workpiece inference throughout the engaged period. However, the current model is considered an idealized trajectory, and such additional complexities remain a future extension of research. The second phase of the framework is concerned with the transformation of tool tip trajectory  $\mathbf{h}(l)$  into cut profile  $s(l)$ , a process that involves the

application of the dynamic characteristic [36, 37], where  $D$  is the differential operator of the cutting process ( $W(D)$ ). This phase is synonymous with workpiece fabrication and cutting force data acquisition. Finally, the resulting surface topography is generated as a function of the preceding process stages.

The inherent assumption behind the aforementioned consideration is that the trochoidal envelope of the tool is identically replicated in the workpiece. Nonetheless, when the attack angle of the tool into the workpiece is larger than the clearance angle, undesirable interferences will be present [33]. This situation can be mitigated through a judicious design of the cutting tool and EVASPC process parameters.

### 2.3 Implementations and applications of EVASPC

Based on EVASPC's governing equations of motion and process algorithm, the door is open for a variety of unique implementations and applications of this technology.

Table 2.1 identifies four primary implementations of EVASPC. Each implementation focusses on the control/modulation of a specific cutting parameter in Equation 2.3, and demonstrates the influence that such modulation has on the resulting tool motion, cutting process, and workpiece functionality. Note, the motion of the tool in the following four implementations remains in the Y–Z plane, and therefore no motion is produced in the X direction, reducing the  $x(t)$  component to zero.

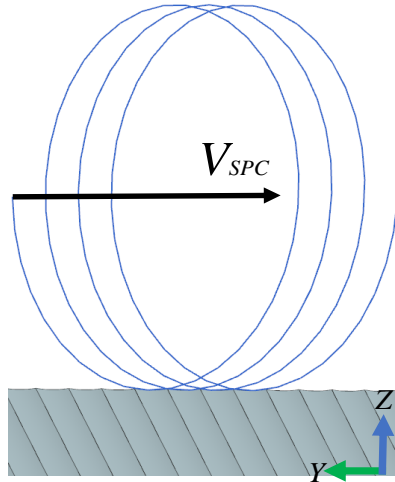
**Table 2.1:** Possible EVASPC implementations.

<b>EVASPC Parameters</b>						
Implementation	$V_{SPC}(l)$	$A_y, A_z$	$(\phi_y, \phi_z)$	$DoC(l)$	$\omega(l)$	$\theta$
1	<i>const</i>	<i>const</i>	<i>const</i>	<i>const</i>	<i>const</i>	0
2	<b><i>var</i></b>	<i>const</i>	<i>const</i>	<i>const</i>	<i>const</i>	0
3	<i>const</i>	<b><i>var</i></b>	<i>const</i>	<i>const</i>	<i>const</i>	0
4	<i>const</i>	<i>const</i>	<b><i>var</i></b>	<i>const</i>	<i>const</i>	0

The first implementation can be obtained by simply keeping all SPC and EVC parameters in Equation 2.3 constant, and limiting tool motion to the Y–Z plane, Figure 2.4. This will lead to spatially uniform structures and consistent surface topography, as shown in the



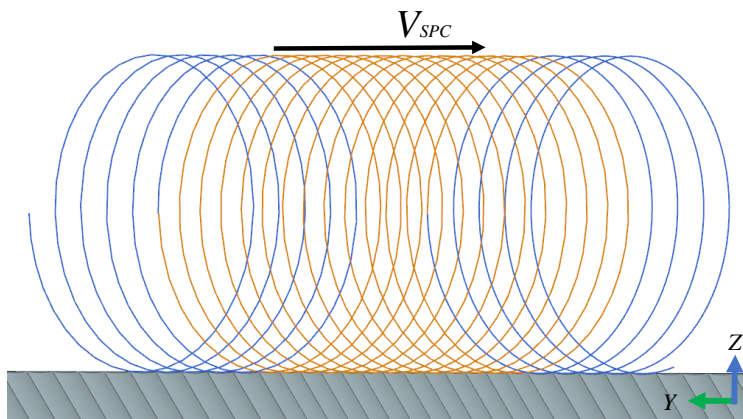
past through the fabrication of optical quality surfaces [14]. The optimal application of this strategy consistently produces high-quality surface finishes for the creation of low roughness and mirror-like surfaces [38].



$$\begin{aligned}x(t) &= 0 \\y(t) &= V_{SPC} \cdot t + A_y \cos(2\pi\omega t) \\z(t) &= DoC + A_z \sin(2\pi\omega t)\end{aligned}$$

**Figure 2.4:** Constant cutting conditions (Implementation 1).

The second implementation—demonstrated by Yang *et al.* [24]—assumes a linear variation of the cutting speed ( $V_{SPC}$ ) while keeping all remaining cutting parameters constant, and in turn, allows for the introduction of areally distributed cusp frequency modulation, Figure 2.5. This option is applicable to implementations such as multi-coloured paint-free surfaces, controlled surface wettability, and the fabrication of planar microfluidic systems that use hydrophobic and hydrophilic areas.



$$\begin{aligned}x(t) &= 0 \\y(t) &= \boxed{V_{SPC}(t)} \cdot t + A_y \cos(2\pi\omega t) \\z(t) &= DoC + A_z \sin(2\pi\omega t)\end{aligned}$$

$$\underline{V_{SPC}} > \underline{V_{SPC}}$$

**Figure 2.5:** Modulated cutting speed (Implementation 2).

The third implementation relies on the control of the elliptical vibration amplitudes ( $A_y, A_z$ ), consequently modulating the *DoC* and/or cusp height across the cutting area while keeping all other cutting parameters constant, Figure 2.6. This approach has been used in the past to create sinusoidal, ramp, and zig-zag surface geometries [33], micro-channeling [39], surface wettability [17], micro-dimpling [21], and paint-free surface colouration [24].

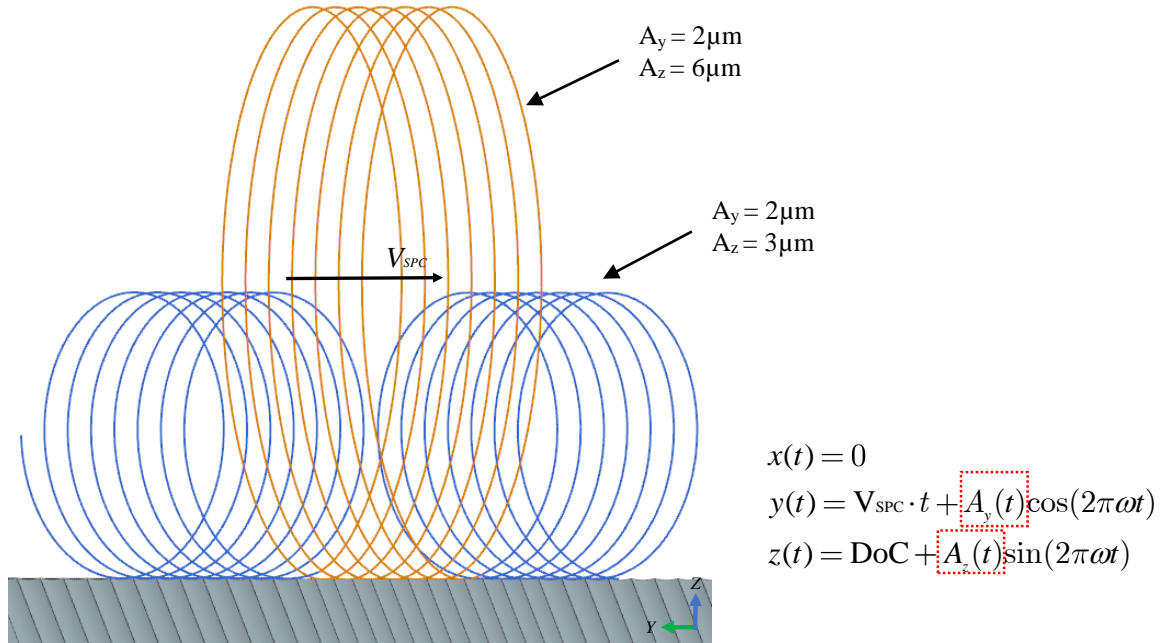


**Figure 2.6:** Modulated EV amplitudes (Implementation 3).

The fourth strategy—arguably the most difficult and advanced strategy encompassed by Equation (2.3)—involves the modulation of ellipse orientation. This can be achieved by modifying the phase shift between horizontal and vertical amplitudes of the ellipse ( $\phi_y, \phi_z$ ), ultimately, changing its orientation from forward-tilted, to vertical or even back-tilted, Figure 2.7. This implementation facilitates the generation of periodical structures with directional control of their inclination [17]. The persistent efforts of Guo *et al.* continues to demonstrate the positive influence that phase shift has on the creation of functional optical surface structures such as paint-free colouration [25] and holographic structuration [26].

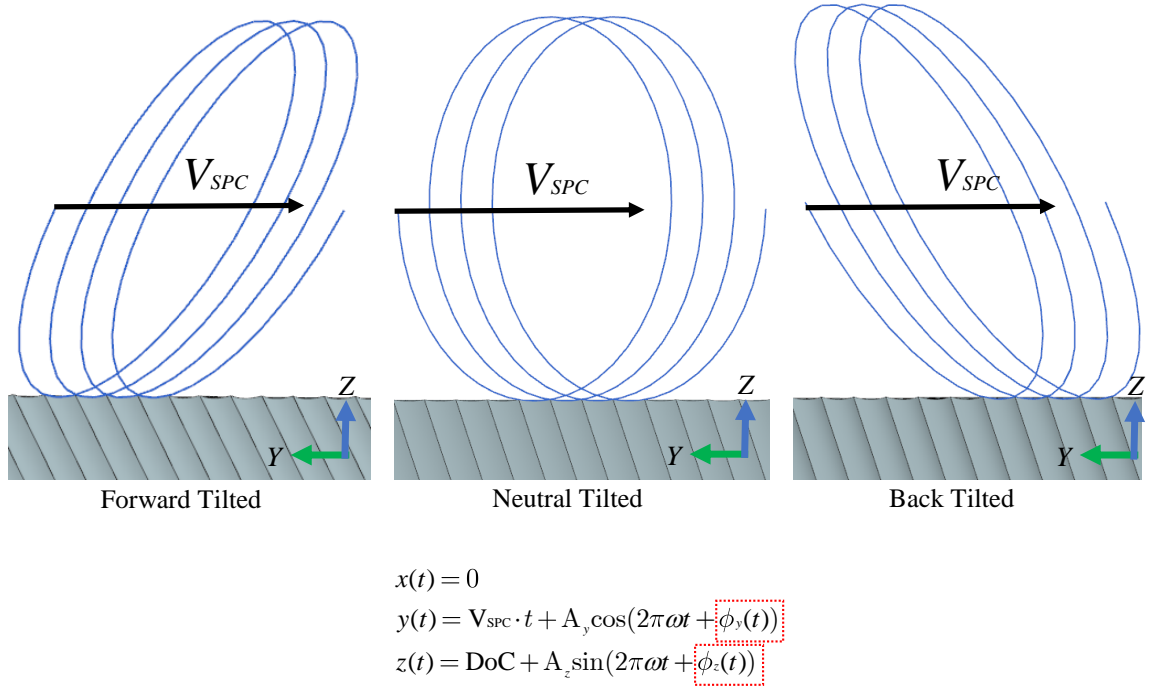


**Figure 2.7:** Modulated phase shift (Implementation 4).

While the four implementations described above have been the research topic of countless EV assisted single point cutting publications, it should be mentioned that this is by no means an exhaustive list. That being said, the following chapters will analyze the influence that a select number of the available EVC parameter (Equation 2.3) have on fabrication processes such as surface topography and cutting forces.

## 2.4 EVASPC cutting force model

A fundamental approach that is used to investigate the cutting mechanics of EVASPC involves the Merchant's Circle [40]. This model describes the cutting force components developed at the chip-tool interface. It should be noted here that the Merchant's Circle is primarily applicable to orthogonal SPC processes in which the rake face is the only face of the tool that is in contact with the workpiece.

In this context, the CF model is completed by analyzing reaction force components at the tool-workpiece interface. While force component magnitudes and directions are ultimately a result of the shear strain rate and the material properties, these effects can also be influenced through the cutting parameters used. Essentially, the CF diagram can

be split into two components, one driven by the axial tool motion (characterized by the cutting speed,  $V_{SPC}$ ) and the other by the shear properties of the workpiece material.

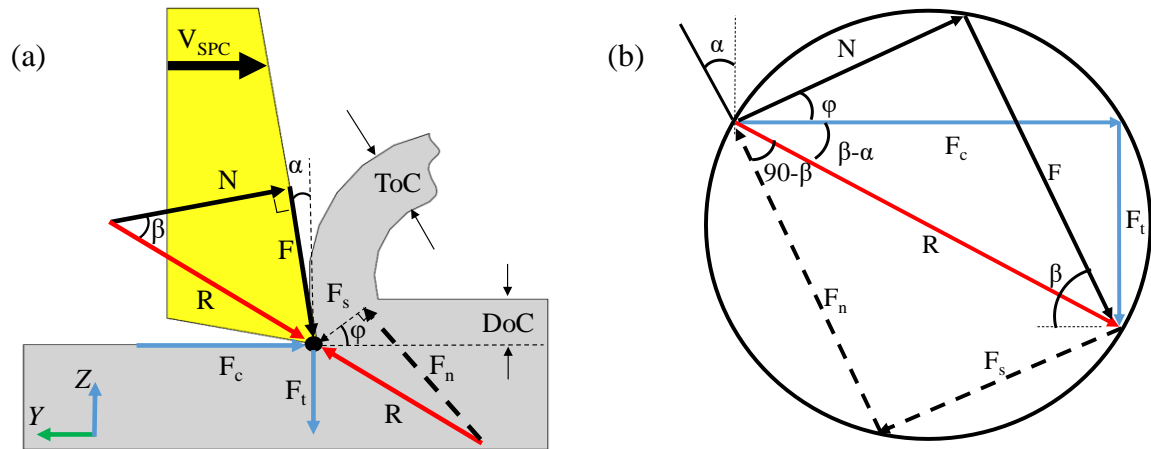


**Figure 2.8:** Cutting force model for conventional SPC: (a) Forces developed at tool-workpiece interface, and (b) corresponding Merchant's circle for free orthogonal cutting.

When it comes to the CF model for conventional no-EVC cutting, tool kinematics are characterized by user-controlled variables such as the cutting speed of the tool ( $V_{SPC}$ ) and the depth-of-cut ( $DoC$ ). Consequently, the principal cutting ( $F_c$ ) and thrust ( $F_t$ ) forces (blue vectors in Figure 2.8) can be defined as the primary forces required to overcome the friction force  $F$ , as well as the shear force ( $F_s$ ) that opposes tool motion direction. The accurate determination of  $V_{SPC}$  and  $DoC$  has a large effect on the magnitude of cutting and thrust forces developed during cutting. However, an additional level of control comes from the tool geometry itself, more specifically the rake angle ( $\alpha$ ). This angle tends to have a large influence on the orientation and magnitude of the force.

On the other hand, the CF model is also influenced by tool-workpiece interaction via shear deformation properties of the material. To explain this, it is reiterated here that the rake angle ( $\alpha$ ) is crucial when it comes to both cutting force and shear components of the CF circle diagram. More specifically, the rake angle determines the direction of the frictional force ( $F$ ), except  $F$  runs in a direction that opposes chip motion (Figure 2.8). Following this, the resultant force  $R$  can be defined as the vectoral sum between  $F$  and  $N$  (a normal to  $F$  force). As suggested by Figure 2.8,  $R$  constitutes the common element

between the CF and shear deformation halves of the circle. The shear deformation-driven CF triangle is geometrically determined by the resultant  $R$  and shear angle  $\varphi$ , from which the shear force ( $F_s$ ) is determined (black dashed lines in Figure 2.8).

All these considerations allow for the theoretical determination of both cutting ( $F_c$ ) and thrust ( $F_t$ ) force components. In more general terms, the forces produced through the conventional cutting (CC) are dependent on the cutting coefficient ( $K$ ) as well as the constant nominal cutting area ( $A_{cc}$ ). According to prior studies [41, 42], the cutting coefficient is dependent on the cutting speed ( $V_{SPC}$ ), depth-of-cut ( $DoC$ ), rake angle ( $\alpha$ ), and constant nominal cutting area ( $A_{cc}$ ), Equation 2.4.

$$F_{cc} = K(V_{SPC}, DoC, \alpha) \cdot A_{cc} \quad (2.4)$$

On the other hand, cutting force models associated with the EVC process adds another level of complexity to the conventional Merchant's Circle by essentially incorporating the time-dependency. While  $V_{SPC}$ ,  $DoC$ ,  $\alpha$  and other cutting parameters described in the preceding section remain constant, the addition of the ultrafast elliptical motion and its inherently interrupted contact produce a more intricate CF analysis.

In the EVASPC case, the major source of cutting force reduction is represented by the intermittent contact between tool and material. This type of interaction is repeated for each elliptical revolution of the tool, a motion fully contained in the vertical plane.

During each elliptical revolution, the duration of the disengaged phase has beneficial effects not only on the magnitude of the CF, but also on chip removal and heat dissipation. The elliptical motion of the cutting tool was described earlier this chapter through Equation 2.3.

The additional complexity brought by EVC on the Merchant's Circle can be explained by means of the two phases associated with the elliptical cutting cycle: conventional kinetic friction zone and reversed friction zone [29]. As shown in Figure 2.9, these two distinct phases are tightly connected with the elliptical path of the tool.

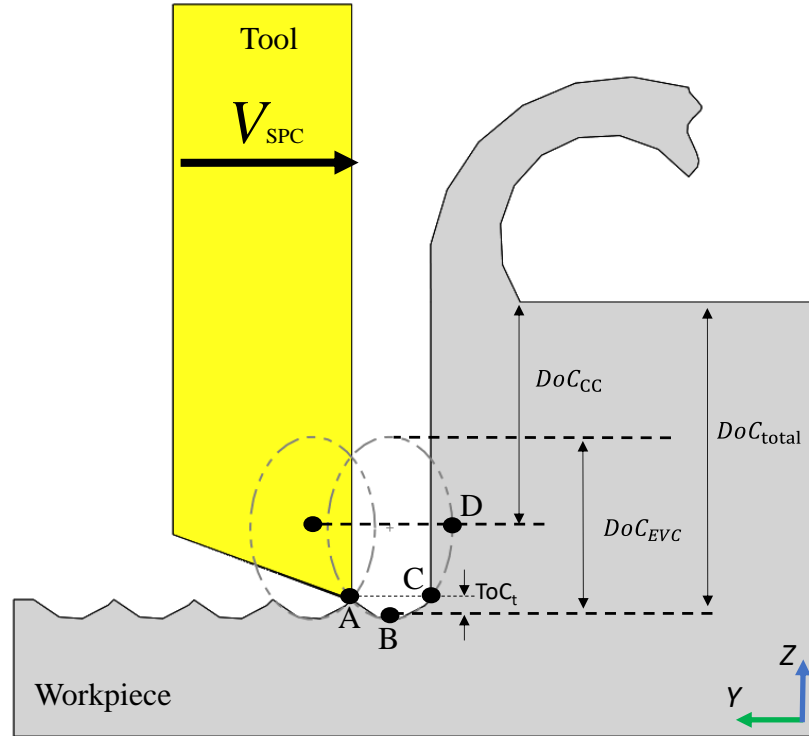


**Figure 2.9:** The two EVC phases/tool motion intervals: 1. Kinetic friction zone (A to C), and 2. Reversed friction zone (C to D).

During the first stage, the conventional kinetic friction zone occurs from point A (initial contact between the tool and workpiece) and lasts until C, where cutting and frictional forces oppose each other, same as in conventional cutting (Figure 2.10).

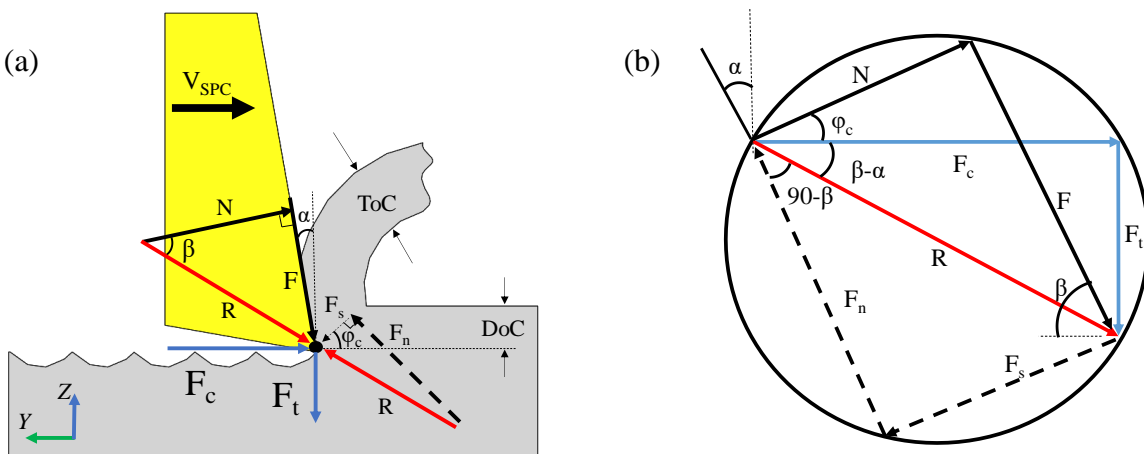


**Figure 2.10:** Cutting forces in the kinetic friction phase of EVC: (a) Forces developed at tool-workpiece interface, and (b) revised Merchant's circle.



As such, the resulting cutting force equations can be expressed through the introduction of a transient force equation that captures the orientation of the force vectors in kinetic friction, transition, and reverse friction zones:

$$F_{EVC} = K(V_{SPC}, DoC, \omega, A_{cc}, \alpha) \cdot A_{EVC} \quad (2.5)$$

$$A_{total} = A_{cc} + A_{EVC} \quad (2.6)$$

$$DoC_{total} = DoC_{cc} + \frac{1}{2} DoC_{EVC} \quad (2.7)$$

According to Equation 2.5–2.7, cutting forces developed during the cutting of micro V-grooves depends on cutting speed ( $V_{SPC}$ ), depth-of-cut ( $DoC$ ), EV frequency ( $\omega$ ), rake angle ( $\alpha$ ), nominal constant cutting area ( $A_{cc}$ ), and the variable cutting area ( $A_{EVC}$ ).  $A_{cc}$  represents the constant cutting area determined through the conventional/non-EVC cutting process, whereas  $A_{EVC}$  is based on the cyclical motion introduced by EVC and varies throughout the elliptical period (Figure 2.9).

## 2.5 Summary and conclusions

The defining principles of EVC come from the advanced elliptical tool trajectory motion introduced to the cutting process. Understanding the influence that each process parameter has on the cutting motion is crucial to predicting the resulting functional application of the fabricated workpiece. This chapter outlined a detailed analysis of the EVASPC motion kinematics along with four implementations of this technology. Additionally, the modified Merchant's Circle CF model provided an explanation of the EVC-induced cutting force reduction based on tool-workpiece interaction via shear deformation properties of the material along with the influence that cutting parameters have on force vector orientations. Experimental hypotheses in the following chapters will be synthesized based on these analytical models, and will be frequently reflected on.



## Chapter 3

### Cutting Force Reduction by Elliptical Vibration Assisted Cutting

A revised version of this chapter has been accepted as: Farrus, N., Joao, D., Milliken, N., Tutunea-Fatan, O.R., & Bordatchev, E. V., 2019. Reduction of cutting forces by elliptical vibration in multi-pass ultraprecise single point axial cutting of V-grooves. *Procedia Manufacturing*, 48, pp. 570-578.

## **3 Cutting Force Reduction by Elliptical Vibration Assisted Cutting**

### **3.1 Overview**

Following the analytical modeling of EVASPC processes, this study aimed to demonstrate the positive effect of EVC motions on cutting force reduction and stabilization. For this purpose, a series of cutting trials involving the fabrication of micro V-grooves by means of ultra-precise single point cutting (USPC) was performed using an axial multi-pass cutting strategy with constant cutting area. The influences and advantages brought by EVC over the conventional ‘no-EVC’ USPC scenario were initially assessed by means of cutting mechanics and experimental results.

### **3.2 Background**

V-grooves are plain geometrical features that play a critical functional role in a wide variety of industrial applications covering uniform area illumination and light guiding optics in automotive lighting [43], conventional Fresnel lenses [44], optical concentrators and sunlight trapping structures for solar energy harvesting [45], surface functionalization for controlled wettability [46], and aerodynamics [47]. These functional surfaces are typically manufactured at mass production rates and over large surface areas, and therefore steel tooling (inserts, dies, molds, stamps, etc.) is required. Microfabrication of V-grooves with high accuracy, precision, and surface quality has been demonstrated in the past [48], but it is typically limited to non-ferrous materials using rotational and non-rotational diamond cutting tools and high-precision processes such as diamond drum turning [49], single point cutting [10, 50], micro-milling [51], flycutting/raster milling [52], and planing [53]. As discussed, workpiece material limitations have been surpassed through the introduction of EVC, and has also enabled the fabrication of V-grooves, micro/nano-optical structures and functional surfaces in ferrous steel and alloys, difficult-to-cut, ceramic, fragile and exotic materials [54].

The microfabrication of V-grooves across flat surfaces is a relatively newer area of research that is primarily concerned with the reduction of cutting forces as well as

enhancements of surface structure accuracy and quality. By contrast, limited studies are directly focused on the more practical aspects of the cutting process optimization to include chip formation [55], variations in the elliptical cutting locus and excitation frequency [9], critical depth-of-cut (DoC) [56], and V-groove cutting process planing [57]. In this regard, past studies have already shown that the EVC process changes the shear flow inside the chip, chip thickness, and chip radius of curvature, concurrently reducing cutting forces (by 10% at 65 kHz) [55]. Furthermore, significant improvements in the form accuracy of burr-free micro V-grooves can be achieved by means of low cutting forces, particularly since EVC suppresses the plastic deformation of the workpiece. A non-contact index involving the vibration amplitude of the elliptical locus, the cutting speed and the excitation frequency was introduced [9] to define a contact/no-contact cutter-workpiece cycle. The EVC process was also studied with different values of the non-contact indices, and it was found that the surface roughness in the feed direction is proportional to the vibration amplitude in the thrust direction and the square of the feed speed. DoC plays a critical role in obtaining a stable cutting state, resulting in a continuous chip [56]. This can be achieved with a minimum (critical) DoC, analyzed with respect to a cutting force ratio ( $F_y/F_z$ ), chip shape, surface roughness, and surface hardening. The complexity of the EVC process significantly increases when cutting V-grooves by means of multi-pass process planing [32, 57, 58]. During multi-pass EVC, it is important to recognize and pay attention to changes in the cutting force components (principal, thrust, and friction) that are affected by a contact area that is unevenly distributed across cutting edges. Taking this into account, EVC process stability and effectiveness can be implemented either with a constant DoC or with a constant cutting area that is essentially targeting a constant cutting force level.

This study exemplifies the capabilities of USPC [32], performed by means of a monocrystalline diamond tool as used during the multi-pass micromachining of high-accuracy V-grooves characterized by an optical surface quality. In this regard, the ultimate objective of this study is to demonstrate the effect of elliptical vibrations on cutting force reduction, and will be investigated in the context of an axial cutting strategy performed with constant cutting area.

### 3.3 Axial strategy for single point cutting of V-grooves with constant cutting area

The axial cutting strategy utilized in this work consists of an axially-translating cutting tool that gradually plunges into the workpiece material over a number of cutting passes while maintaining constant cutting area. An overview of the cutting kinematics of this strategy is shown in Figure 3.1. During V-groove fabrication, every cutting pass is run across the workpiece with a specific-to-pass depth in the  $-Z$  direction until the final desired DoC was achieved (Figure 3.1(a)). As the name of the strategy implies, while cutting area remains constant, the depth-of-cut and chip thickness will follow an inverse proportionality dependence. This means that in order to fulfill the constant cutting area constraint, the cutting force will be distributed over the lateral edges of the tool (Figure 3.1(b)).

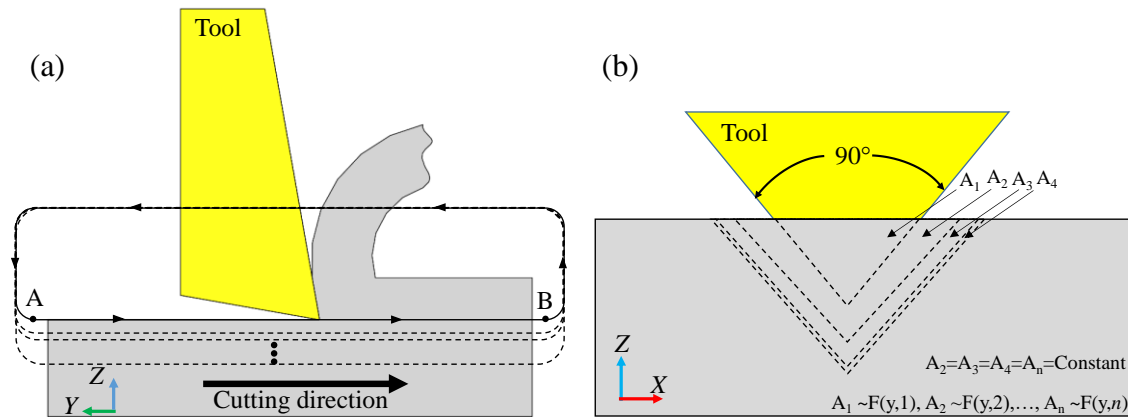


**Figure 3.1:** Cutting kinematics of V-groove fabrication via SPC: (a) Single passes along  $-Y$  direction, and (b) multi passes in  $-Z$  direction [59].

The motion tracked by the SPC tool in this process is characterized by a rather low complexity. In brief, the tool plunges in the  $-Z$  direction to the desired DoC and then moves across the workpiece in the  $-Y$  direction at a constant cutting speed until it reaches the end of the toolpath, Point B in Figure 3.1(a). Here, the tool lifts above the workpiece and returns to its starting position (Point A), readying itself for the next pass. This cycle is repeated for a desired number of tool passes until the final depth of the groove is achieved.

The theoretical approach used to investigate the cutting mechanics of EV assisted USPC for V-groove fabrication involves Merchant's Circle [40], as seen in Chapter 2. This model describes the cutting force components developed at the chip-tool interface. It should be noted here that the Merchant's Circle is primarily applicable to orthogonal cutting processes in which the rake face is the only face of the tool that is in contact with the workpiece. The constant cutting area USPC strategy used in V-groove fabrication involves additional contact on the flanks of the cutting tool, such that the Merchant's model must be modified in order to sufficiently capture cutting force (CF) generation accurately (Figure 3.2). To utilize this orthogonal CF model for V-groove fabrication, the cutting edge has to be discretized into small elements, each representing an instance of the micro-orthogonal cutting process, Figure 3.2(b). Following this, each elemental section can then be solved individually by means of the original Merchant's Circle method. Finally, the combination all such discrete instances will provide an accurate general CF model, Figure 3.2(c).

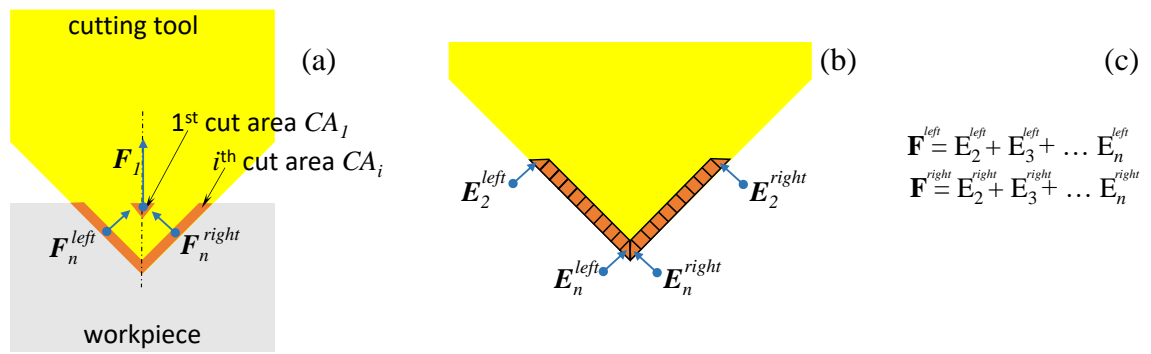


**Figure 3.2:** Modified Merchant's Circle method for representing V-groove fabrication: (a) Cutting force distribution for cutting passes 1 to  $n$  [59], (b) discretize cutting force distribution for individual Merchant's Circle analysis, and (c) summation of discretized elements to achieve general cutting force model.

The major source of cutting force reduction is represented by the intermittent contact between tool and material which is repeated for each elliptical revolution of the tool. During each elliptical revolution, the duration of the disengaged phase has beneficial effects not only on the magnitude of the cutting force, but also on chip removal as well as heat dissipation.



The second phase is associated with the reversed friction zone where both frictional ( $F$ ) and cutting ( $F_c$ ) forces have somewhat similar directions, Figure 3.4. This situation is a consequence of the fact that tool motion happens in the direction of the chip that is being formed. As such, it appears that cutting force reduction is the result of both the diminished contact time between tool and workpiece as well as the change/reversal of frictional force direction.

In summary, from the above model, it is reasonable to expect that the overall average cutting forces will be reduced when EVC is active since the tool is only intermittently in contact with the workpiece for each elliptical revolution of the tool.

### **3.4 Experimental setup and data processing methodology**

In order to measure, record, and analyze the actual cutting force components over time and space domains, a previously developed experimental setup [32] was augmented to enable experiments with integrated EVC motions, such that enhancements by means of EVASPC could be observed (Figure 3.5). The experimental setup was based on a high-performance/high-precision multi-process 5-axis micromachining center MicroGantry nano5x manufactured by Kugler GmbH. The external EVC unit EL-50Σ, manufactured by TAGA Electric Co., Ltd. was mounted vertically on the Z-axis with the ability to move only along the Z-axis. Horizontal and vertical elliptical vibrations of the cutting tool tip were fully controlled by means of an electrical controller and power amplifiers.

The workpiece, made of aluminum alloy 6061, was mounted onto the Kistler 9256C-2 multicomponent dynamometer and attached to a tilt-swivel unit of the 5-axis micromachining center, allowing 4-axis motions of the workpiece. This dynamometer was capable of capturing 3-component force measurements up to  $\pm 250$  N, from which point the three corresponding XYZ charge amplifiers converted the charge signals into output voltages, proportional to the cutting forces. While the accuracy of the dynamometer is predominantly dependent on the calibration method, the sensitivity for this experiment was specifically controlled in each force component direction, with sensitivity in the X direction of 13 pC/N, and 26 pC/N in the Y and Z directions. The

increased sensitivity in the Y and Z direction was required due to the principal cutting force magnitudes being captured in these components.

### Experiment Setup

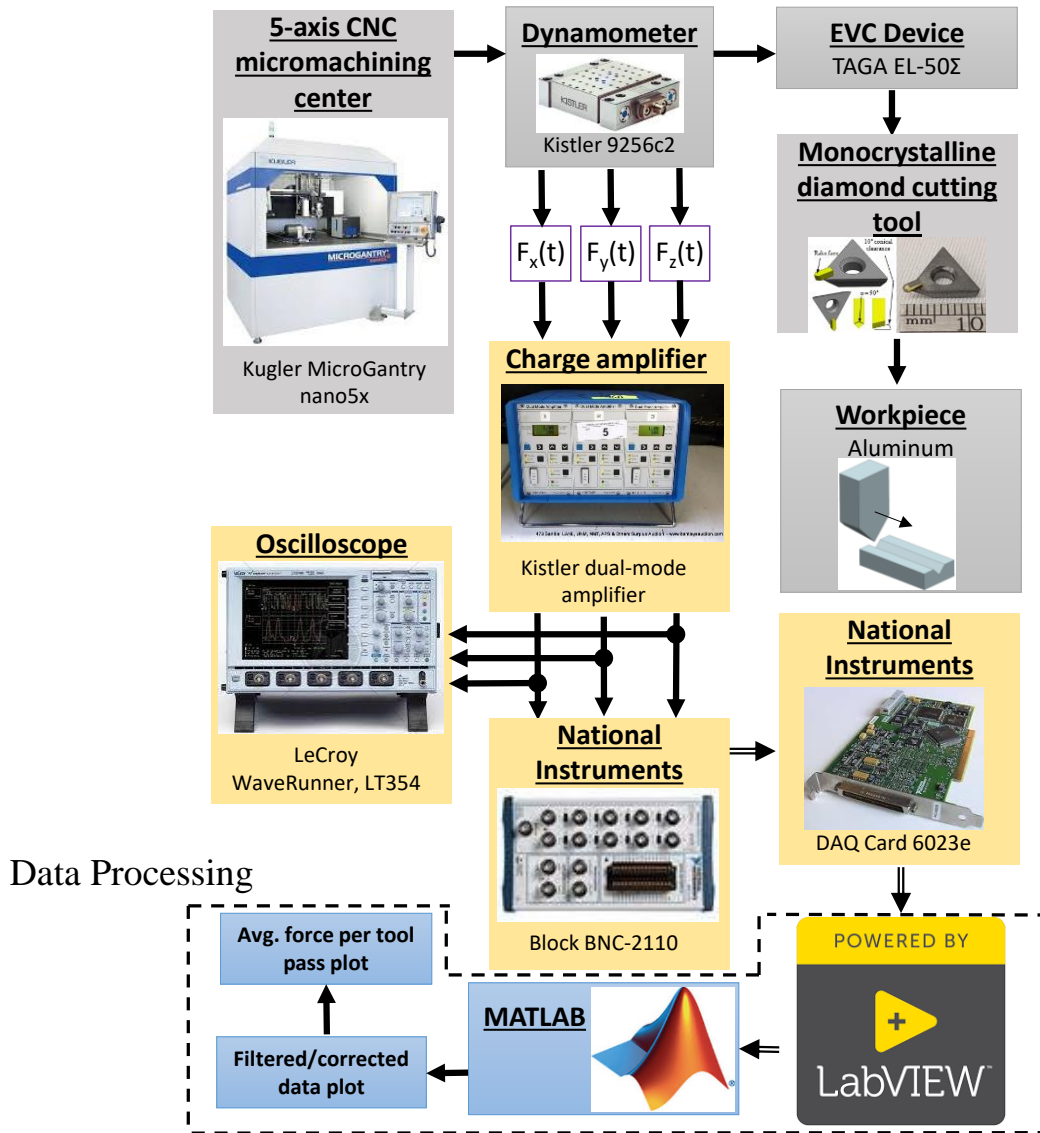


**Figure 3.5:** Experimental setup and data processing workflow.

During cutting experiments, the tool performed a total of 44 passes across the 10 mm long workpiece until a final DoC = 250  $\mu\text{m}$  was obtained. For each cutting pass, all parameters listed in Table 3.2 were kept constant—with the exception of the DoC that varied to maintain a constant cutting area (Figure 3.1). The DoC for each pass was calculated by means of trigonometric formulas presented by Joao *et al.* [58]. Spatial



cutting force components  $\{F_x(t), F_y(t), F_z(t)\}$  were measured by the dynamometer for each pass, and were subsequently converted into corresponding electrical signals by three Kistler 5010 dual mode charge amplifiers (one amplifier per cutting force component). After that, electrical signals were digitized by a National Instruments 6023e data acquisition card with a sampling frequency of 2 kHz and displayed in real-time through an in-house LabVIEW program, such that the cutting process could be monitored instantaneously. In parallel, the amplified cutting force data was saved onto a computer in the form of a LabVIEW *.lvm* file type for further data processing.

The time-dependent cutting force components  $\{F_x(t), F_y(t), F_z(t)\}$  were then initially filtered by means of a MATLAB software and in-house developed post-processing script. To investigate the quasi-static components of the cutting forces, a MATLAB-based moving-average low-pass filter was used to filter/smooth the acquired data. This filter used a window size of 200 data points and a sampling frequency of 2 kHz, matching the sampling rate of the experimental DAQ system. Furthermore, the drift introduced by the dynamometer and corresponding charge amplifiers was eliminated from the data for each of the cutting force components. This was done using a second-order polynomial fitting curve that followed the raw cutting force data profile, from which point the drift offset was subtracted, resulting a zero offset force curve. Finally, the digital signature of the cutting force components was separated with respect to individual tool motions/passes and then average cutting forces per pass were calculated.

The main objective of the EVC experiments performed in the context of this study was to investigate the influence of elliptical vibrations on the cutting force developed during the multi-pass fabrication of V-grooves. Therefore, cutting experiments were performed both with and without EVC motions active. The axial V-groove cutting strategy with constant area was intentionally selected to ensure a high repeatability of the experimental results with respect to the desired constant/quasi-constant cutting forces.

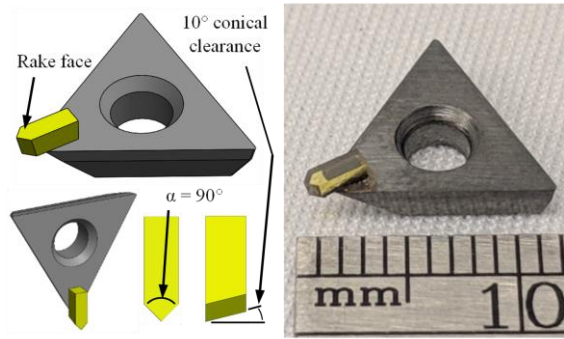


**Figure 3.6:** Triangular monocrystalline single point diamond cutting tool [59].

A triangular-shaped monocrystalline single point diamond cutting tool was used for experiments (Figure 3.6). The cutting tool had an included angle of  $90^\circ$ , a rake angle of  $0^\circ$ , and a clearance angle of  $10^\circ$ . The  $90^\circ$  included angle allowed the fabrication of axially symmetric V-grooves characterized by a symmetric cutting area shape and thereby symmetric cutting forces across the cutting face. Special attention was dedicated to the clearance angle of  $10^\circ$  since it introduced a limitation in the selection of the EVC parameters (e.g. horizontal and vertical amplitudes). More specifically, the clearance angle limited the magnitude of the cutting speed in order to avoid frictional contact between the flank face of the cutting tool and that of the cut surface.

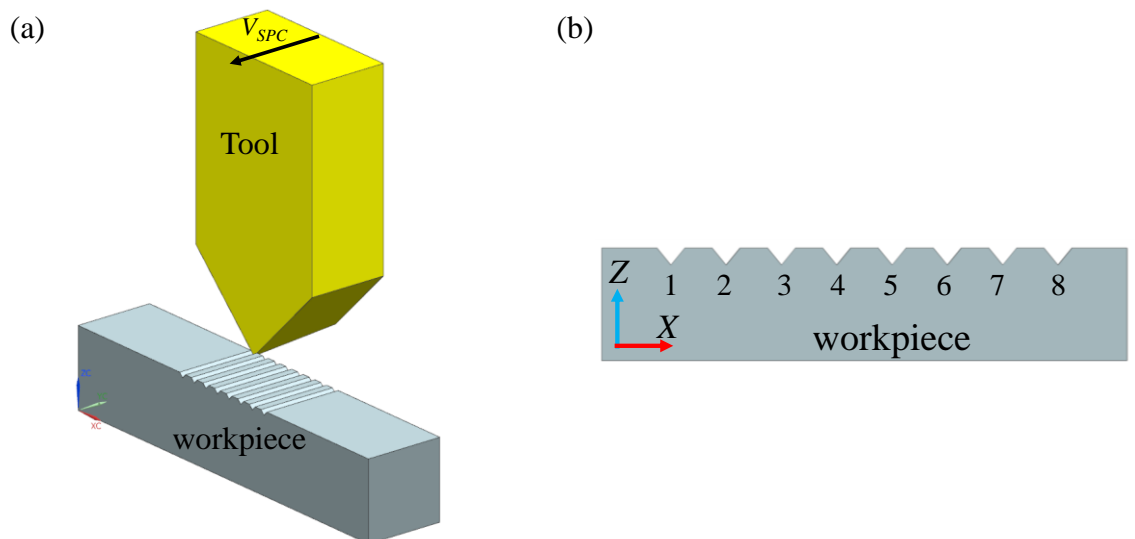


**Figure 3.7:** V-groove fabrication overview: (a) Isometric representation of experimental tool-workpiece setup, and (b) groove numbering corresponding to experiment number.

The following experiment was repeated a total of eight times in order to capture the influence that unique combinations of EV amplitudes have on the cutting force generation. Table 3.1 demonstrates the specific combinations of horizontal amplitudes ( $A_y$ ) and vertical amplitudes ( $A_z$ ) used for each experiment, and can be visualized in Figure 3.7. The elliptical amplitudes ranged from 2  $\mu\text{m}$  to 6  $\mu\text{m}$ , covering a large range of capabilities offered by the EL-50 $\Sigma$  EVC elliptical control unit. Additionally, EV ellipse dimensions spanned from the extreme vertical-dominant orientation, as seen in Experiment 6 ( $A_y = 2 \mu\text{m}$  and  $A_z = 6 \mu\text{m}$ ), to the extreme horizontal-dominant orientation, as seen in Experiment 8 ( $A_y = 6 \mu\text{m}$  and  $A_z = 2 \mu\text{m}$ ). This array of EV amplitude-based experiments (Experiments 2 to 8) were ultimately compared to the ‘no-EVC’ trial in Experiment 1, in order to analyze the comparative cutting forces produced, not only between ‘no-EVC’ and ‘with-EVC’ cutting, but also between individual EV amplitudes.

**Table 3.1:** Elliptical vibration amplitude experiment parameters.

Experiment	Horizontal Amplitude, $A_y$ ( $\mu\text{m}$ )	Vertical Amplitude, $A_z$ ( $\mu\text{m}$ )
1	N/A	N/A
2	2	2
3	4	4
4	6	6
5	4	6
6	2	6
7	6	4
8	6	2

### 3.5 Cutting forces during multi-pass micromachining of V - grooves performed with and without EVC motions

Several V-groove cutting trials were performed with and without the use of EVC (Table 3.1) in order to compare actual cutting forces and their quasi-dynamics. The pre-trial surface of the sample was brought to an ultra-finished state by means of diamond cutting in order to ensure its planarity and quality (two important prerequisites for the repeatability of the tests to be performed). The peak-to-valley waviness of the surface was assessed to be below 400 nm. The sample was aligned with the cutting direction (by

enforcing a deviation of under  $0.5 \mu\text{m}$ ) to ensure a uniform DoC along each cutting pass. In addition, V-grooves were placed more than  $500 \mu\text{m}$  from each other in order to avoid confounding effects caused by deformations of the lateral V-groove walls.

A detailed analysis of two selected experiments was completed, and the machining parameters are presented in Table 3.2. The first experiment, Experiment 1, consisted of conventional SPC V-groove fabrication, without EV activated, using cutting parameters in Table 3.2—omitting  $A_y$  and  $A_z$ . The second experiment, Experiment 8, utilized EVC amplitudes  $A_y = 6 \mu\text{m}$  and  $A_z = 2 \mu\text{m}$ , with additional constant cutting parameters as seen in Table 3.2. These values were based on a number of anterior trials attempting to determine the combination of amplitudes yielding larger/more significant CF reductions.

**Table 3.2:** Cutting trial parameters.

Parameter	Value
Cutting speed (mm/min)	500
Final chip thickness ( $\mu\text{m}$ )	2
Vibrational frequency (kHz)	41
Final depth of cut ( $\mu\text{m}$ )	250
Groove length (mm)	10
Vertical amplitude, $A_z$ ( $\mu\text{m}$ )	2
Horizontal Amplitude, $A_y$ ( $\mu\text{m}$ )	6
Rake angle, $\alpha$ ( $^\circ$ )	0
Workpiece material	Aluminum alloy 6061
Coolant	Isoparaffin mist

To analyze average cutting forces, a mid-depth V-groove pass was used (*i.e.*, pass 22 of the total 44 passes required to generate the entire V-groove). This selection ensured a stable cutting regime and thereby the acquisition of reliable data. The analyzed pass was characterized by  $DoC_{cc} = 4 \mu\text{m}$  and  $DoC_{EVC} = 1 \mu\text{m}$ . An overview of all eight experiments are visible in Figure 3.8, and it is immediately evident that the introduction of EVC significantly reduces cutting forces by as much as 94.5% in the cutting direction

( $F_y$ ), Figure 3.8(a). This being said, the thrust component ( $F_z$ ) demonstrated indecipherable fluctuations in force magnitude orientation Figure 3.8(b). These fluctuations in the  $F_z$  component may be caused by mechanical and electrical noise within the sensing resolution of the dynamometer; therefore, such unpredictable  $F_z$  values could not be used for further detailed analysis.

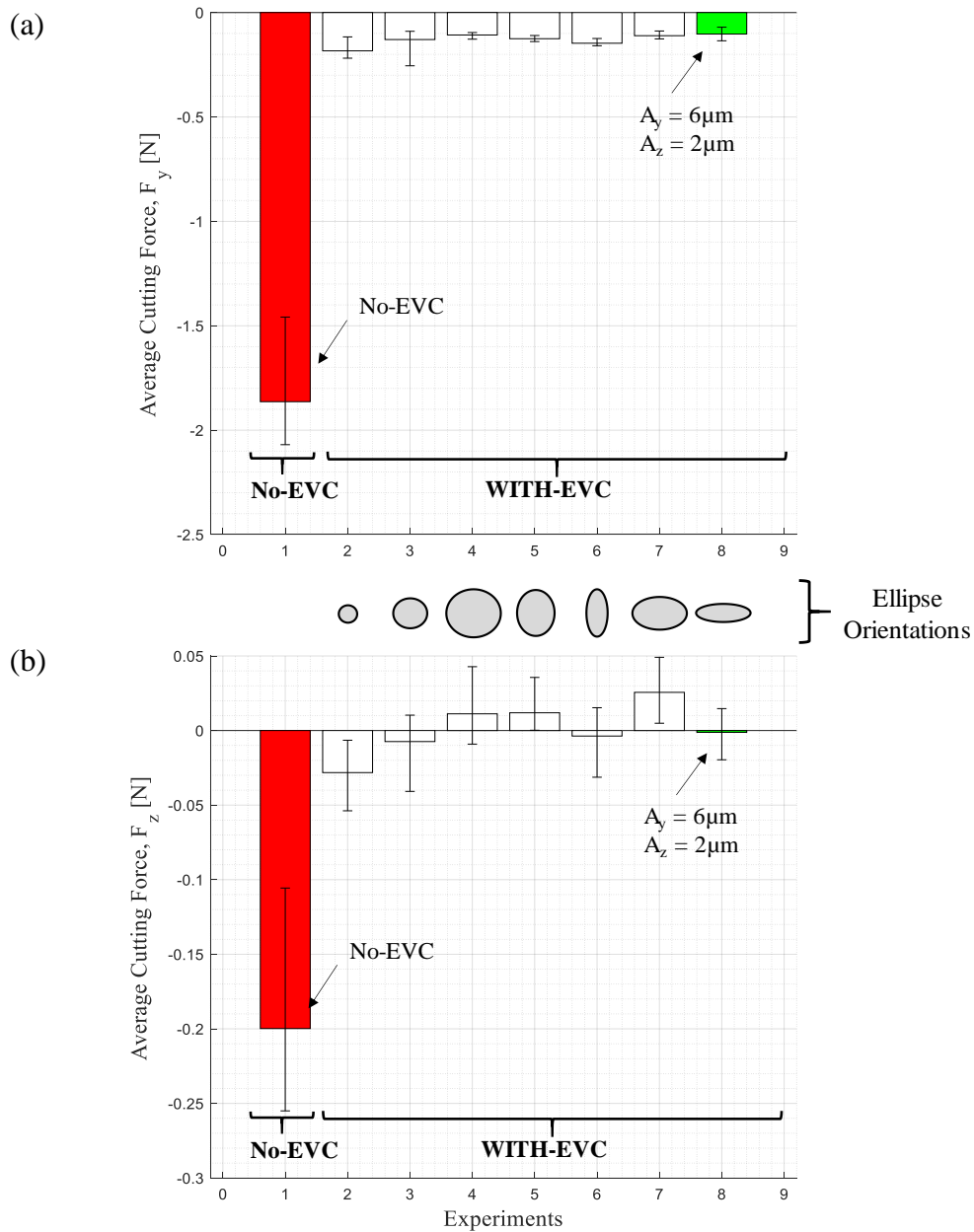


**Figure 3.8:** Average cutting forces for each experiment: (a)  $F_y$  cutting forces, and (b)  $F_z$  thrust forces.

The results for Experiment 1 presented in Figure 3.9 demonstrates the evolution of the cutting forces during the consecutive machining passes. Of note, the first cutting pass, denoted by the average force of  $\sim -2.3$  N, Figure 3.9(c), was not taken into consideration since it was regarded as more of a preliminary alignment/engagement-pass.

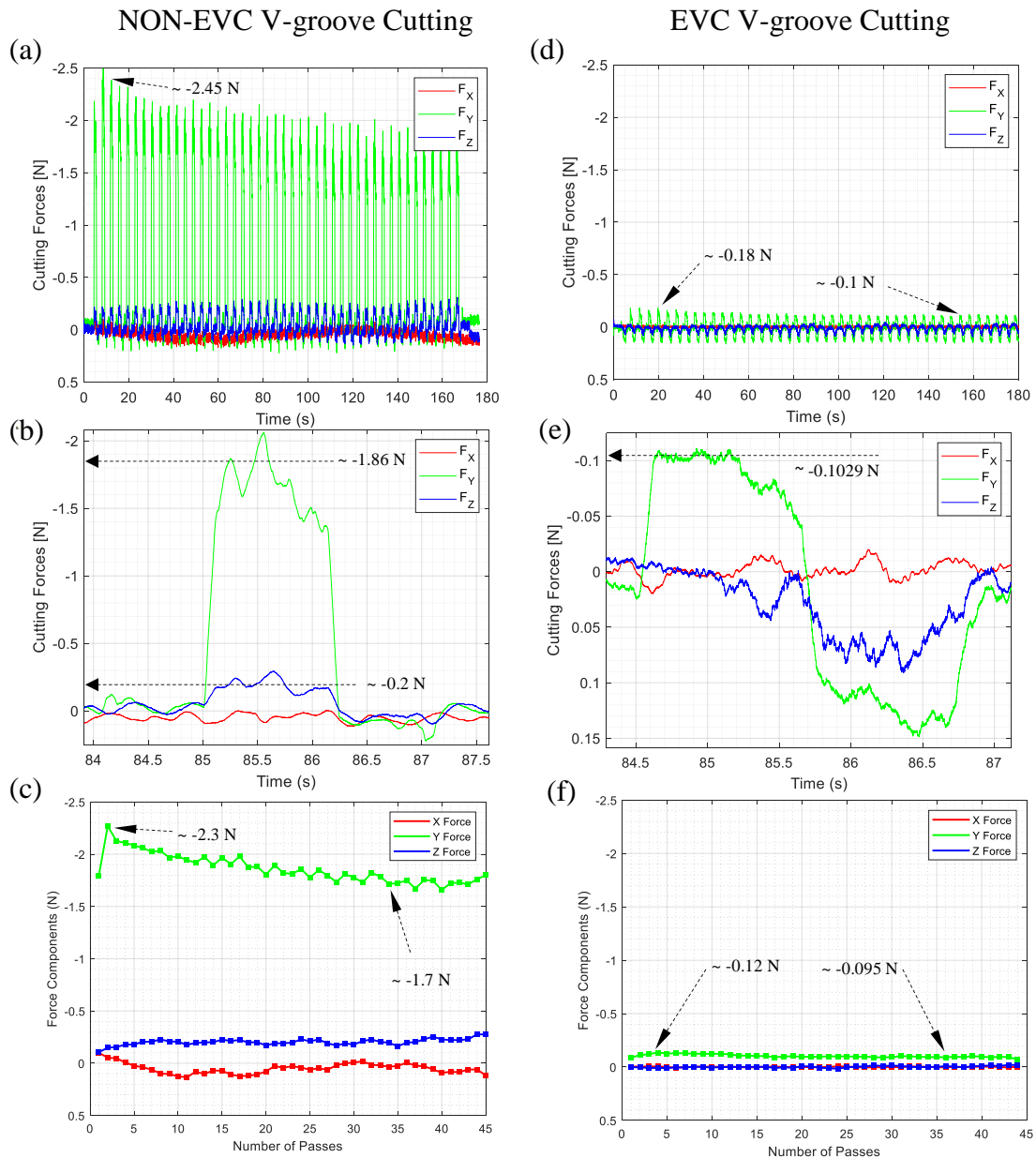


**Figure 3.9:** Evolution of cutting forces during no-EVC vs with-EVC V-groove cutting characterized by  $A_y = 6 \mu\text{m}$  and  $A_z = 2 \mu\text{m}$ : (a and d) multiple successive passes, (b and e) single pass, (c and f) average per machining pass.

One important observation to be made is related to the correlation between the behaviors presented in Figure 3.9. Note that the  $Y$ -forces are produced in the negative orientation—this is characterized by the orientation of dynamometer coordinate system, reiterated in Figure 3.1(a). As suggested by Figure 3.9(a),  $F_{Y,2}$  reaches a maximum magnitude value for the second pass and all subsequent passes exhibit a quasilinear reduction trend:

$$F_{Y,2} < F_{Y,3} < F_{Y,4} < \dots < F_{Y,n}.$$

Here,  $F_{Y,n}$  represents the  $Y$  component of the cutting force for the  $n^{\text{th}}$  cutting pass. Similar notations were used for  $F_{X,n}$  and  $F_{Z,n}$ . This type of downward trend can be directly attributed to the redistribution of the principal cutting force component  $F_{Y,n}$  over the cutting area for each  $n^{\text{th}}$  pass, an activity followed by the gradual reconfiguration of the cutting area from a triangle to a V-shape (Figure 3.1(a)). Because of the deepening groove, cutting force  $F_Y$  gradually changes its location from the tip ( $F_{Y,2}$ ) to the sides of the cutting tool ( $F_{Y,3\dots n}$ ). As a result, the friction between the lateral cutting edges and facets of the V-groove gradually become a more dominating factor on the overall magnitude of  $F_Y$ .

On the other hand, the evolving cutting forces also cause changes in  $F_X$  and  $F_Z$  components. As it can be noticed in Figure 3.9(c),  $F_{Z,2\dots n}$  exhibits a somewhat similar but ascending trend (*i.e.*, opposite to  $F_{Y,2\dots n}$ ). This is a consequence of the fact that side friction forces are projected vertically according to the included angle of the V-groove and therefore they will simultaneously reduce  $F_{Y,2\dots n}$ . However, their influence on  $F_Y$  is relatively minimal. On the other hand, the absent  $X$ -axis motions as well as the symmetrical balancing of the horizontal projections of the lateral friction forces can explain the near-zero/negligible average value of  $F_{X,2\dots n}$ . In other words,  $F_{X,2\dots n}$  and  $F_{Z,2\dots n}$  components remain quite consistently at (very) small values relative to the main  $F_{Y,2\dots n}$  axial component. The value of the lateral components of the cutting force can be assessed as varying around the noise level.

Figure 3.9(b) depicts the quasi-dynamic behavior of the cutting force components during a single cutting pass. During each pass, the cutting tool contacts the workpiece material with the rake face and this causes an initial spike in two of the cutting force components

( $F_Y$  and  $F_Z$ ), but not in the third ( $F_X$ ). The initial contact bends/deflects the tool. This deformation is gradually released during the stable cutting and this in turn might cause the aforementioned linear reduction of  $F_Y$  during the subsequent passes.

A second set of cutting trials was performed with EV motions ‘on’, while preserving all non-EVC cutting parameters, cutting strategy, tool trajectory, and V-groove geometry being cut, as outlined in Table 3.2. As expected, EVC affected the entire cutting mechanics behavior (Figure 3.9(d)) that was then comparatively assessed with respect to its non-EVC counterpart.

In brief, it is quite evident that EVC motions significantly reduce all spatial components of the cutting force. For instance,  $F_Y$  was observed to decrease by a variable range above the 92% threshold (*i.e.*, 92.7% for  $F_{Y,2}$  and 94.4% for  $F_{Y,35}$ ). The overall stability of the cutting has also improved significantly since the 26.1% (0.6 N) reduction of  $F_Y$  that is visible in Figure 3.9(c)—with single-pass deviations around  $\pm 0.36$  N—was replaced with a more stable ‘with’ EVC  $F_Y$  that decreased only slightly from  $F_{Y,2} = -0.12$  N to  $F_{Y,35} = -0.095$  N, deviating from the single-pass average force by  $\pm 0.025$  N. Owing to these small values, it can be noted here that the apparent fluctuations of the  $F_X$  and  $F_Z$  components are in fact comparable to the noise level of the data acquisition system. This notable improvement was also coupled with significant reductions in the friction process between cutting edges and V-groove facets. These observations also demonstrate that cutting force  $F_Y$  becomes proportional to the cutting area since it is characterized only by minor deviations ( $\pm 0.005$  N) from its mean value of approximately  $-0.1$  N that spans over the entire multi-pass cutting process. However, it is perhaps important to mention here that these values may be within the sensing resolution of the dynamometer and also barely above the noise level.

The validity of the results above is reinforced by the observation that forces seen in the no-EVC scenario, both  $F_X$  and  $F_Z$  have in this case negligible values characterized by minor fluctuations caused by mechanical and electrical noise.

Thus,  $F_X \approx 0$  N simply because EVC suppresses (the majority of) process-induced tool-workpiece displacements. Moreover, the following are also plausible: i) the dynamic



compliance of the cutting process becomes almost negligible, ii) cutting force coefficient  $K(\cdot)$  becomes constant for this set of machining parameters, and iii) surface topography is solely determined by the elliptical trajectory of the cutting tool tip.

For all these reasons, EVC constitutes a valuable enabler of micro/nano-structuring of functional surfaces (e.g. [24, 48]). Using a high-precision 3D surface profiler and corresponding 150x Confocal lens, all eight experiments were scanned, leveled and filtered to capture surface patch roughness values. As shown in Figure 3.10, the addition of EVC motions does not decrease surface quality compared to the no-EVC case. This means that in addition to the aforementioned cutting force reduction, EVC does not have a detrimental effect on surface quality. Furthermore, such results were echoed in all eight experiments (Figure 3.8), thus reiterating this processes accuracy and repeatability.

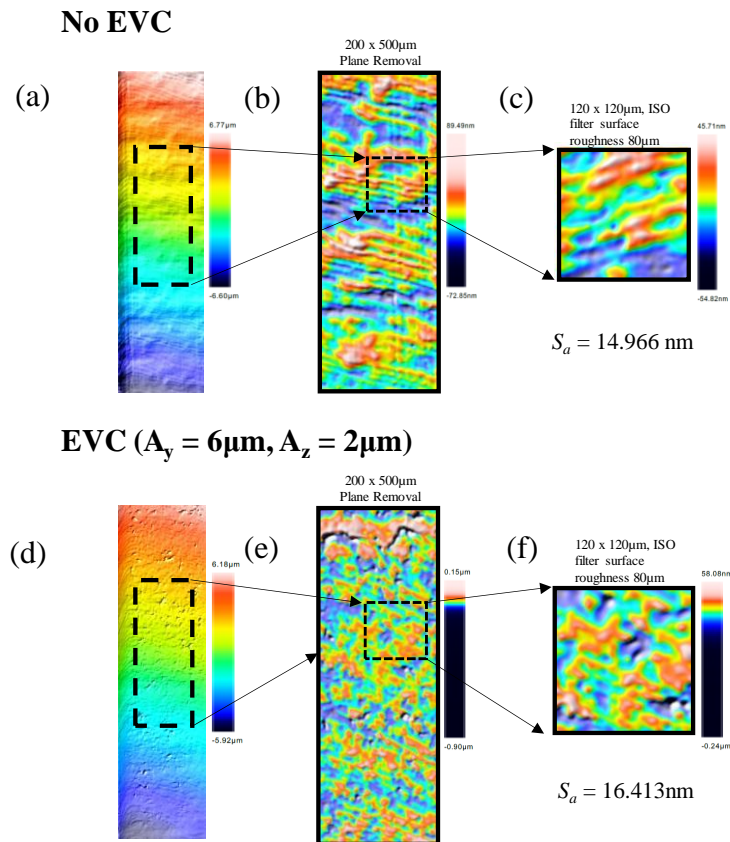


**Figure 3.10:** V-groove surface quality: (a)–(c) Represents no-EVC surface roughness results, (d)–(f) representative with-EVC results surface roughness.

The comparative analysis of the quasi-dynamics during single pass cutting without EVC (Figure 3.9(b)) and with EV (Figure 3.9(e)) suggests both the mechanism and the actual dependence of  $F_Z$  and  $F_X$  on  $F_Y$ . More specifically, Figure 3.9(b) implies that  $F_Z$  represents nothing but a spatial projection (or ‘spatial echo’) of  $F_Y$  that appears concomitantly but at much smaller amplitude ( $F_Y = 1.86$  N vs  $F_Z = -0.2$  N). However, when EVC is on, no such definite relationship exists (Figure 3.9(e)). This could be a supplementary indication of the indirect effect exerted by high-frequency elliptical motions of tool tip (EVC unit is fixed wrt  $Z$ -axis) on low-frequency cutting motions along  $Y$ -axis of the workpiece, *i.e.*, along the principal/axial cutting direction of the  $V$ -groove.

### 3.6 Summary and conclusions

This study was primarily concerned with the investigation of EVC effects on the spatial components of the cutting forces developed during  $V$ -groove micromachining when compared to the traditional SPC process. For this purpose, the spatial decomposition of the cutting forces was initially analyzed by means of classical Merchant’s Circle that was particularized both for with and without EV cutting scenarios. Following these preliminary observations, identical cutting trials were performed under the same two main scenarios and the following conclusions can be drawn:

- The addition of high-frequency elliptical vibrations to single point cutting of  $V$ -grooves significantly changes both its cutting dynamics and chip formation mechanism. The main outcome of the EV-augmented  $V$ -groove cutting is that it leads to significant reductions of cutting force amplitude (> 92%).
- EVC has an important stabilization effect on cutting forces since they become less dependent on the friction between tool and  $V$ -groove facets. This effect is implied by the lack of descending trend in  $F_Y$  (0.6 N to 0.025 N) during multi-pass machining of  $V$ -grooves.
- Elliptical vibrations change the dynamics of the cutting process since the tip moves at high speeds with respect to the slow-moving workpiece. This observation is supported by the fact that when EVC is on,  $F_Z$  and  $F_X$  components have a minimal effect on  $F_Y$ .

In summary, it is seen that cutting forces consistently and significantly decrease following the introduction of elliptical vibration cutting, and it is anticipated that these improvements of the V-groove cutting process brought by EVC will open up new opportunities in micromachining of micro/nano products, systems, sensors, functional surfaces, as well as lighting/holographic optics. Furthermore, the results above could constitute the premise of several new scientific directions related to deep learning-based analysis, optimization and control of the cutting-based material removal at micro/nano-scale and/or with optical surface quality.

## Chapter 4

### Parametric Analysis of EVASPC Characteristics and their Effect on Process Performance

**Farrus, N.,** Milliken, N., Tutunea-Fatan, O.R., & Bordatchev, E. V. (2020). Parametric Analysis of EVASPC Characteristics and their Effect on Process Performance. Submitted in Aug. 2020 to *The International Journal of Advanced Manufacturing Technology*.

## **4 Parametric Analysis of EVASPC Characteristics and their Effect on Process Performance**

### **4.1 Overview**

In the previous chapter, the fabrication of constant area V-grooves was used to demonstrate the capabilities offered by EVASPC such that cutting force reduction and stabilization was observed. This being said, while EVASPC was shown to enhance cutting force performance for V-groove fabrication, the next step aims to understand the influence that certain EVASPC process parameters have on both cutting forces and surface quality.

Thus, the parametric study presented in the following chapter utilizes orthogonal single point cutting integrated with elliptical vibrations to isolate a pair of linked cutting parameters—EV horizontal and vertical amplitudes—with the purpose of analyzing the influence that their relationship has on the cutting forces and surface quality results. Furthermore, the determination of a so-called functional dependence model is achieved, defining the transition from a machining process that prioritizes cutting force reduction to one that prioritizes surface quality improvement. Subsequent, a finite element model will aim to reproduce experimental cutting force results as a method of predictive modeling.

### **4.2 Background**

There are two primary motivations behind implementing EVASPC: (1) a surface quality enhanced cutting process that aims to generate micro or even nano-scale structures for surface functionality purposes, and (2) a cutting force efficient process that aims to reduce cutting forces in the two primary component directions (cutting direction and thrust direction). In the following chapter, a parametric study is completed to determine the influence that manipulating elliptical vibration (EV) amplitudes have on primary process outcomes—cutting force generation and surface quality. This was achieved through the use of orthogonal EVASPC in order to obtain clear and concise results.

Orthogonal cutting has been exhaustively used for conventional machining, and can be considered a fundamental single point cutting method. Although it has demonstrated

extensive applicability for nearly a century now, ultra-precise orthogonal cutting, in the form of EVC, has recently flourished. It has been the choice of many researchers when it comes to the force analysis of enhanced high-accuracy cutting processes and cutting mechanics—both, through experiment and simulation. In addition, orthogonal cutting was used to determine the origins of EVC's cutting force reduction on the primary cutting face of the tool; hence, the friction-reversal zone as demonstrated by Ma *et al.* and then again by Zhang *et al.* [27] and [28], respectively. Furthermore, orthogonal cutting for ultrasonic applications has been used for the analysis of chip formation and its contribution to the EV transient force reduction [60].

In addition to cutting force reduction, orthogonal EVC has also been used to generate functional surface micro/nano-structures through EV amplitude control. Many studies have focused on the applicability of such amplitude control for the purpose of surface structuring—creating surface textures based on sinusoidal, ramp, or zig-zag tool paths to obtain the desired surface functionality [16]. Ultimately, recent applications of amplitude control consist of micro-channeling [39], surface wettability [17], micro-dimpling [21], and paint-free surface colouration [24]. Secondary EVC-based amplitude control studies have also been used to predict cutter-compensation and other predictive methods that prevent unwanted tool engagement; thus, improving process accuracy and surface functionality [34].

All this being said, although studies have demonstrated the influence that elliptical vibrations have on orthogonal cutting and various other high-accuracy fabrication processes, there has been no explicit parametric study focused on EV amplitudes and the influence they have on cutting forces and surface quality (to the best of the authors knowledge). Hence, the purpose of this chapter is to execute a parametric study that breaks down the ultrasonic elliptical vibration assisted orthogonal single point diamond cutting process into its most fundamental components in order to analyze the effect that two specific cutting parameters—horizontal ( $A_y$ ) and vertical amplitudes ( $A_z$ )—have on force generation and surface roughness, both experimentally and through simulation, along with the functional dependence between these two outputs, Figure 4.1.

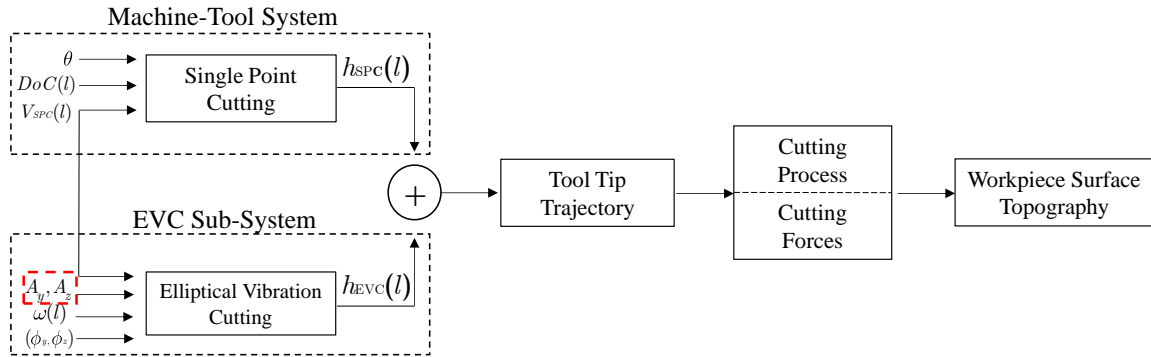


**Figure 4.1:** EVASPC process flow diagram.

In order to do so, sixteen aluminum ribbed structures were fabricated using a monocrystalline diamond tool insert: fifteen were assisted by orthogonal EVASPC, and the other without EV assistance. A significant number of cutting parameters remained constant, while the only variability came from the modification of the EV horizontal and vertical amplitudes that define the ellipse size and shape. In this regard, the ultimate objective of this study is to demonstrate the influence that EVC parameters have on the cutting forces and the surface roughness through the context of orthogonal SPC. Furthermore, this study will demonstrate a functional dependence model that characterizes where cutting process conditions transition from a cutting-force-efficient process to surface-quality-enhanced process, based on the size and shape of the ellipse. To conclude, a supportive finite element method (FEM) model will mimic experimental cutting conditions and provide a method of predictive modeling.

### 4.3 Parametric study of experiments

The elliptical vibration parameters lay the foundation of this study, specifically of concern are the 2D elliptical vibration amplitudes that alone provide extensive flexibility and capabilities for EVC. Through the methodological and experimental setup, trial results will develop a reliable metric that describes the EVASPC transition from a cutting force reduced process to a surface quality dominant process, Figure 4.2.

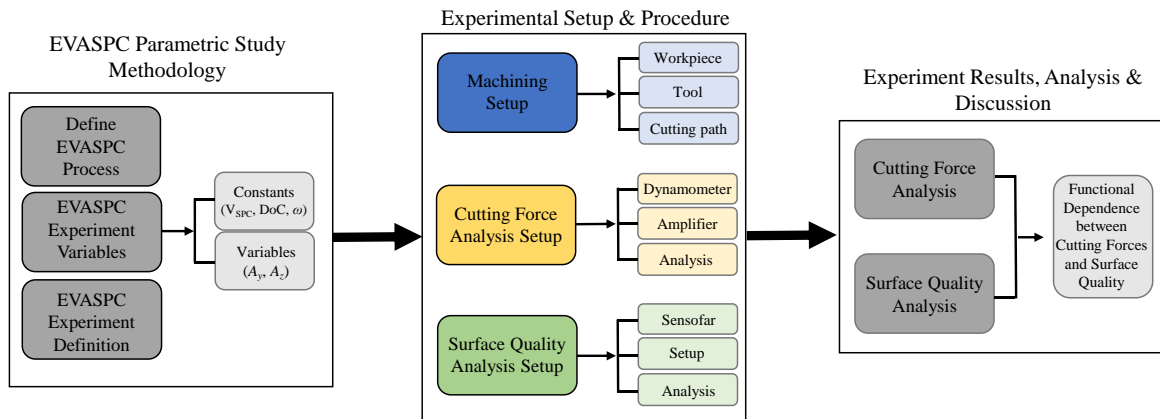


**Figure 4.2:** Step-by-step EVASPC study methodology.

The cutting-efficient process can be defined by its prioritization of cutting force reduction over other process outcomes, where the user requires reduced force components in the cutting direction and/or the thrust direction. This method can be used for improving cutting time, reducing tool wear, and preventing diamond tool graphitization induced by ferrous workpiece material. On the other hand, a surface quality enhanced process prioritizes surface finish in one of two ways: the first is through minimized surface roughness,  $S_a$ , and the second is through high-accuracy surface structure formation. This method is advantageous for surface functionality applications.

The size, shape, and orientation of EV amplitudes are hypothesized to determine which process is achieved. Furthermore, the combined horizontal ( $A_y$ ) and vertical ( $A_z$ ) amplitudes define the orientation of the tool trajectory as it travels across the workpiece (Figure 4.1). The combined  $A_y$  and  $A_z$  form an elliptical locus that comes in one of three geometrical classes, Figure 4.3: (a) vertical-dominant EV amplitudes where the  $A_z$  is greater than the  $A_y$ , (b) circular orientation where the  $A_y$  and  $A_z$  amplitudes are equal, and (c) horizontal-dominant EV amplitudes where the  $A_y$  is greater than  $A_z$ .



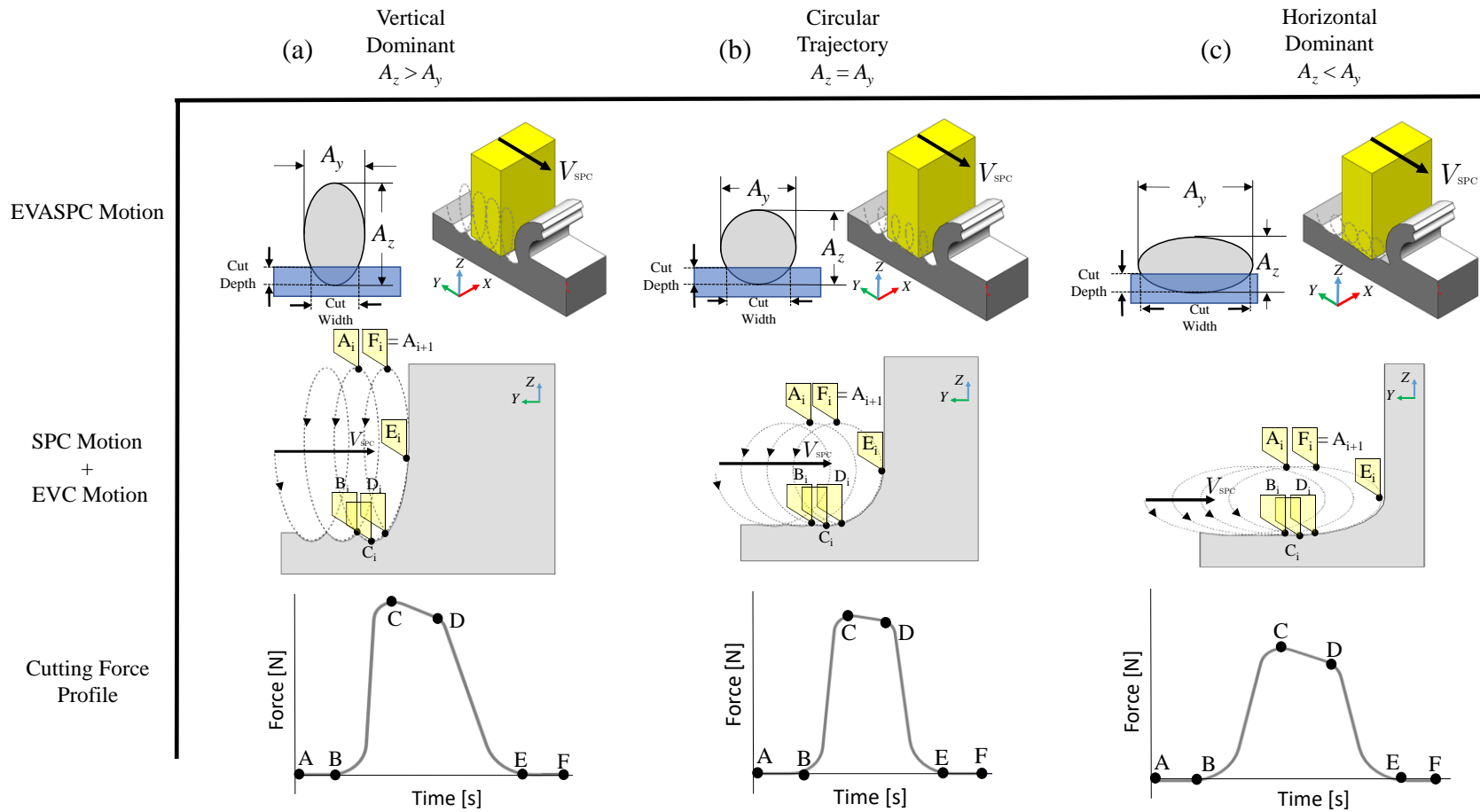


**Figure 4.3:** Elliptical vibration amplitude orientations, tool trajectory and cutting force profile: (a) Vertical-dominant ellipse orientation, (b) circular ellipse orientation, and (c) horizontal-dominant ellipse orientation.

These classifications are the key principles for the following chapter. Previous literature has demonstrated the impact that specific orientations of the ellipse has on desired characteristic outcomes; however, to the best of my knowledge, there has been no study covering the overarching influence that EV amplitude size and orientation has on cutting forces and surface quality. Therefore, this chapter will establish the parametric relationship between ellipse orientation and the key EVASPC process outcomes (cutting forces and surface quality).

Vertical-dominant elliptical orientation has been touted to provide functional micro/nano surface structure capabilities. As seen in Figure 4.3(a), they produce more pronounced surface cusps that, when linked with a desired cutting speed, have applicability in surface colouration, surface wettability, and various other functions [61].

On the contrary, horizontal-dominant elliptical orientation is synonymous with providing reduced surface roughness (within the optical surface quality range). In the past, EVC itself has demonstrated optical quality surface finish according to industry standards, however the predominant horizontal orientation can enhance such effects even further [15]. The mirror-like surface qualities of horizontal-dominant EVC come from the relatively shallow surface cusps produced, Figure 4.3(c), resulting in virtually seamless surface generation similar to traditional CC methods, but without CC's detrimental flaws—graphitization, tool wear, surface quality degradation, etc.

The circular elliptical orientation, Figure 4.3(b), has been hypothesized to provide a stable cutting approach that offers smooth motion kinematics throughout a single elliptical revolution, all the while, creating a balanced force profile between normal and thrust force components.

The combination of SPC, Equation 2.1, and EVC, Equation 2.2, results in the elliptical tool trajectory motion defined as EVASPC, Equation 2.3, and visualized in Figure 4.3. Ultimately, producing unique cutting force profiles and surface topographies based on the ellipse orientation. Furthermore, the mean force reduction produced through EVASPC comes directly from the tool trajectory, and more specifically, from the disengagement

period between the tool and workpiece. Traditionally, in conventional SPC, the tool is in contact with the workpiece throughout the cutting process, resulting in a constant mean force. However, in EVASPC, the pulsating contact (or periodic disengagement) between tool and workpiece produces a time period over which 0 N of cutting force is achieved; therefore, decreasing the mean forces over the cutting process. This mean force reduction can be significantly influenced by ellipse size and orientation.

The general characteristics of the preceding elliptical orientations lay the foundation for the following sixteen experiments—fifteen experiments with orthogonal EVASPC, and one experiment using conventional no-EVC orthogonal cutting—Table 4.1. The premise around this study is to utilize the elliptical vibration amplitude range offered by the external EVC unit—EL-50 $\Sigma$  Control Unit—to create fifteen different ellipse orientations, spanning all three scenarios visible in Figure 4.3. The EL-50 $\Sigma$  EV Control Unit used in this study created elliptical dimensions ranging from 2  $\mu\text{m}$  to 6  $\mu\text{m}$  (for both  $A_y$  and  $A_z$ ). The addition of the EV amplitudes induces a change in the overall  $DoC_{total}$ , depending on the  $A_z$  used. As seen in Figure 4.4, without EVC, the depth-of-cut remains static at the nominal  $DoC_{cc}$ , however, when EVC is introduced, there is a transient depth-of-cut introduced as a result of the elliptical motion. This transient motion adds an additional depth-of-cut component,  $DoC_{EVC}$ , that is defined by the vertical amplitude ( $A_z$ ). Consequently, I acknowledged this additional process consideration in the experimental setup. All this being said, the sixteenth, and final, experiment was done in the absence of EVC to demonstrate conventional SPC, and was used as a benchmark for result analysis. Ultimately, Table 4.1 demonstrates the sixteen unique experiments, where the EV amplitudes are the only cutting parameters varied in order to analyze their effect on the cutting force generation and surface quality of the workpiece.

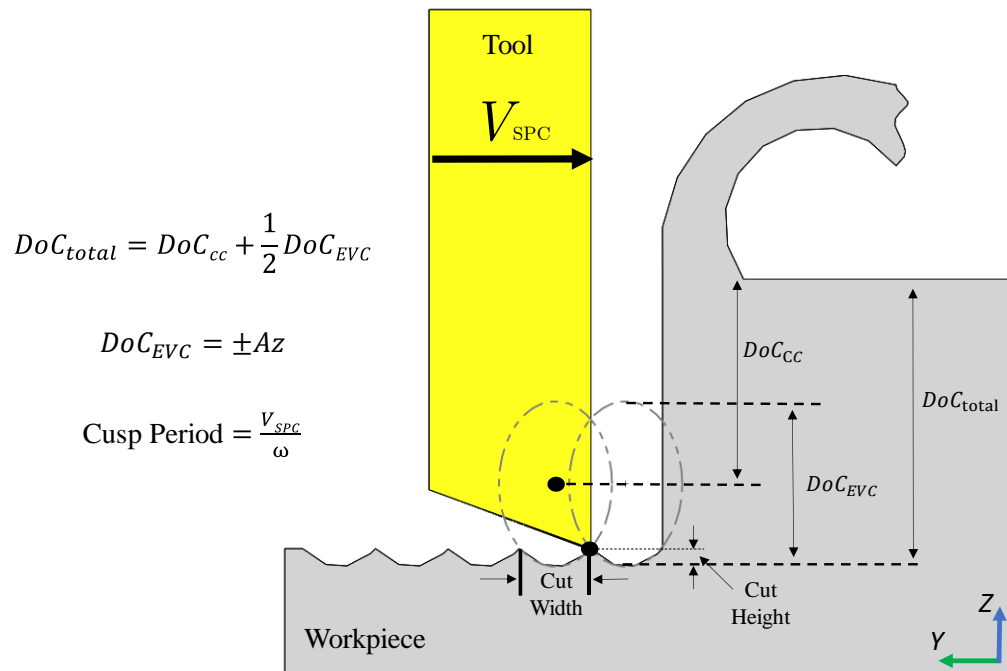

















**Figure 4.4:** EV amplitude influence on depth-of-cut.

The remainder of the cutting parameters were held constant across all sixteen experiments, namely the cutting speed ( $V_{SPC}$ ), the nominal depth-of-cut ( $DoC_{cc}$ ), and the vibrational frequency ( $\omega$ ). Note, the vibrational frequency is indeed one of the unique driving input parameters for EVASPC, however, the EL-50Σ EV Control unit used for the experiment provided only one allowable vibrational frequency at 41 kHz, thus,  $\omega$  remained constant.

While the EL-50Σ EV control unit has greater EV amplitude capabilities than just those listed in Table 4.1, I believed that the chosen experiments provide a sufficient picture of the cutting force and surface quality trends for orthogonal EVASPC, without excessively stressing the multi-axis machine and monocrystalline tool—which could possibly result in damaged equipment and/or inaccurate results.

**Table 4.1:** Matrix of experimental EV amplitudes along with fixed cutting parameters.

Constant Cutting Parameters ( $V_{SPC}$ , DoC, $\omega$ )		Horizontal Amplitude, $A_y$ ( $\mu\text{m}$ )			
		0	2	4	6
Vertical Amplitude, $A_z$ ( $\mu\text{m}$ )	0	Exp. 16	X	X	X
	2	X	Exp.1 	Exp.2 	Exp.3 
	3	X	Exp.4 	Exp.5 	Exp.6 
	4	X	Exp.7 	Exp.8 	Exp.9 
	5	X	Exp.10 	Exp.11 	Exp.12 
	6	X	Exp.13 	Exp.14 	Exp.15 

The supplementary characteristic of this study—behind EV assisted single point cutting—is the utilization of planar orthogonal cutting. Elliptical vibrations present an extra level of complexity to the cutting process through the introduction of additional cutting parameters and unique EV cutting motion kinematics that can create unpredictable obscurities in experimental results. Orthogonal-based EVASPC limits these complexities dramatically, and is defined by the use of a single cutting edge, such that the adjacent cutting face is oriented orthogonally with respect to the cutting motion (Figure 4.3). This produces chips that travel in the direction parallel to the feed direction [11]. Consequently, the force components remain in two primary directions: the cutting direction (parallel to  $V_{SPC}$ ) as well as the direction perpendicular to the cutting direction (the thrust direction) [12]. This method of plane cutting pairs nicely with this parametric study of EVASPC and reduces the number of cutting force components required for analysis; contrary to the previous chapter, where cutting forces were present in three directions: the cutting direction, thrust direction, and on the side-faces of the triangular tool.

## 4.4 Experimental procedure

In order to measure, record and analyze the actual cutting forces and surface roughness over time and space domains, an array of orthogonal SPC experiments with integrated EVC motions were used (Figure 4.5). The experimental setup was based on a high-performance/high-precision multi-process 5-axis micromachining center MicroGantry nano5x manufactured by Kugler GmbH. The external EVC unit EL-50Σ, manufactured by TAGA Electric Co., Ltd. was mounted vertically on the Z-axis. Horizontal and vertical vibrations were fully controlled by means of an electrical controller and power amplifiers, and transferred to the cutting tool tip.

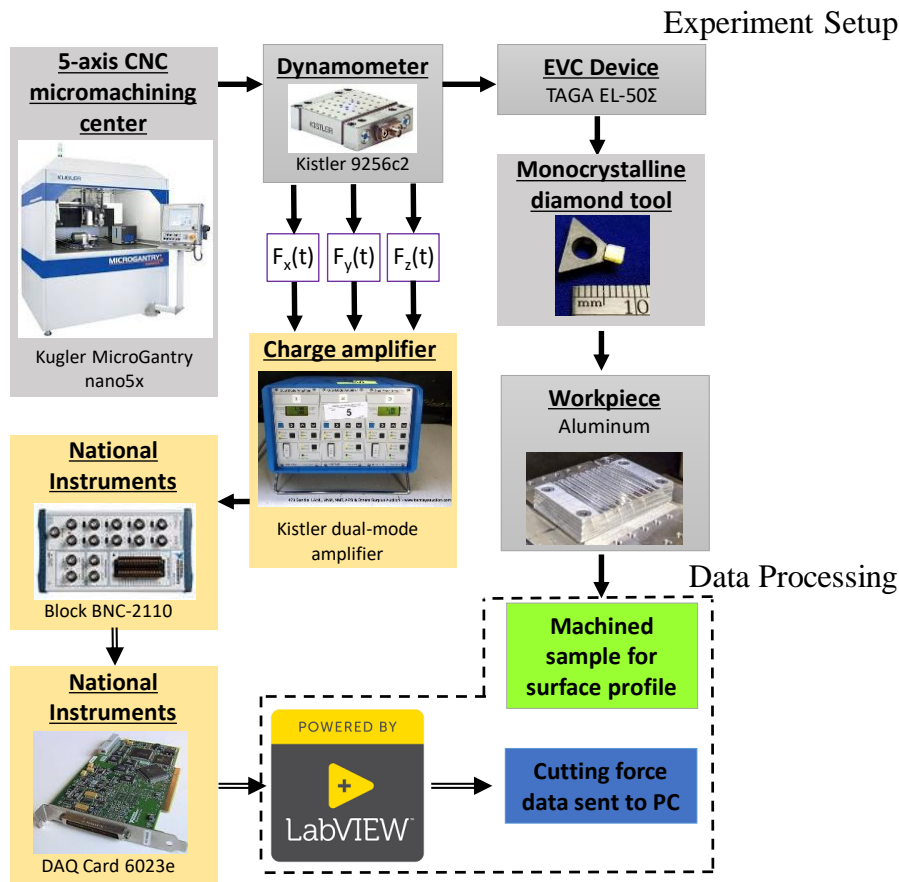


**Figure 4.5:** Experimental setup and data processing workflow.

The tool used in this study was a rectangular-shaped monocrystalline single point diamond cutting tool with cutting face width of 3.2 mm, rake angle of  $0^\circ$  and a clearance angle of  $5^\circ$  (Figure 4.6(a)). Special attention was dedicated to the clearance angle since it

introduced a limitation in the selection of the EVC parameters (e.g. vertical and horizontal amplitudes), as well as limits to the magnitude of the cutting speed, in order to avoid frictional contact between the clearance face of the tool and the previously cut surface. This undesired interference was avoided through the choice of EV parameters listed in Table 4.1.

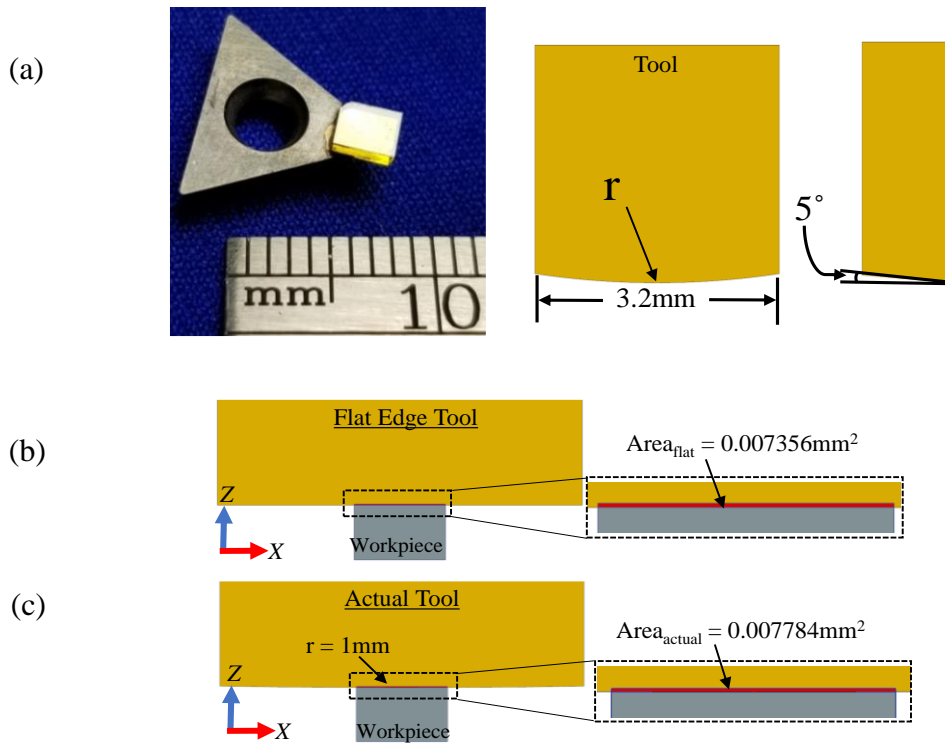


**Figure 4.6:** Orthogonal monocrystalline single point diamond cutting tool: (a) Geometrical tool dimensions, (b) ideal flat tool cutting area, and (c) actual tool cutting area used for experiment.

Additionally, it is worth noting that the tool contained a very large, and relatively negligible, cutting edge radius denoted by  $r$  in Figure 4.6(a) (exaggerated for demonstration only). Although this radius was present, it was very large relative to the overall tool geometry and its influence on the contact area between the tool and workpiece was negligible—as seen through the miniscule difference in contact area for an ideal flat edge tool (Figure 4.6(b)) and the real experimental tool with 1 mm cutting edge radius (Figure 4.6(c)). Consequently, the cutting force and surface quality results

produced through experiments can comfortably be assumed to be the result of ideal flat-edge orthogonal cutting.

Similar to the previous chapter, the workpiece, made of aluminum alloy 6061, was mounted onto the center of a Kistler 9256C-2 multicomponent dynamometer, which was subsequently attached to a tilt-swivel unit of the 5-axis micromachining center, allowing 4-axis motions of the workpiece. The ribbed workpiece was oriented on the dynamometer such that the cutting direction remained in the  $Y$ -axis and the thrust component in the  $Z$ -axis, Figure 4.7.

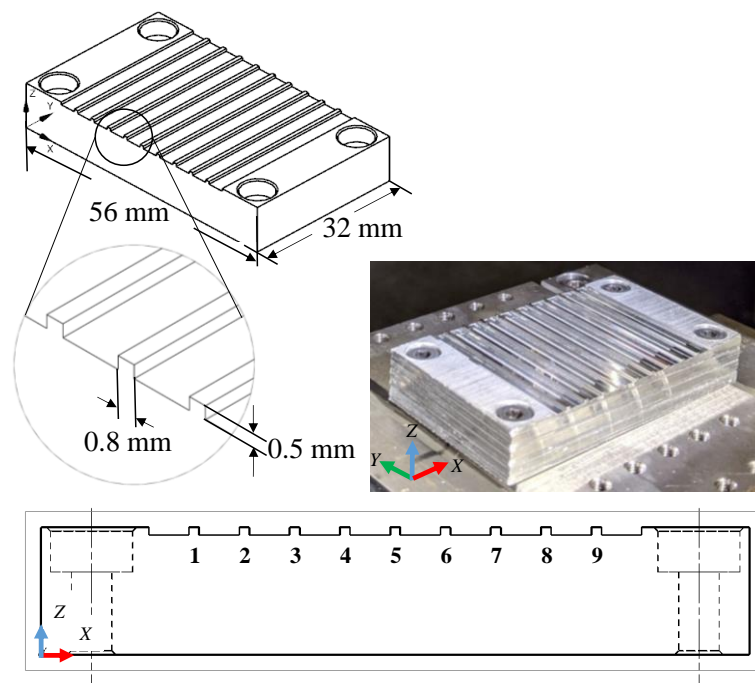


**Figure 4.7:** Multi-ribbed Aluminum T-6061 workpiece used for experiment.

In order to complete the sixteen experiments, two prefabricated workpieces were machined to the specific dimensions seen in Figure 4.7. Each workpiece consisted of 9 ribbed structures measuring 0.5 mm tall, 0.8 mm wide and 32 mm long. The rib width was designed to be smaller than the tool width (3.2 mm), such that the only contact made between the tool and workpiece was on the primary cutting face. Additionally, the rib length was chosen to allow for sufficient steady-state cutting conditions which could be reflected in the cutting forces results and surface finish. Such conditions are achieved



when the tool has accelerated to the desired constant cutting speed and all other cutting parameters remain constant.

Subsequently, the tool and workpiece were placed onto the multi-axis Kugler GmbH CNC machine and aligned with respect to one another, Figure 4.8. The tool was aligned to ensure perpendicularity with the workpiece, such that the cutting area remained constant. Additionally, the workpiece was mounted on the Kistler dynamometer and aligned in the  $X$ ,  $Y$ , and  $Z$  axis.

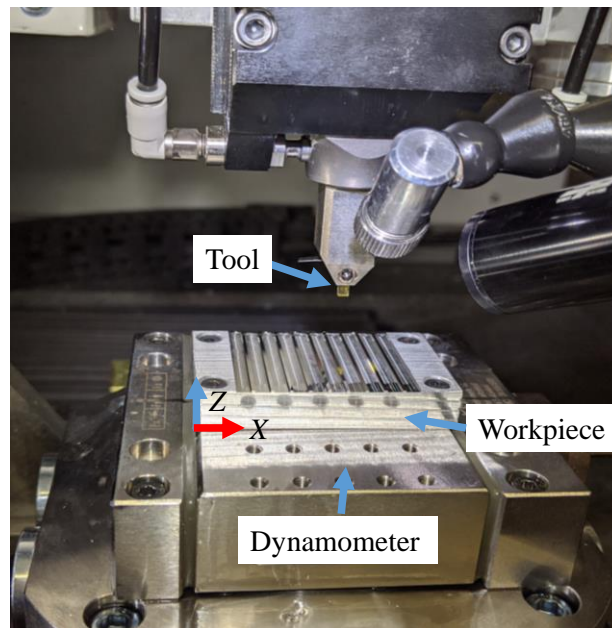


**Figure 4.8:** Experimental setup.

The cutting path utilized in this work consisted of an axially-translating diamond tool that plunged into the workpiece material over a number of consecutive passes while maintaining constant cutting parameters. An overview of the cutting kinematics of this strategy is shown in Figure 4.9. Rib fabrication consisted of four cutting passes that ran across the workpiece. The first three passes acted as preparation passes and also verified the  $Z$ -axis alignment between tool and workpiece. In each of these passes, the tool plunged in the  $-Z$  direction  $50\ \mu\text{m}$  at point A and, in the absence of EV assistance, moved across the workpiece in the  $-Y$  direction at a constant cutting speed and DoC to point B. These passes were used to remove any peak-to-peak waviness present on the initially rough surface, Figure 4.9(a), and to create an ultra-finished planar surface, such that the

detrimental  $DoC_{total} = 10 \mu\text{m}$  was machined. After the third pass, the tool lifted above the workpiece at B and returned to its starting position at A, readying itself for the final pass (the experimental pass).

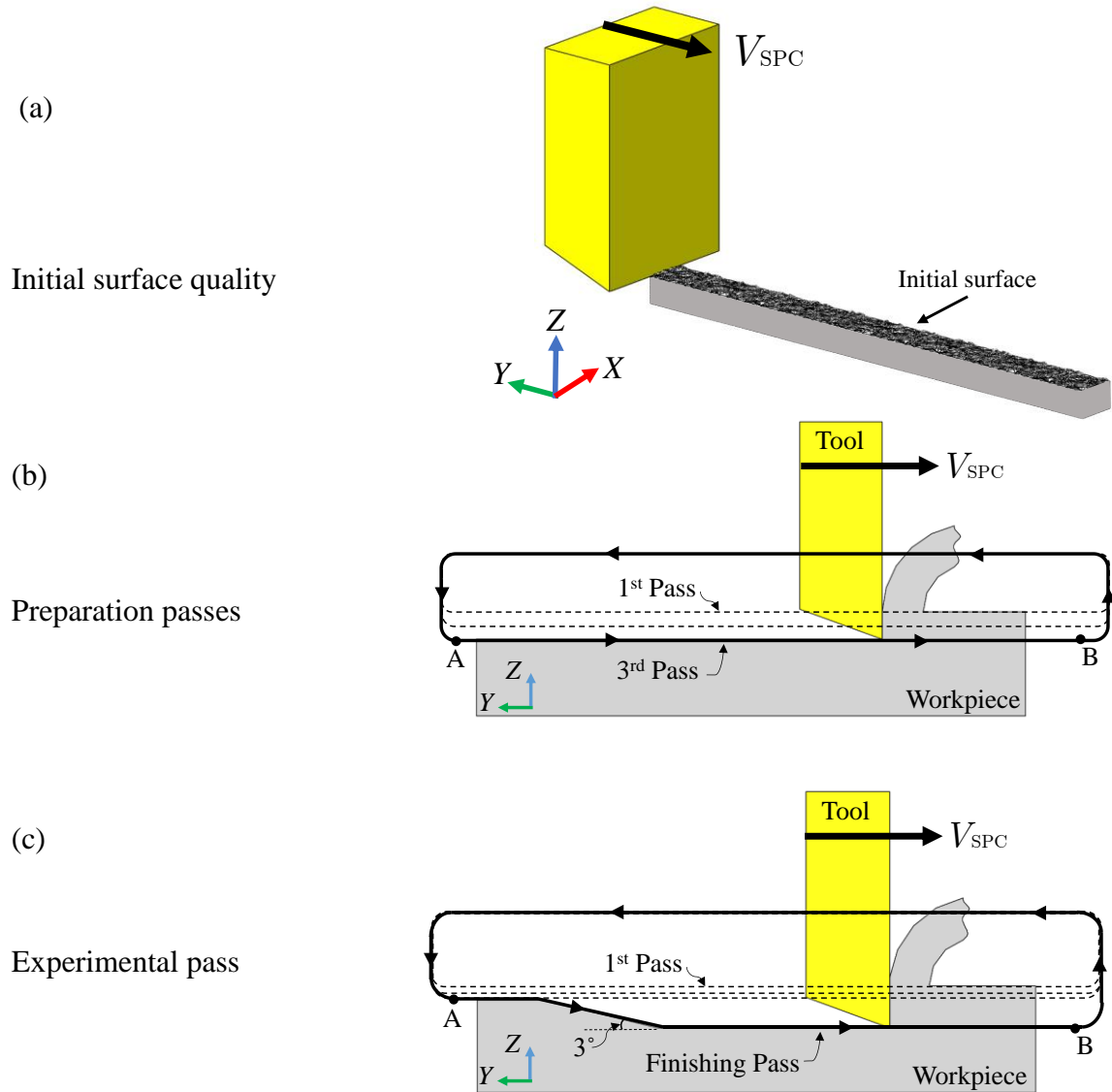


**Figure 4.9:** Cutting kinematics of rib fabrication via orthogonal EVASPC: (a) Initial workpiece surface, (b) three consecutive preparation passes, and (c) final experimental pass.

The final pass introduced the unique EV parameters and followed a slightly modified cutting path. The tool engaged with the workpiece at an angle of  $3^\circ$  until the desired DoC was reached. This engagement method was implemented in order to minimize large impact pressure between the tool and workpiece, allowing the process to reach

steady-state cutting conditions, avoiding large spikes in cutting force results and prolonging tool life. As the name of the cutting strategy implies, the EV amplitudes were the only variables in each of the fifteen EVASPC experiments, while all other cutting parameters remained constant.

The EV amplitude specifications have been detailed, however, the fixed cutting parameters were also explicitly chosen to deliver clear and concise experimental results. Of note are the cutting speed ( $V_{SPC}$ ) and the depth-of-cut (DoC), Table 4.2. The cutting speed of 1200 mm/min was chosen to allow for the analysis of EVASPC-induced surface cusps—as will be mentioned shortly, the cusp periodicity must lay within the resolution range of the surface measurement instrument.

**Table 4.2:** Cutting trial parameters.

<b>Parameter</b>	<b>Value</b>
Cutting speed, $V_{SPC}$ (mm/min)	1200
Depth-of-Cut, DoC ( $\mu\text{m}$ )	10
Vibrational frequency, $\omega$ (kHz)	41
Horizontal amplitude, $A_y$ ( $\mu\text{m}$ )	<b>Variable</b>
Vertical Amplitude, $A_z$ ( $\mu\text{m}$ )	<b>Variable</b>
Cut length (mm)	32
Tool engagement angle ( $^\circ$ )	3
Tool Cutting Face Width (mm)	3.2
Tool Clearance Angle ( $^\circ$ )	5
Rake angle ( $^\circ$ )	0
Tool Material	Monocrystalline Diamond
Workpiece material	Aluminum alloy 6061
Coolant	Isoparaffin mist

On the other hand, the depth-of-cut ( $DoC_{total}$ ) of 10  $\mu\text{m}$  was chosen based on previous experience, as it provided a balance between enhanced cutting force results and limitations in tool wear. The DoC for EVASPC process analysis must be sufficient enough to produce cutting forces that are readable by the dynamometer (limiting noisy signals from miscellaneous sources such as apparatus vibrations), yet small enough to limit tool wear. As will be seen in sections to come, cutting parameter definition is absolutely critical when analyzing micro-scale cutting processes.

#### 4.4.1 *Cutting force measurement and analysis procedure*

For the finishing pass of each experiment, Figure 4.9(c), spatial cutting force components  $\{F_x(t), F_y(t), F_z(t)\}$  were measured by the mounted dynamometer and then converted into corresponding electrical signals by three Kistler 5010 dual mode charge amplifiers (one amplifier per cutting force component). As alluded to, the primary cutting force components for orthogonal EVASPC are produced in the cutting direction and the thrust direction; therefore, the dynamometer was situated such that these components translate into dynamometer  $Y$  and  $Z$  axes, respectively, Figure 4.8. From here, the electrical signals were digitized by a National Instruments 6023e data acquisition card with a sampling frequency of 2 kHz, and the raw data was saved onto a computer using LabVIEW for further data processing.

The time-dependent cutting force components  $\{F_x(t), F_y(t), F_z(t)\}$  were then filtered by means of a MATLAB software and in-house developed post-processing script. To investigate the quasi-static components of the cutting forces, a MATLAB-based moving-average low-pass filter was used to filter/smooth the acquired data. This filter used a window size of 200 data points and a sampling frequency of 2 kHz (matching the sampling rate of the experimental DAQ system). Furthermore, the linear drift introduced by the charge amplifier was eliminated from the data for each of the cutting force components. Finally, the digital signature of the cutting force components was separated with respect to individual tool motions and then average cutting forces were calculated, Figure 4.10.

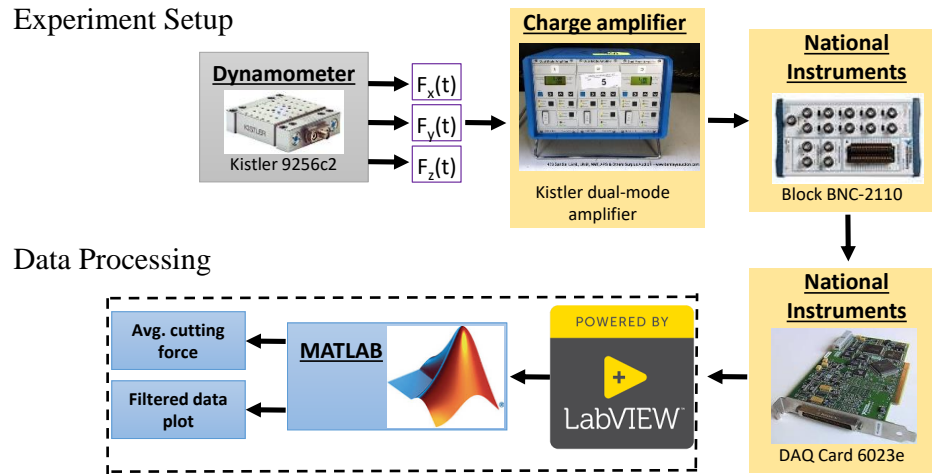


**Figure 4.10:** Cutting force measurement and analysis procedure.

Ideally, force data for each elliptical revolution would be desired, however the frequency of EV motion far-exceeds the sampling rate capabilities of existing data acquisition instruments. Thus, for the final pass of each experiment, the average force components gathered from MATLAB were used as the primary sources of data for comparative analysis, and will demonstrate the mean cutting force reduction provided through EV assisted cutting.

#### 4.4.2 *Surface topography measurement and analysis procedure*

The surface topography of each fabricated rib also underwent post-processing analysis with the assistance of a SensoFar high-performance 3D optical profiler. The fabricated workpiece was placed on the work-table, aligned such that the lens could travel the length of the rib, and focused according to the two magnification settings used for analysis: (1) 10× DI Interferometry lens, and (2) 150× EPI Confocal lens. SensoFar’s integrated visual software, SensoScan, was used to view the magnified workpiece on a PC, incorporating any additional data analysis operators, and ensuring alignment (leveling, filtering, form removal, and cropping).

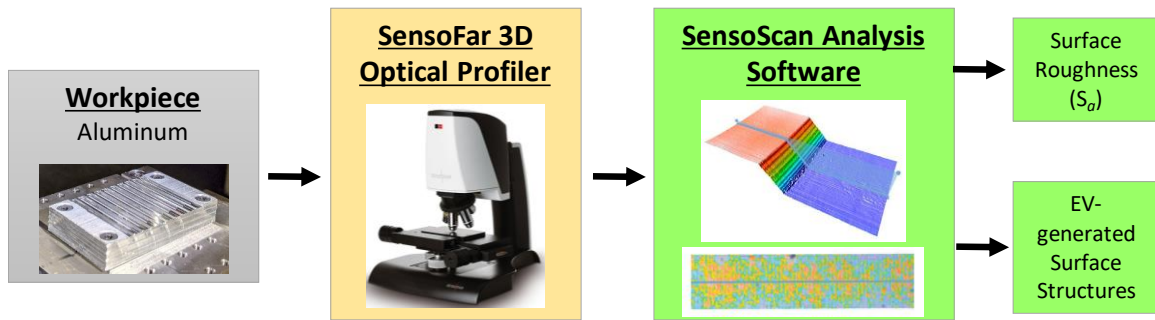


**Figure 4.11:** Surface profile measurement and analysis procedure.

The 10× DI Interferometry lens was used to extract a full scan of each fabricated rib in order to verify and compare actual results to the desired process parameters in Table 4.2. This lens was also used for the rib surface roughness analysis, calculating an average  $S_a$  value across the cutting length. Additionally, the Interferometry VSI profiler option used vertical white-light scans to measure the smooth surfaces and view critical dimension measurements. On the other hand, the 150× EPI Confocal lens was used for a more detailed analysis of EVASPC-induced surface structures, and the verification of experimental cutting speed and vibrational frequency—described through the surface cusp width. The Confocal profiler was used to enhance large scans and view critical dimension measurements—produced as a result of each unique ellipse orientation.

## 4.5 Cutting force results

The first process outcome analyzed in this study establishes the influence that elliptical vibration amplitude has on the mean cutting forces. Several orthogonal cutting trials were performed on the aluminum workpiece, with and without EVASPC, in order to compare the actual cutting forces produced as a result of each unique ellipse orientation. Following the machining setup and preparation passes, the final cutting pass was executed, from which the cutting forces were captured by the Kistler dynamometer, amplified and then filtered through MATLAB for further analysis. This section analyzes the average cutting forces generated for each experiment, drawing attention to the influence that specific ellipse orientations have on the force magnitudes.

First and foremost, a detailed analysis compared two specific experiments: the first being the conventional SPC experiment without EV assistance, and the second being the

EVASPC experiment characterized by EV amplitudes  $A_y = 2\mu\text{m}$  and  $A_z = 2\mu\text{m}$ . One important observation is related to the correlation between the behavior of the SPC and the EVASPC results presented in Figure 4.12(a). Note that the  $Y$ -forces are produced in the negative orientation—this is characterized by the orientation of dynamometer coordinate system.

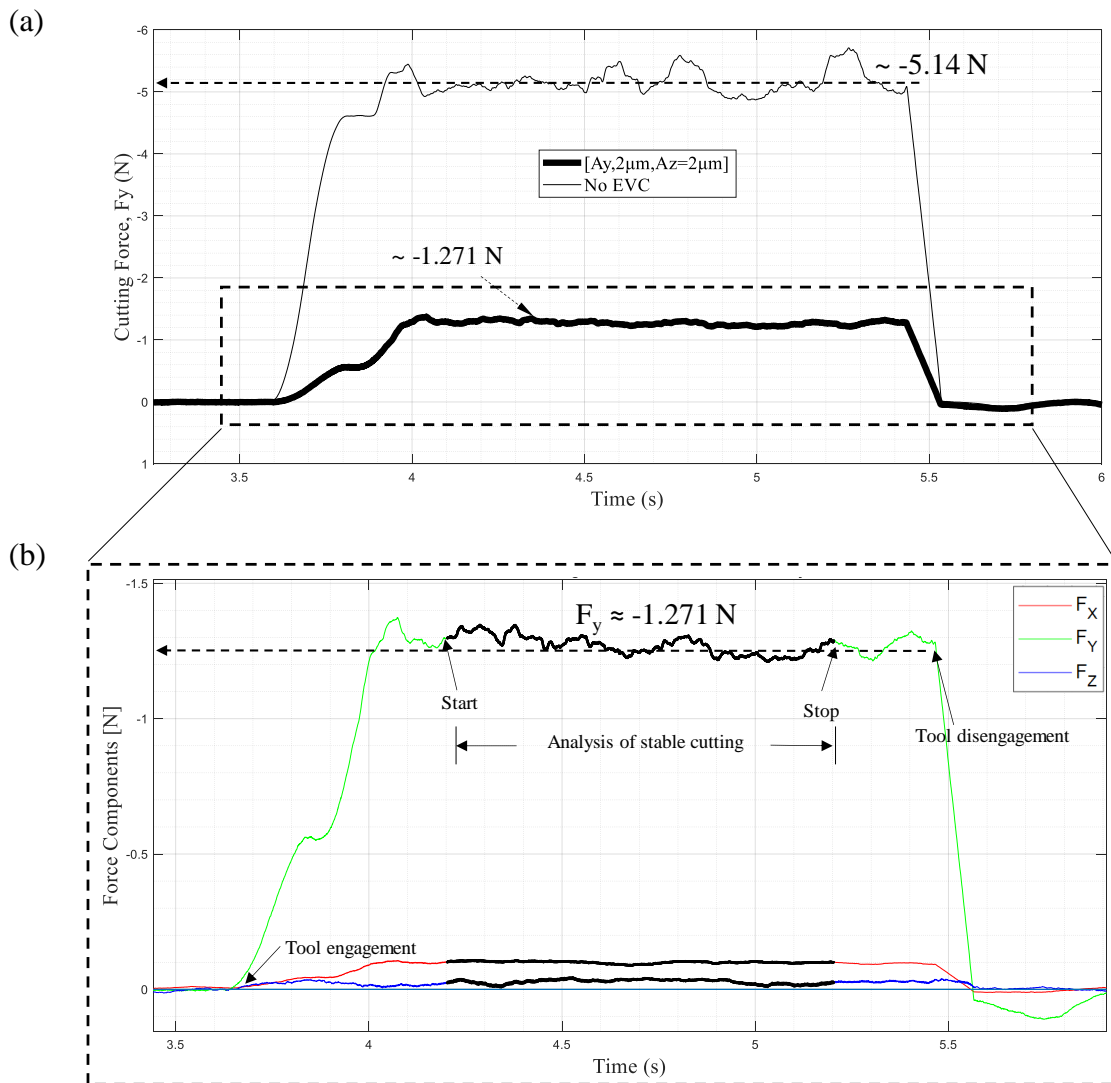


**Figure 4.12:** Detailed cutting force results comparing conventional orthogonal cutting to EVASPC: (a)  $F_y$  cutting force comparison between CC and EVASPC (characterized by  $A_y = 2\mu\text{m}$  and  $A_z = 2\mu\text{m}$ ), and (b) average cutting force values in  $F_x$ ,  $F_y$  and  $F_z$  directions for EVASPC experiment.

The observation that is reinforced from the previous chapter on V-groove fabrication is the extensive cutting force reduction properties of EVASPC. Here,  $F_y$  represents the  $Y$  component of cutting force, parallel to the feed direction, and  $F_z$  represents the thrust force component, perpendicular to feed direction, as seen in Figure 4.3.

Figure 4.12(a) demonstrates the quasi-dynamic behavior of the primary cutting force ( $F_y$ ) as a comparison between SPC and EVASPC processes. It should be noted that the EVASPC results presented above, with ellipse dimensions of  $A_y = 2 \mu\text{m}$  and  $A_z = 2 \mu\text{m}$ , demonstrated the study's highest mean cutting forces, at  $-1.271 \text{ N}$  (a reduction of 75% when compared to the conventional SPC process). Furthermore, the EVASPC experiment with the smallest  $F_y$  cutting forces ( $A_y = 6 \mu\text{m}$  and  $A_z = 6 \mu\text{m}$ ) provided force improvements over 86% (average cutting pass forces of  $-0.715 \text{ N}$ ). Similar cutting force stability demonstrated in the previous chapter is again emphasized in orthogonal EVASPC. The conventional SPC forces deviated from the mean value quite significantly ( $\sim 0.1651 \text{ N}$ ), while EVASPC limited this metric to nearly  $0.0125 \text{ N}$  (a 92% improvement).

Furthermore, Figure 4.12(b) details the EVASPC primary cutting force components in  $X$ ,  $Y$ , and  $Z$  directions, characterized by the cutting parameters in Table 4.2, along with EV amplitudes,  $A_y = 2 \mu\text{m}$  and  $A_z = 2 \mu\text{m}$ . At a first glance, a stark difference stands out between the SPC and the EVASPC force profiles through the initial spike in force of  $\sim -0.3 \text{ N}$ . This spike is characteristic of initial contact that bends/deflects the tool when penetrating the workpiece. Notably, this contact force was much smaller than the average cutting force as a consequence of the user-defined tool engagement angle ( $3^\circ$ ) that allowed for lower-impact contact. This deformation was gradually released as the process achieved stable cutting conditions.

Additionally, the thrust force ( $F_z$ ) demonstrated a similar force profile trend to  $F_y$  — however, in the opposite direction, as a result of the dynamometer  $Z$ -axis orientation. As hypothesized, this trend is a consequence of the vertical motion introduced by the elliptical vibration control unit, and additional frictional forces between the cutting face of the diamond tool and the workpiece chip formation. This being said, this trend wasn't



as prominent and distinct across all experiments. After executing all trials in Table 4.1, it became evident that this force component ( $F_z$ ) was relatively insignificant in comparison to the primary  $F_y$  component, and proved to show inconsistent and indecipherable fluctuations. These results ideally demonstrate the influence that ellipse orientation has on the thrust force component, however, such conclusions were not possible as a result of dynamometer resolution limitations and substantial apparatus vibrations.

As alluded to earlier in this chapter, there was no side-face contact between the tool and workpiece which explains the negligible average  $F_x$  values—and any lateral cutting force components can be considered as mechanical or electrical noise. Additional reasoning for  $F_x \approx 0$  N simply comes because orthogonal EVASPC suppresses (the majority of) process-induced tool-workpiece displacements. Moreover, the following are also plausible: i) the dynamic compliance of the cutting process becomes almost negligible, ii) cutting force coefficient  $K(\cdot)$  becomes constant for this set of machining parameters, and iii) surface topography is solely determined by the elliptical trajectory of the cutting tool tip.

Going further, analysis was completed to show the influence that each ellipse orientation has on the cutting forces ( $F_y$ ). The average cutting force for each EVASPC experiment was calculated across the stable cutting region of the final cutting pass, denoted in Figure 4.12. More specifically, once tool engagement was achieved, MATLAB waited 0.3 seconds before starting to record force signals—as to avoid the initial spike in force as a result of impact. From here, cutting force data was acquired for a time duration of 1.0 second, spanning a significant portion of the stable cutting time. As a result, Figure 4.13 demonstrates the experimental mean cutting forces ( $F_y$ ) for each ellipse orientation as a 3D bar plot, along with its corresponding ellipse, provided as a visual aid.

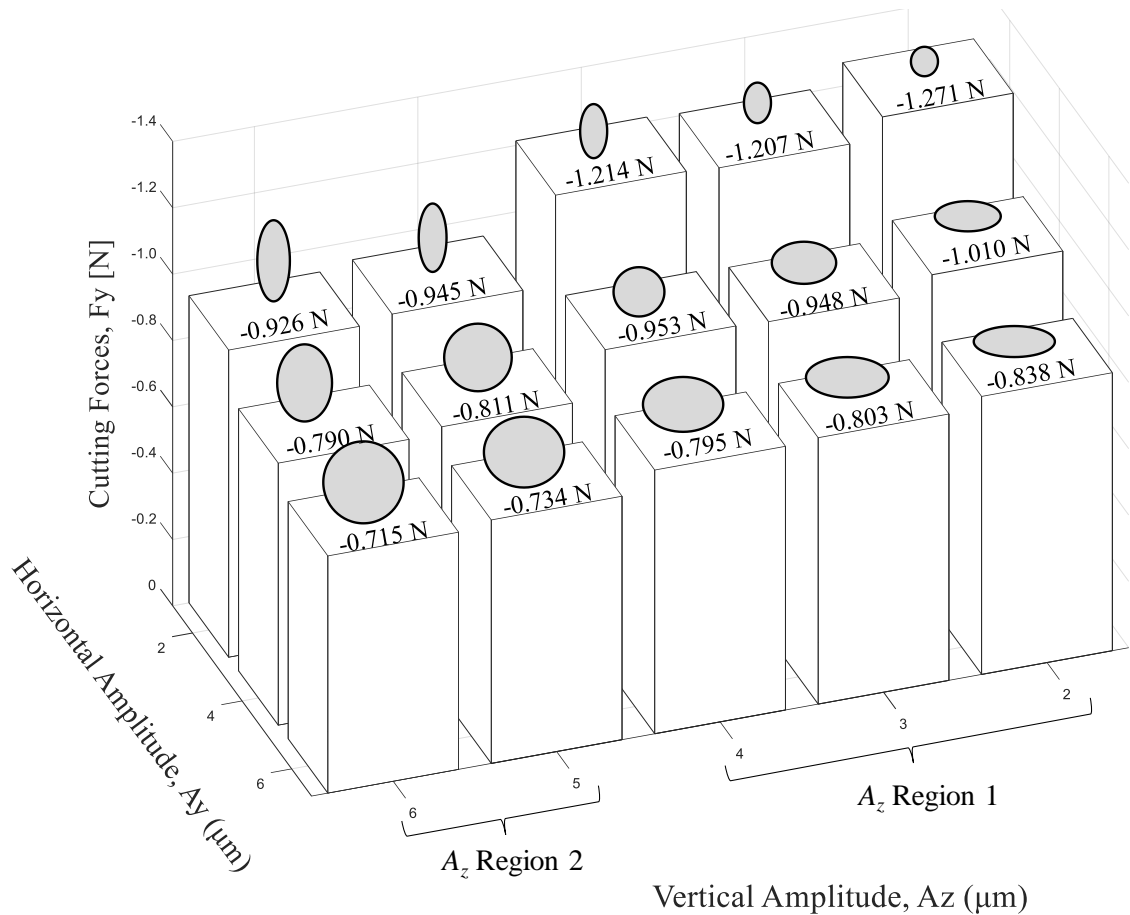


**Figure 4.13:** Summary of EV amplitude influence on cutting force generation ( $F_y$ ).

Many characteristics of Figure 4.13 exhibit the impact that ellipse orientation has on the cutting forces ( $F_y$ ) when using orthogonal EVASPC. This being said, the ultimate objective of this study is to analyze the influence that each EV amplitude ( $A_y$  and  $A_z$ ) has on cutting force results. Immediately, there is a consistent force reduction trend when analyzing each EV amplitude. Ultimately, as the amplitude increases, the cutting force consistently decreases.

In regards to the horizontal amplitude ( $A_y$ ), there are distinct trends when transitioning from small  $A_y$  to large  $A_y$  amplitudes, while maintaining a constant vertical amplitude ( $A_z$ ). The first transition (from  $A_y = 2 \mu\text{m}$  to  $A_y = 4 \mu\text{m}$ ) demonstrated an average force reduction of  $\sim 19\%$  between experiments, while the second transition (from  $A_y = 4 \mu\text{m}$  to  $A_y = 6 \mu\text{m}$ ) demonstrated an additional force reduction of  $\sim 14\%$ . Ultimately leading to a

total of 33% force reduction from the smallest to largest  $A_y$  (for a given  $A_z$ ). These force reduction tendencies can be explained through the impact that horizontal amplitudes have on the duty cycle of each cutting process. The duty cycle is defined by the ratio of Engaged Length between tool and workpiece to Total Ellipse circumference. As the value of the horizontal amplitude increases (for a fixed vertical amplitude,  $A_z$ ), the duty cycle of the cutting process decreases along with the cutting forces, Figure 4.14. This phenomenon is linked to the vertical amplitudes and will be detailed shortly.

Similar trends are shown for vertical EV amplitudes. As the  $A_z$  increases, the cutting forces ( $F_y$ ) consistently decreases (for a fixed horizontal amplitude,  $A_y$ ). Furthermore, there are two distinct regions of force reduction, denoted as ‘ $A_z$  Region 1’ and ‘ $A_z$  Region 2’ in Figure 4.13. The first region consists of amplitudes  $A_z = 2 \mu\text{m}$ ,  $3 \mu\text{m}$ , and  $4 \mu\text{m}$ , while the second contains the remaining amplitudes ( $A_z = 5 \mu\text{m}$  and  $6 \mu\text{m}$ ). Within these defined regions, there is relatively small and gradual cutting force change— in  $A_z$  Region 1 the average cutting force reduces by less than 5%, and  $A_z$  Region 2, less than 2.5%. However, there is a more prominent force drop when transitioning between  $A_z$  Region 1 and  $A_z$  Region 2 (as large a 22%). This can, once again, be directly explained through the process duty cycle and the cusp width. As the value of the vertical amplitude increases, the duty cycle of the cutting process decreases along with the cutting forces (for a fixed horizontal amplitude,  $A_y$ ).

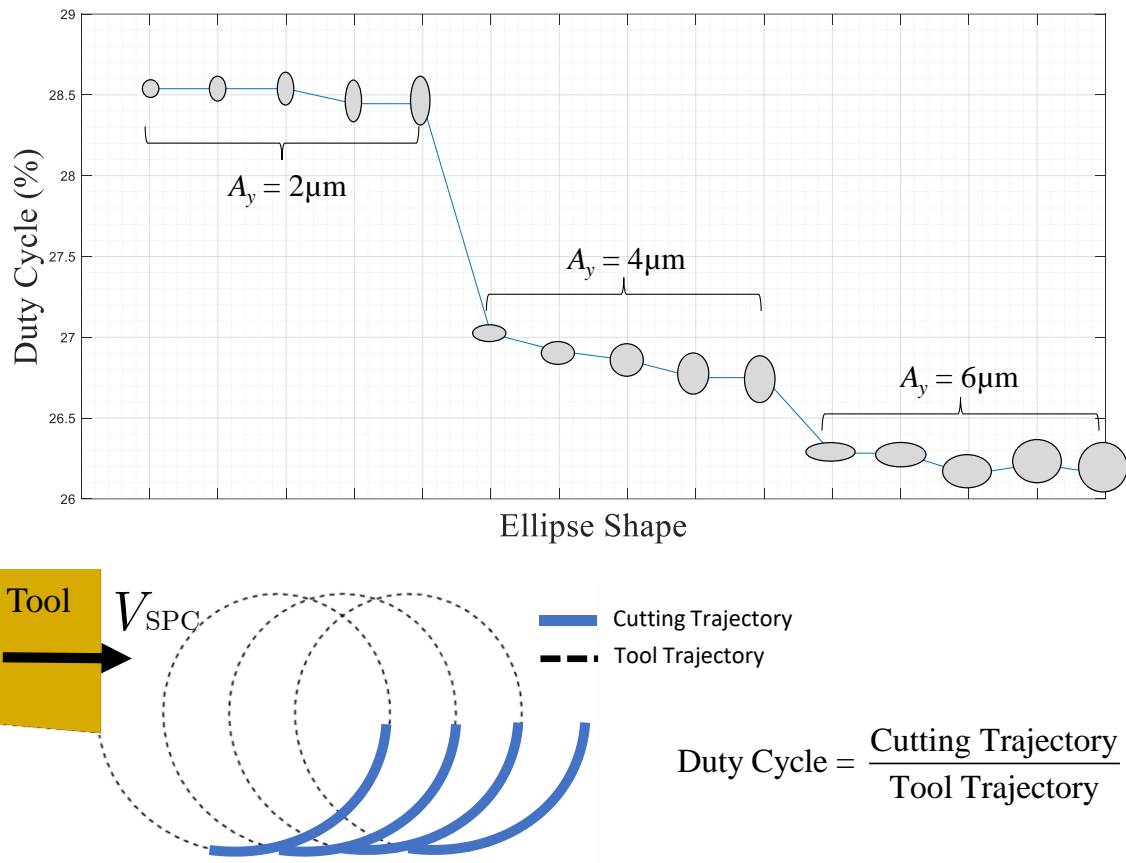


**Figure 4.14:** Cutting process duty cycle (%).

Building on this phenomenon, the duty cycle, and subsequently the cutting forces, are influenced by the overall ellipse size. The larger the ellipse, the smaller the duty cycle, and thus the smaller the cutting force. In other words, the cutting force is inversely related to the overall ellipse size, characterized by the ellipse area, Figure 4.15. As evidence, the smallest ellipse ( $A_y = 2 \mu\text{m}$  and  $A_z = 2 \mu\text{m}$ ), having an area of  $\sim 12.5 \mu\text{m}^2$ , produced the largest average force magnitude of  $\sim 1.271 \text{ N}$ . On the contrary, the largest ellipse ( $A_y = 6 \mu\text{m}$  and  $A_z = 6 \mu\text{m}$ ), with area  $\sim 113.1 \mu\text{m}^2$ , produced the smallest force magnitude of  $\sim 0.715 \text{ N}$ .

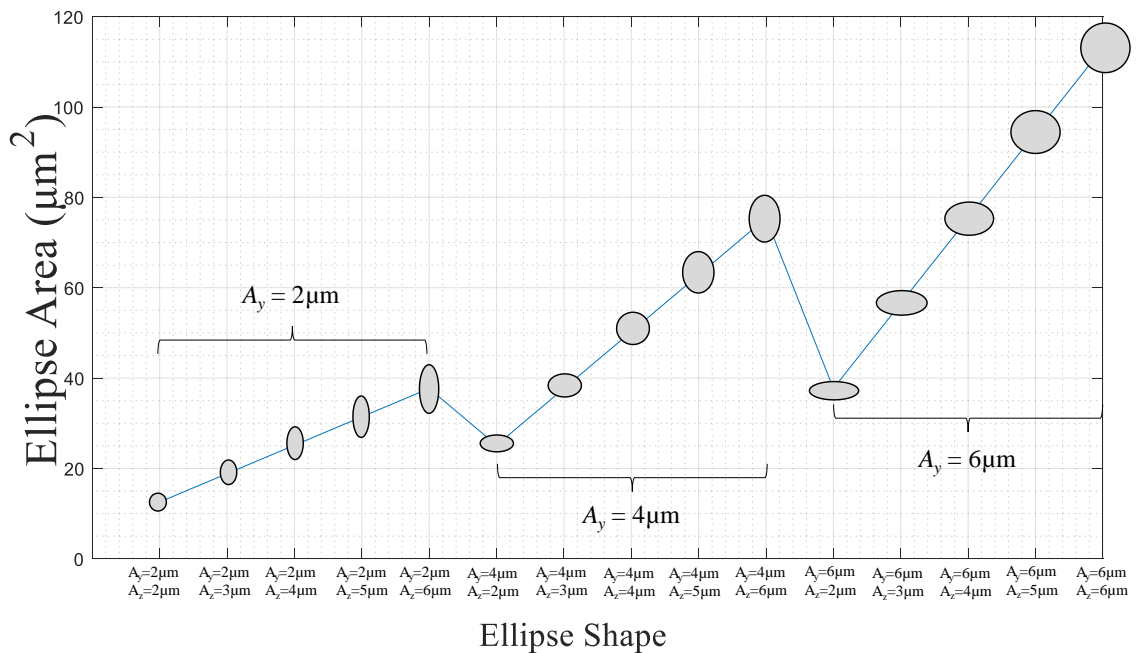


**Figure 4.15:** Ellipse area for each cutting experiment.

Inherently, as the size of the ellipse increase (either horizontally, vertically, or both), a smaller fraction of the overall ellipse contributes to the cutting process (Figure 4.14), thus, the fraction of time that the tool is engaged with the workpiece decreases for a cutting process, causing the resulting cutting forces to also decrease. This phenomenon comes from the cusp width, Figure 4.4, which is a function of the cutting speed ( $V_{SPC}$ ) and vibrational frequency ( $\omega$ ), not the ellipse shape; thus, it remains constant no matter the change in EV amplitudes [35]. As a result, when ellipse size increases the cutting force is distributed over a larger tool path, inherently lowering its average value.

## 4.6 Surface quality results

The average surface roughness ( $S_a$ ) is the second EVASPC outcome analyzed in this study. However, prior to the analysis of experimental results, it was crucial to verify that the desired cutting parameters were indeed being translated onto the workpiece—this was done through the examination of the fabricated surface. The SensoFar 3D optical profiler discussed in the earlier section captured a number of the user-defined cutting parameters listed in Table 4.2: the depth-of-cut, engagement angle, and the cutting speed (represented through the EV cusp width). The SensoFar's 10× DI Interferometry lens

was used to capture an initial 3D scan of the fabricated surface at the point of tool engagement, Figure 4.16(a). From this point, a 2D cross-section was extracted from the center of the scan, demonstrating the 10  $\mu\text{m}$  DoC and the 3° engagement angle, Figure 4.16(b).

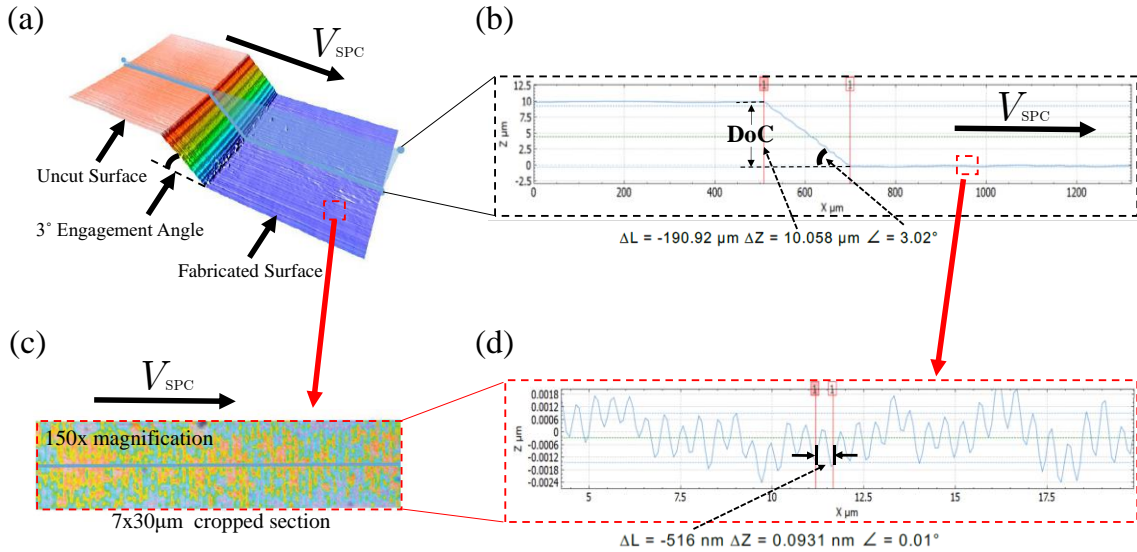


**Figure 4.16:** Experimental validation of cutting parameters: (a) 3D view of scan, (b) 2D profile validating desired DoC and engagement angle, (c) 150 $\times$  magnification of fabricated surface, and (d) 2D cross-section of EV-generated cusp and validation of EV cusp width.

Further magnification, Figure 4.16(c), was done using the 150 $\times$  EPI Confocal lens to reveal the periodic cusps produced on the fabricated surface as a result EV motion, from which the user-defined cutting parameters  $V_{SPC}$  and  $\omega$  were validated. The theoretical cusp width ( $T_{spatial, Theor.}$ ) was demonstrated earlier in Figure 4.4, and is defined by the ratio of cutting speed ( $V_{SPC}$ ) to vibrational frequency ( $\omega$ ) [29],

$$T_{spatial, Theor.} = \frac{V_{SPC}}{\omega} = \frac{1200[\text{mm} / \text{min}]}{41[\text{kHz}]} = 487\text{nm} \quad (4.1)$$

However, the corresponding 2D cross-section view in Figure 4.16(d) clearly demonstrated the cusp width to be  $\Delta L = 516 \text{ nm}$ —which does not exactly reflect the theoretical value in Equation 4.1. This comes as a result of the limitation in SensoFar lens pixel resolution (86 nm/pixel) when dealing with nano-scale surface structures.

Additional analysis was needed to ensure that the periodic structures seen in Figure 4.16(d) were indeed a product of EVASPC motion. For this purpose, frequency analysis was completed on the raw surface topography using a Fast Fourier Transform (FFT), where two separate arrays of data were extracted from the same 2D profile in Figure 4.16(d). The two frequencies in Figure 4.17 form the pixel resolution range provided by the 3D optical profile, from which point the actual cusp width should lay within.

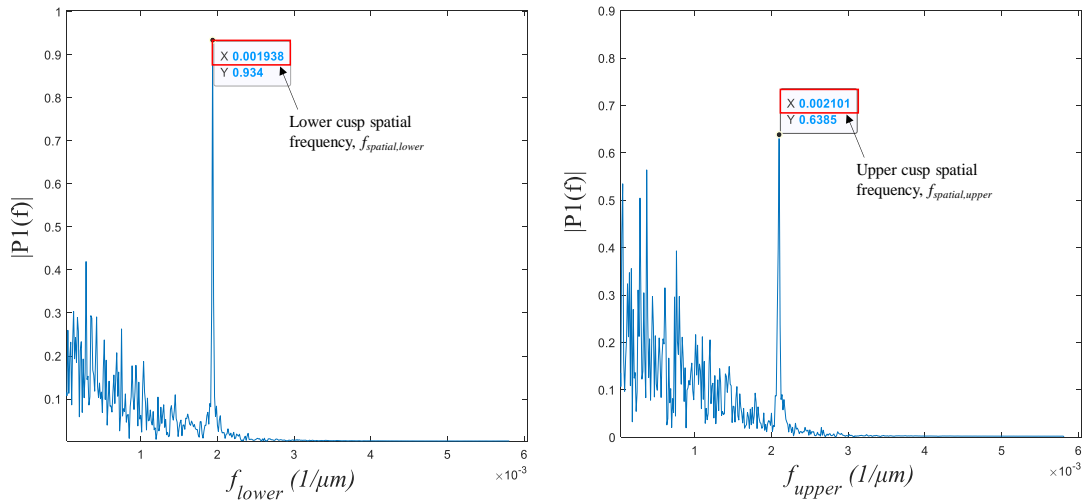


**Figure 4.17:** Raw surface FFT analysis in MATLAB: (a) FFT of cusp width for lower frequency range, and (b) FFT of cusp width for upper frequency range.

In Figure 4.17, MATLAB and its built-in ‘*fft*’ function captured the lower and upper spatial frequencies (defined by the 3D optical profiler pixel resolution) on the fabricated surface, and upon inversion, the respective cusp widths were acquired,

$$T_{\text{spatial, lower}} = \frac{1}{f_{\text{spatial, upper}}} = \frac{1}{0.002101_{\left[\frac{1}{\mu\text{m}}\right]}} = 476[\text{nm}] \quad (4.2)$$

$$T_{\text{spatial, upper}} = \frac{1}{f_{\text{spatial, lower}}} = \frac{1}{0.001938_{\left[\frac{1}{\mu\text{m}}\right]}} = 516[\text{nm}] \quad (4.3)$$

Consequently, the FFT analysis revealed its enhanced resolution of 40 nm (476 nm to 516 nm), doubling the SensoFar’s resolution. Ultimately demonstrating that the raw

cross-section surface profile exhibits the desired cusp width (theoretically at 487 nm) as a result of the defined cutting speed ( $V_{SPC}$ ) and vibrational frequency ( $\omega$ ).

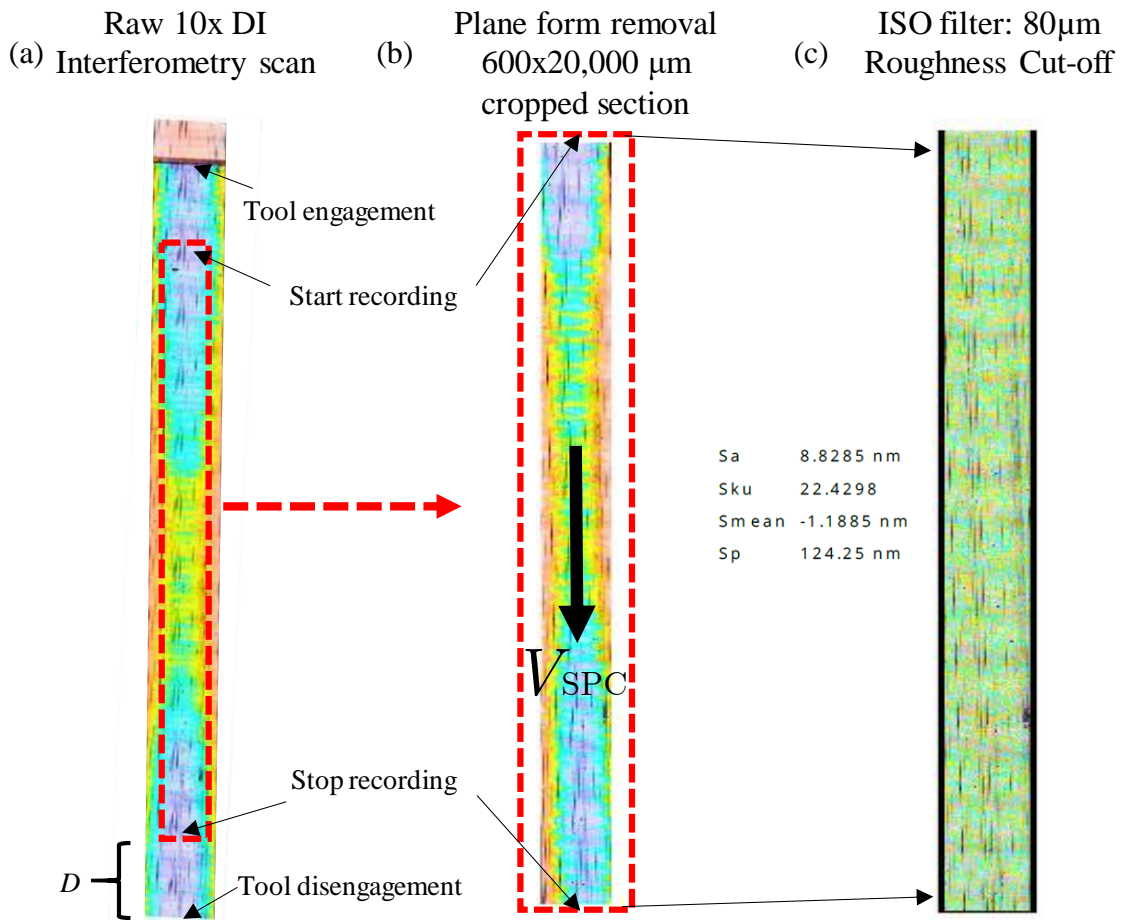


**Figure 4.18:** EVASPC surface roughness ( $S_a$ ) for orthogonal cutting experiment characterized by  $A_y = 6 \mu\text{m}$  and  $A_z = 2 \mu\text{m}$ : (a) Raw scan using 10× DI Interferometry lens, (b)  $600 \times 20,000 \mu\text{m}$  cropped section and plane form removal, and (c) ISO roughness filter 80 μm cut-off wavelength.

Following the cutting process and the experimental parameter validation, a detailed analysis of average surface roughness ( $S_a$ ) was done on each of the fifteen EVASPC samples. The 10x DI Interferometry lens was used to capture a scan of the entire rib length (Figure 4.18(a)), from which point a cropped section was extracted to match the time period over which average cutting force values were calculated (Figure 4.18(b)). More specifically, the length and location of the scan was determined from the cutting force plot in Figure 4.12(b). The overall scan length (20 mm) matches the distance



travelled by the tool during cutting force averaging—this is based on the tool cutting speed (1200 mm/min) and the time duration over which the averaging was calculated (1.0 second). The location of the cropped section was defined by  $D$  in Figure 4.18(a), which is the distance between the end of cutting force recording and the tool disengagement.  $D$  determined where the 20 mm scan would end with respect to the rib length. Specific post-processing procedures were then used to level and filter the raw topographical data according to industry standards (ISO 4288, ASME 46.1), Figure 4.18(b-c). Finally, Figure 4.18(c) shows the average surface roughness, seen to be as low as  $S_a = 8.8285$  nm—for the experiment consisting of EV amplitudes,  $A_y = 6$   $\mu\text{m}$  and  $A_z = 2$   $\mu\text{m}$ . For reference purposes, the industry standard for mirror-like surface finish is  $R_a < 100$  nm, while superfinishing—the hallmark surface finishing process—is capable of  $R_a \approx 25\text{--}200$  nm [15]. Recall that this experiment measured the areal surface roughness ( $S_a$ ) which is calculated over an 3D ISO standard-defined area, and provides a more advanced overview of surface quality compared to  $R_a$ . After further analysis, all EVASPC experiments comfortably surpassed this industry standard, Figure 4.19.

Similar to the cutting force section, analysis was completed to show the influence that ellipse orientation has on surface roughness ( $S_a$ ). This was done by scanning each rib using the procedure shown in Figure 4.18, and populating a matrix with the corresponding  $S_a$  values. Note, the scan for each experiment was taken over the same distance and location as the cutting force analysis in order to compare surface quality within the same region of the cutting process. As a result, Figure 4.19 demonstrates the experimental surface roughness ( $S_a$ ) for each ellipse orientation as a 3D bar plot, along with its corresponding ellipse provided as a visual aid.

Figure 4.19 shows various trends in surface roughness, both in the horizontal and vertical directions. However, throughout analysis, the most consistent observation demonstrated that the horizontal amplitude is the most significant EVC parameter when it comes to the influence on surface roughness—as  $A_y$  increases, the surface roughness decreases.

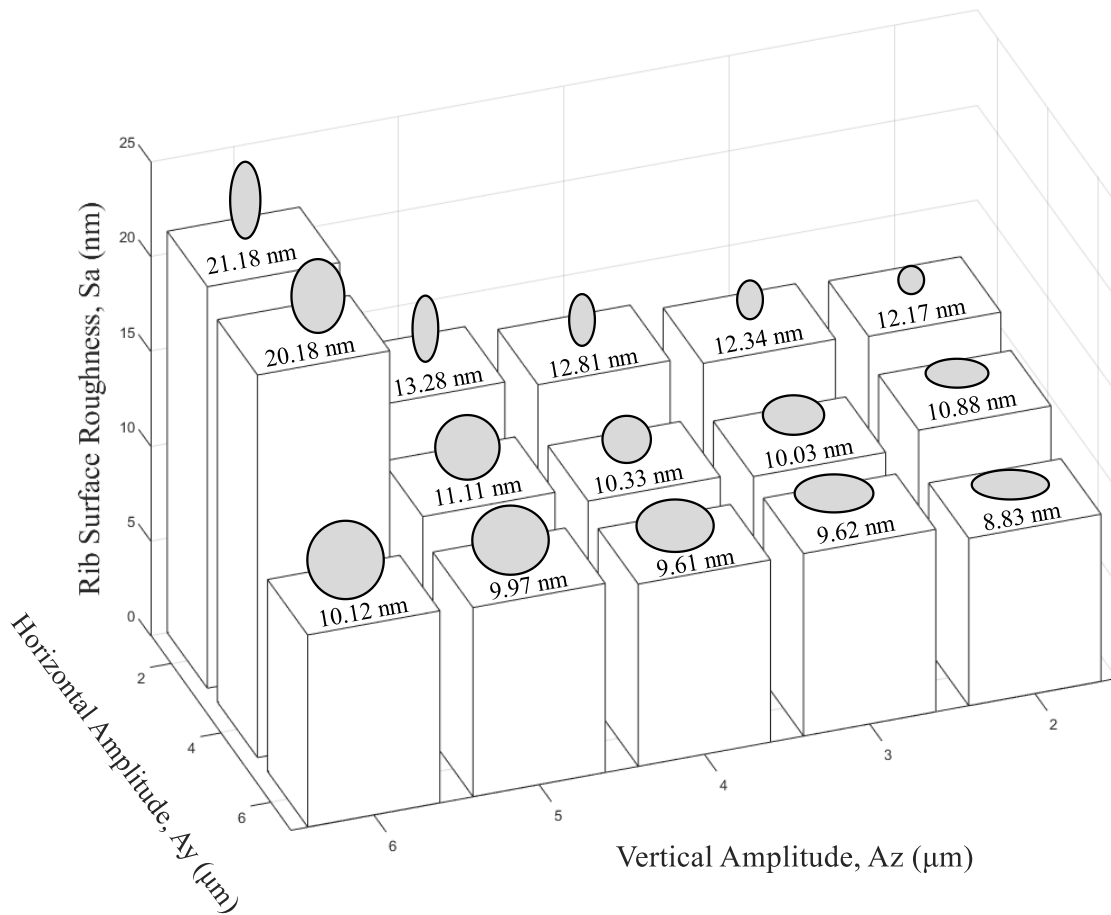


**Figure 4.19:** Summary of EV amplitude influence on surface roughness ( $S_a$ ).

Building on this, when analyzing the horizontal amplitudes ( $A_y = 2 \mu\text{m}$ ,  $4 \mu\text{m}$ , and  $6 \mu\text{m}$ ), it is evident that as  $A_y$  increases, the surface roughness decreases proportionately. Averaging in surface roughness reduction by  $\sim 2.3 \text{ nm}$  between each horizontal amplitude. Once again, this comes as a result of the cusp width discussed earlier. The cusp width is a function of  $V_{SPC}$  and  $\omega$ ; therefore, as the  $A_y$  increases, the ellipse trajectories overlap more, causing the cusp height to become shallower (see transition from Figure 4.3(a) to Figure 4.3(c)). Consequently, as the height of the cusps decrease, the overall surface roughness ( $S_a$ ) also decreases.

On the contrary, the incremental change in vertical amplitude ( $A_z$ ) appeared to have a smaller correlation to the surface roughness, where values seemed to fluctuate without a pattern. This being said, an alternative way to analyze this data is through the ellipse

shape point-of-view. Namely, the vertically-dominant ellipse orientations ( $A_z > A_y$ ). Such ellipse orientations are synonymous with surface texturing and surface functionality applications—meaning that as the  $A_z$  increases, EV-generated surface structures become more prominent.

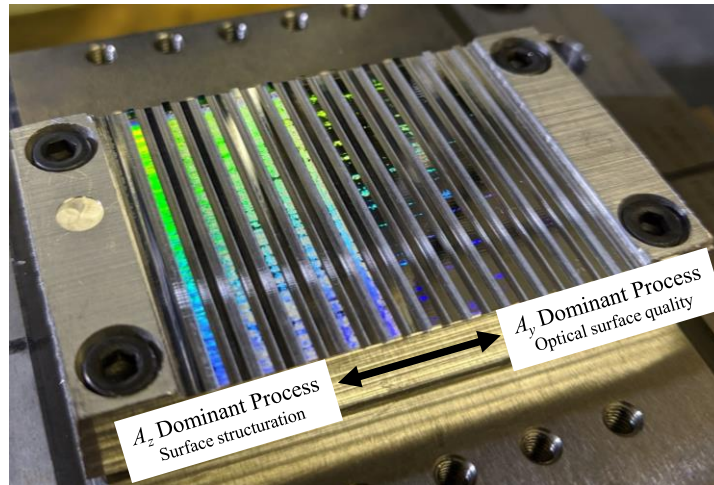


**Figure 4.20:** Physical demonstration of EV amplitude influence on surface quality using second workpiece from orthogonal EVASPC experiment.

These stark differences in EVASPC functionality were clear throughout the orthogonal EVASPC experiments, Figure 4.20. The left side of the workpiece was fabricated with the assistance of vertically-dominant EVASPC ( $A_z > A_y$ ), resulting in high surface colouration functionality. Moving to the right, the ellipse gradually transitions to a horizontally-dominant orientation ( $A_y > A_z$ ), producing an optical, mirror-like surface quality.

It was initially hypothesized that ultra-fast elliptical vibration assistance is responsible for the surface roughness formation while the slow motion cutting provided by the CNC stage influenced the surface waviness formation. From the analysis above, it is evident that the high frequency EVC motions are indeed translated into high frequency surface profiles, thus, influencing the surface roughness. On the other hand, the same analysis was completed for waviness  $S_a$ , however, the EV amplitude did not seem to consistently and predictably influence the waviness results; thus, no definitive conclusions were made.

## 4.7 Functional dependence analysis

So far, analysis has been completed to determine the effect that EV amplitude manipulation has on the individual cutting process outputs: average cutting force magnitude and surface roughness. Figure 4.21 provides a comparative plot that summarizes the individual findings so far: (a) demonstrates a bar plot of the average cutting forces ( $F_y$ ) while the colourmap represents the corresponding surface roughness, while (b) inversely reveals the surface roughness plot with cutting force ( $F_y$ ) colourmap. While trends were observed for each respective trial, the following functional dependence analysis will demonstrate the relationship between process inputs and process outputs across the entire parametric study. Ultimately, this section develops a regression model for the average cutting forces ( $F_y$ ) and the surface roughness ( $S_a$ ), along with their respective response models.

More specifically, statistical analysis software, Tableau, was used to formulate a correlation between input process parameters and output process metrics. This correlation was created in the form of a regression model for both the cutting force and surface roughness. A list of selected input process parameters were calculated for each experiment and imported into the model, Figure 4.22(a) and Figure 4.23(a). The  $S_a$ ,  $A_y$ ,  $A_z$ , *ellipse area*, and *duty cycle* have already been discussed, however the *effective ellipse area* and *engaged time* and *engaged length* variables are new concepts. The *effective ellipse area* is the portion of the ellipse that is transferred into the formation of surface cusps, while the *engaged time* and *engaged length* are the portion of the tool trajectory that is in contact with the workpiece, Figure 4.14. These input parameters sufficiently describe the EVASPC process and are uniquely defined by each ellipse shape as a result of EV amplitude control. From here, a multi-input regression model was generated, demonstrating the predicted output data versus the actual experimental data.

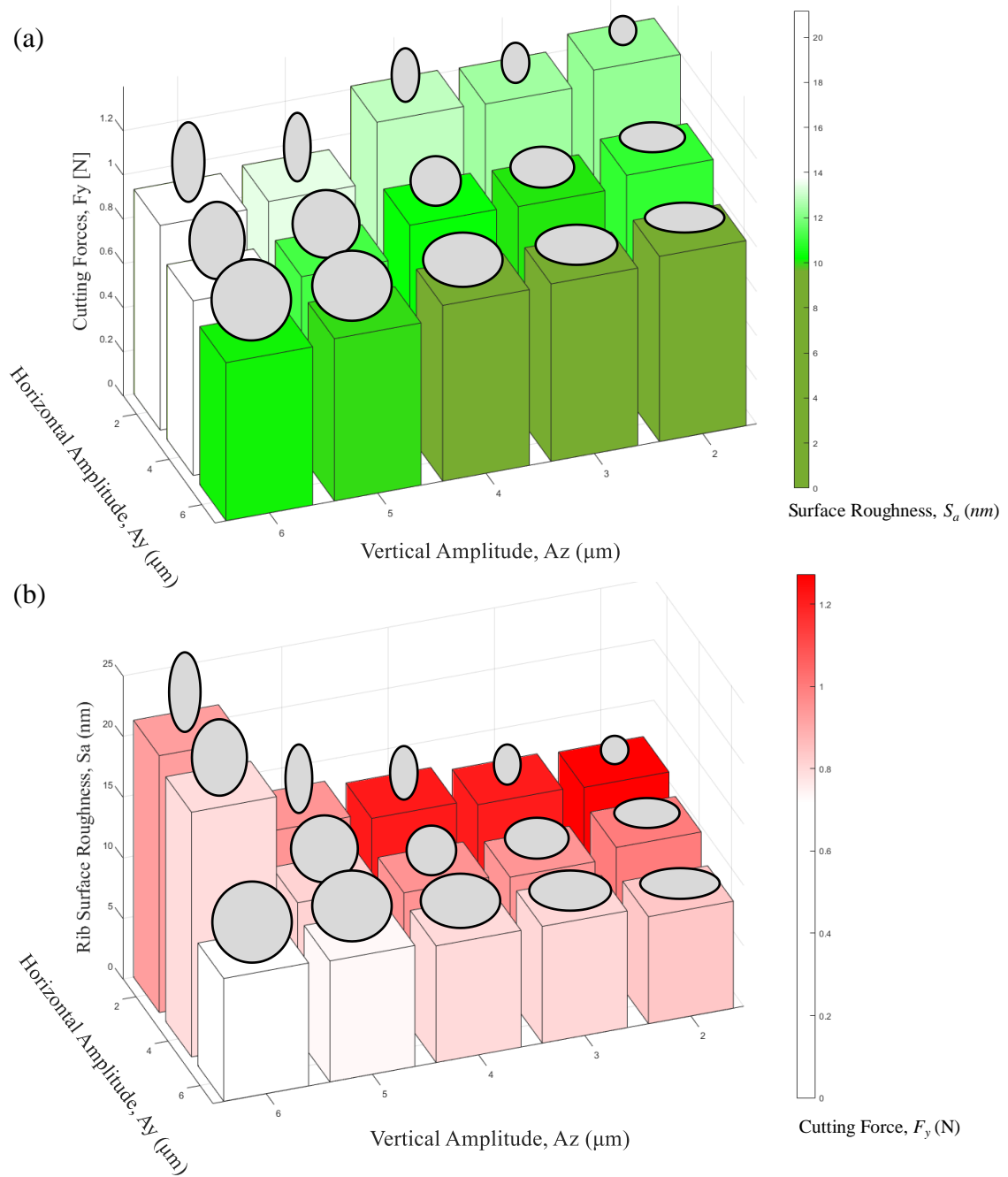


**Figure 4.21:** Comparative parametric study plot: (a) Average  $F_y$  bar plot with colourmap signifying ( $S_a$ ), and (b) average  $S_a$  bar plot with colourmap signifying  $F_y$ .

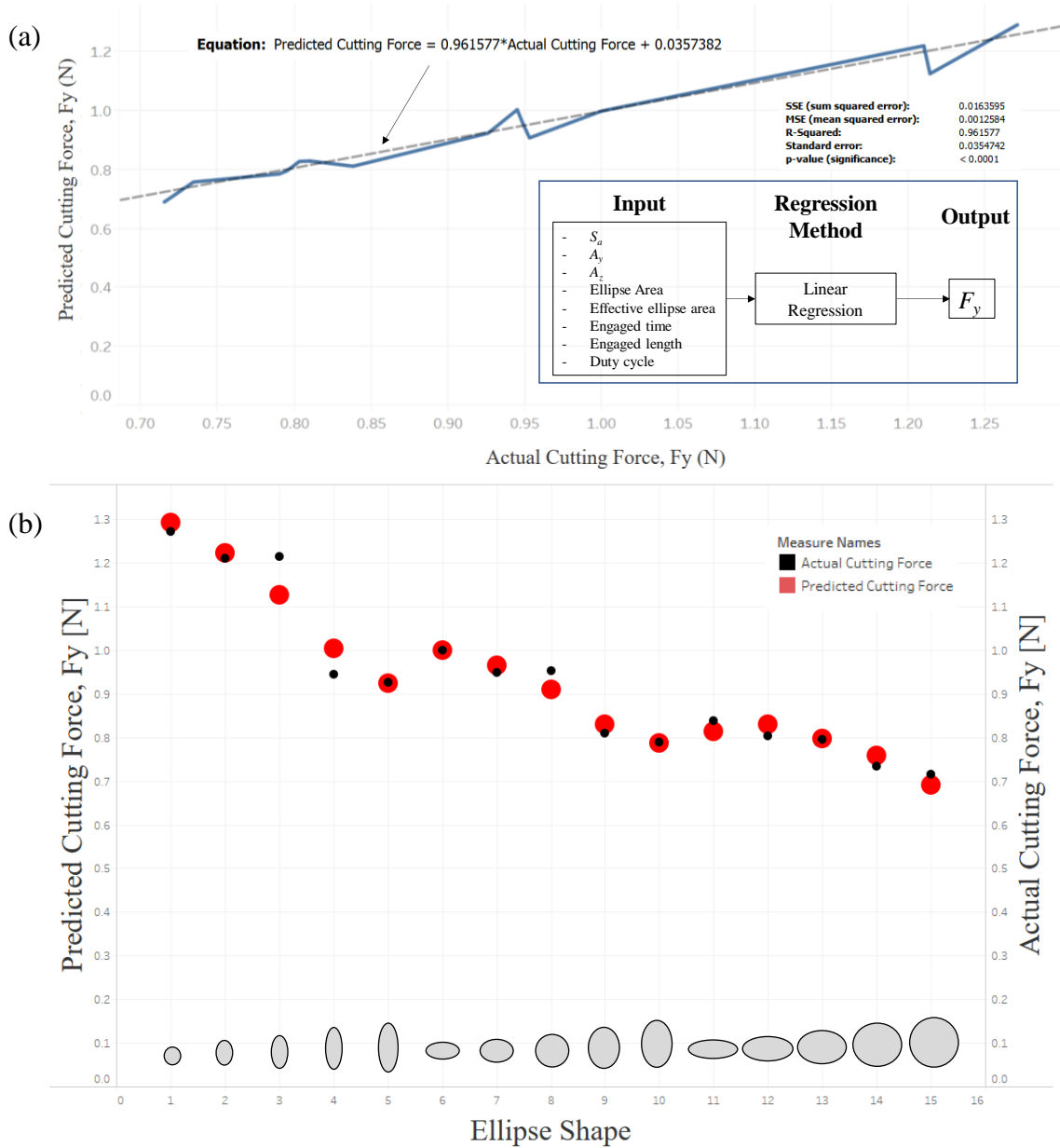


**Figure 4.22:** Cutting force ( $F_y$ ) regression model: (a) Predicted cutting force vs. actual cutting force plot, and (b) cutting force response plot for each ellipse shape.

For the cutting force predictive model, a linear regression generated a high correlation between the independent variables (*Inputs*) and the dependent variable (cutting force,  $F_y$ ), Figure 4.22(a). The relationship between the input variables and output  $F_y$  link back to Figure 4.1 in which cutting forces are a direct function of the tool trajectory—produced by SPC parameters and the additional EVC parameters. Additionally, the most significant predictors of cutting force were observed to come from the ellipse area and the engaged length between the tool and workpiece, with  $R^2$  values of 0.884 and 0.878, respectively. Both parameters demonstrated a largely negative relationship with  $F_y$ ; thus, as they increase  $F_y$  decreases. Following the predicted cutting force results, a response plot demonstrates the accuracy at which the regression model can predict the cutting forces based on the calculated model for each ellipse shape used in the experiments, Figure 4.22(b). More generally, as was seen in the comparative study, there is a consistent downwards trending in the average cutting force  $F_y$  as the size of the ellipse increases.

Similar analysis was completed for the surface roughness, demonstrating acceptable, yet less significant results. It was more difficult to generate an appropriate regression model, stemming from the intermediary cutting process dynamics that cannot be described through a simple model. Contrary to the cutting forces, surface topographical results are a function of both the tool trajectory and the cutting forces themselves (Figure 4.1); therefore, introducing more complexity into the predictive model. This being said, Tableau generated an acceptably accurate regression model based on the process inputs (Figure 4.23(a)), and as expected from Figure 4.19, the most significant predictor of surface roughness is provided through its inverse correlation with the horizontal amplitude, where  $R^2 = 0.3818$ ; however, this correlation is still very limited. Furthermore, through Figure 4.23(b), as the orientation of the ellipse translates from a horizontal-oriented ellipse towards a vertically-oriented ellipse the corresponding  $S_a$  is observed to increase in a U-shaped trajectory. On this note, two obvious examples of vertically-dominant orientations, Ellipse Shape 5 and 10 (Figure 4.23(b)), appear to have significantly larger  $S_a$  values compared to the others. While there is no conclusive answer to this observation, it is hypothesized that these large  $S_a$  trials offer enhanced surface functionality characteristics at the expense of average  $S_a$ .

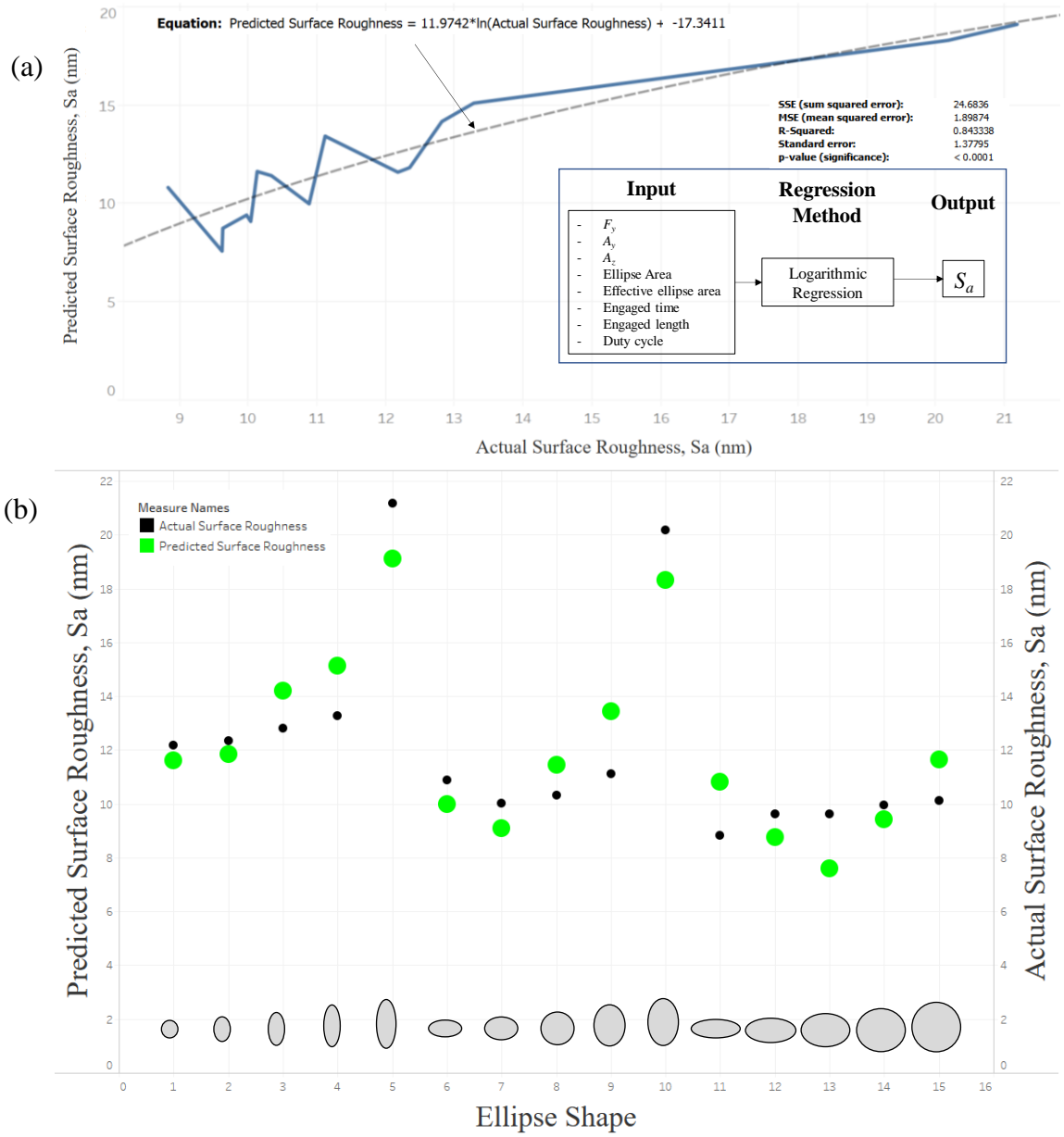


**Figure 4.23:** Surface roughness ( $S_a$ ) regression model: (a) Predicted surface roughness vs. actual surface roughness plot, and (b) surface roughness response plot for each ellipse shape.



The functional dependence analysis demonstrated through the preceding regression models deliver an adequate method of predicting additional elliptical vibration assisted cutting processes that were not completed experimentally. Such models can be used in future research applications to provide a relatively reliable metric for predicting the influence that intermediary ellipse orientations have on cutting forces and surface roughness.

## **4.8 Finite element modeling**

### *4.8.1 General setup*

To further predict the influence that elliptical vibrations have on the process of orthogonal SPC, a finite element method model (FEM) was used. FEM modeling is a popular method of reproducing and predicting experimental results given appropriate user-defined process conditions and assumptions, all the while doing so in a time and cost-effective manner. The current objective of this FEM model is to validate cutting force results observed in the experimental parametric study completed earlier, from which point predictive cutting force analysis can then be executed on machining conditions that were not used during experimentation. In addition, the FEM simulations strive to provide a more detailed explanation of process-specific physical phenomena through analysis of high-resolution cutting force results, stress distributions, and workpiece chip formation—all of which are difficult (if not impossible) to capture during the experimental trials.

Thus, the following FEM model was created using an ABAQUS/Explicit solver and Lagrangian-based formulation. This method was suggested to provide appropriate analysis for EVASPC due to its inherent compatibility with highly discontinuous models, high-speed and high-frequency impact, quasi-static, and enhanced computing efficiency for large models [62]—all of which are crucial for EVASPC.

Furthermore, the ABAQUS/Explicit simulation was created to demonstrate the cutting process performance as a result of EVASPC motion kinematics, deformation mechanics, tool-workpiece material interaction properties, and chip formation. One way of doing this is through the visual chip deformation and separation. More specifically, SPC can

produce one of three primary chips types: continuous chips, serrated chips and discontinuous chips [63]. The continuous chip is synonymous with conventional no-EVC cutting, in which a single unbroken chip is removed as the tool translates across the cutting length. This being said, the unbroken chip has tendencies to obstruct the cutting process which may lead to undesired damage to the workpiece and/or tool. Conversely, such problems have been limited, and even mitigated, through the employment of serrated chips. Serrated chip formation (or segmented continuous chips) and EVC processes have been seen to go hand-in-hand. More specifically, small chip segments are formed due to the development of adiabatic shear banding and crack initiation mechanisms within the primary shear zone [63]. The adiabatic shear banding then translates to the localization of plastic deformation, resulting in shear fracture, ultimately leading to the small fractured chip segments. Furthermore, these small segments remain attached as a result of the microscopic chip fractures in the primary deformation zone; the interface between each overstrained chip segment is essentially welded together as a result of high contact compression, thermal properties, and chemical reactions. Ultimately, such chips are broken and removed from the cutting area, thus proving to be more advantageous for SPC processes. Finally, discontinuous chips occur when small segments of chips evacuate from the cutting region before build-up and ‘self-welding’ can be achieved, however this method is not as prominent as the preceding methods. All this being said, both serrated and discontinuous chip formation is encouraged through EVC’s intermittent tool-workpiece contact, however due to high contact stress and temperature gradients, serrated chips have proven more prevalent.

#### 4.8.2 *Material parameters*

As discussed, the FEM simulation was executed through the definition of an ABAQUS/Explicit 3D assembly model. Two part instances were extruded to represent the monocrystalline diamond cutting tool and Aluminum 6061 workpiece. Table 4.3 and Table 4.4 outline the dimensional and material properties for each respective instance, which each mimic the experimental cutting conditions, along with the Johnson-Cook damage criterion.

**Table 4.3:** Cutting tool properties.

<b>Tool Dimensional Parameters</b>	
Tool Cutting Face Width (mm)	3.2
Tool Clearance Angle (°)	5
Rake angle (°)	0
<b>Tool Material Properties</b>	
Material	Monocrystalline Diamond
Density (kg/m <sup>3</sup> )	3520
Young's Modulus (GPa)	1050
Poisson's Ratio	0.1

**Table 4.4:** Workpiece properties.

<b>Workpiece Dimensional Parameters</b>	
Length (mm)	5.0
Width (mm)	0.8
Height (mm)	1.0
<b>Workpiece Material Properties</b>	
Material	Aluminum 6061
Density (kg/m <sup>3</sup> )	2700
Young's Modulus (GPa)	70
Poisson's Ratio	0.33

**Table 4.5:** Johnson-Cook damage criteria.

<b>Workpiece Johnson-Cook Damage Evolution</b>	<b>d1</b>	<b>d2</b>	<b>d3</b>	<b>d4</b>	<b>d5</b>	<b>Reference strain rate</b>
		-0.77	1.45	0.47	0	1.6
<b>Workpiece Johnson-Cook Plastic Hardening</b>	<b>A</b>	<b>B</b>	<b>C</b>	<b>n</b>	<b>m</b>	<b><math>\epsilon_0</math></b>
	324	114	0.002	0.42	1.34	1

Of note, literature suggested the use of a Johnson-Cook model for workpiece material failure when it comes to orthogonal single point cutting in ABAQUS (Table 4.5). This model has been validated as an appropriate constitutive model that captures the thermo-viscoplastic characteristics of high speed cutting for workpiece damage evolution and plastic hardening [64].

#### 4.8.3 Instance meshing

From this point, both the tool and workpiece were partitioned according to specific cutting regions, Figure 4.24. The ‘tool cutting region’ was created in order provide enhanced mesh refinement for high-resolution stress distribution plots. Additionally, in the EVASPC model, an extra partitioned section ( $200\mu\text{m} \times 100\mu\text{m}$ ) was introduced in the cutting region for further contact force analysis between the tool and workpiece, Figure 4.25(b). Likewise, the workpiece ‘cut surface’ region was partitioned  $50\mu\text{m}$  from the top face to provide highly refined mesh in the region where tool-workpiece interactions occur, ultimately allowing for accurate chip formation. Furthermore, a sacrificial cell partition acted as a buffer region between the cutting region and the rest of the unaffected workpiece. This region prevented excessive distortion of the workpiece and encouraged chip separation.

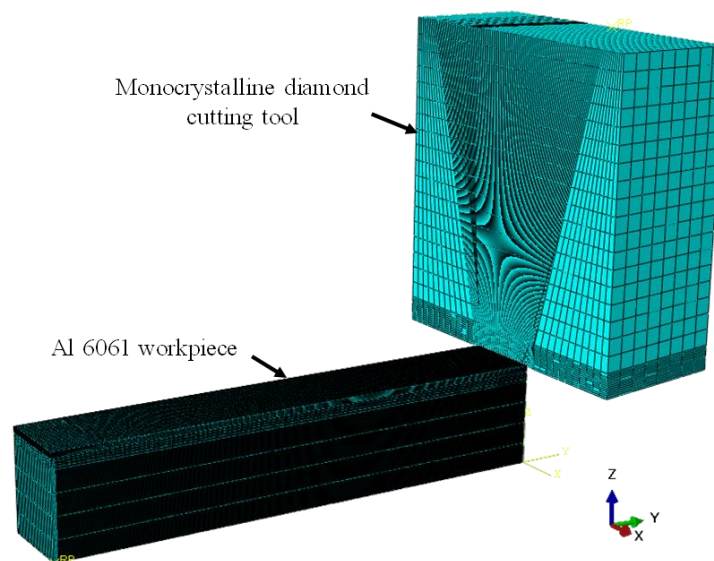


**Figure 4.24:** FEM meshed assembly setup with tool and workpiece.

Each instance was then meshed using first-order Hex, 3D Stress, C3D8R 8-node linear brick elements with reduced integration and default hourglass control in order to improve simulation efficiency while maintaining acceptable results. The cutting region on the tool was meshed with element size  $10\mu\text{m} \times 10\mu\text{m}$  in cross-section, while the remaining geometry used the default mesh settings. These dimensions were chosen in order to enhance contact mechanics between the tool and workpiece, as well as improve visual contact stress results. Element size on the workpiece cut surface section was  $2\mu\text{m} \times 2\mu\text{m}$  cross-section while the element height was  $0.5\mu\text{m}$  in order to capture the micron-scale EVC shearing motion and improve chip formation due to elliptical vibration motions.

Following mesh definition, a mesh quality check was completed for both the workpiece and the cutting tool using the built-in meshing verification tool in order to verify that appropriate mesh was being used for modeling. Using the default, and suggested, aspect ratio (AR) threshold of  $>10$  [65], both parts demonstrated relatively acceptable values: the tool showed an average  $\text{AR} = 6.28$ , while the workpiece showed a somewhat larger average  $\text{AR} = 11.30$ . A major reason for the larger AR values came from the non-uniform mesh element geometry present in the refined cutting region on both the tool and workpiece. On the other hand, the calculated stable time increment for the cutting tool and workpiece were also observed,  $1.38\text{e-}09$  and  $1.46\text{e-}10$ , respectively. The fact that the average stable time increment was smaller than actual stable increment ( $6.5\text{e-}08$ ) is good, but the difference should ideally be larger than it currently is. In the future work, it will be crucial to perform further analysis on appropriate mesh parameters, because better mesh quality would most likely increase the time step, and consequently reduce the overall runtime as well as improving the aspect ratios.

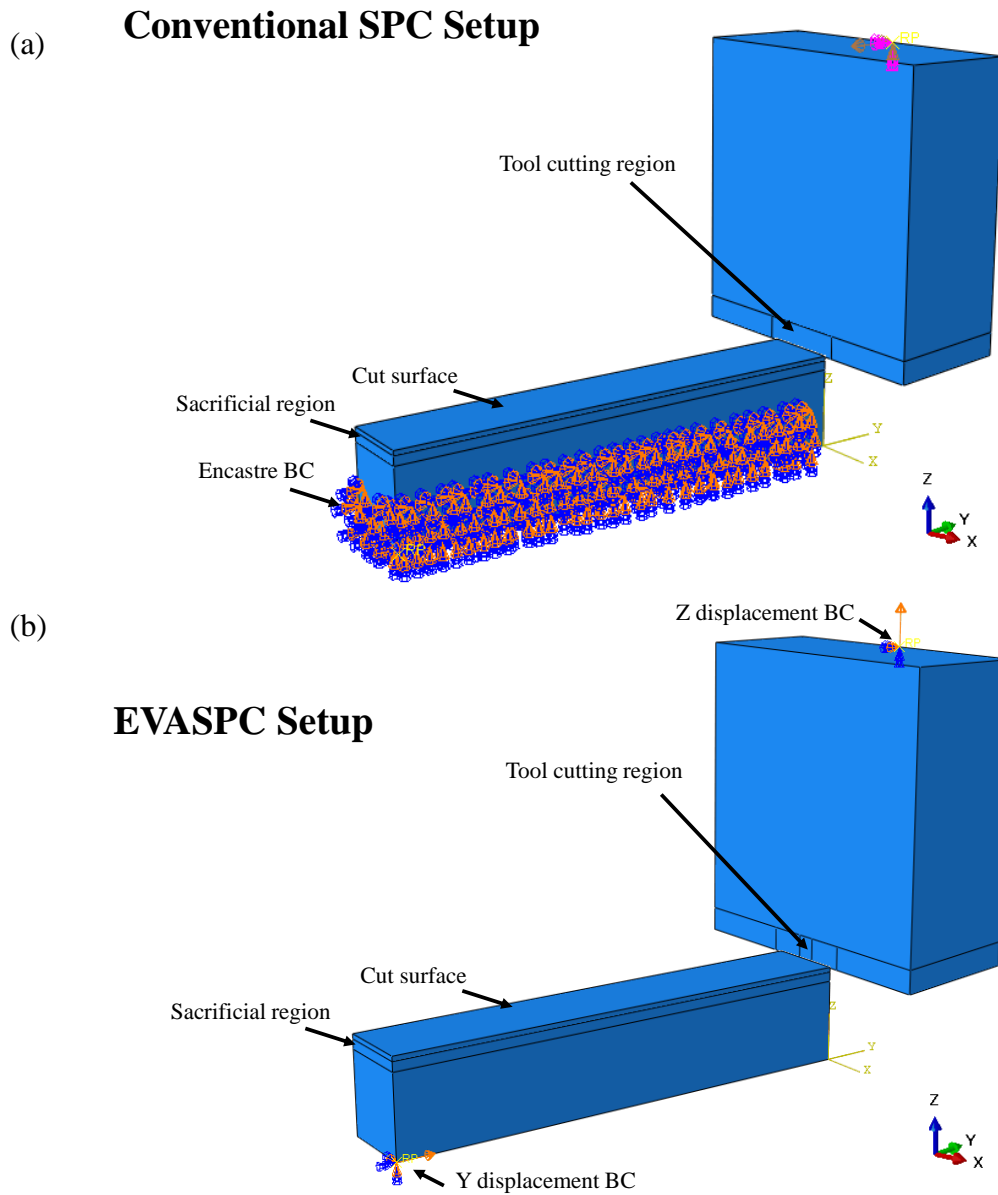


**Figure 4.25:** FEM model assembly setup with tool and workpiece BC: (a) Conventional SPC setup, and (b) EVASPC setup.

#### 4.8.4 *Boundary conditions*

In both model assemblies, the tool was aligned with the workpiece in the same manner as the experiment, such that the tool translated in the  $-Y$  direction at a DoC =  $10\ \mu\text{m}$ . The boundary conditions (BC) used to define the tool translation were the major differentiators between the conventional SPC model and the EVASPC model. In the SPC model, two simple BC's were defined, Figure 4.24(a): an encastre BC and a spatial

velocity BC. The encastre BC was placed on the lower half of the workpiece, preventing any translation and/or rotation of the instance. Contrarily, a simple spatial velocity BC was placed on the tool reference point (RP), such that the entire rigid body translated at  $V_{SPC} = 1200$  mm/min in the  $-Y$  direction, Figure 4.26.

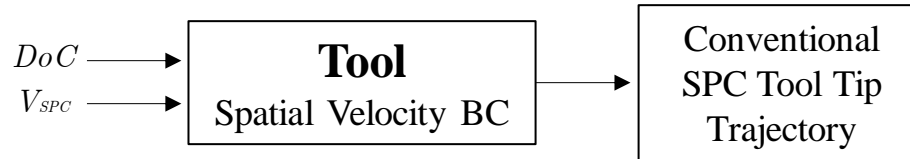


**Figure 4.26:** Conventional SPC boundary conditions.

Conversely, the EVASPC model proved to be much more difficult. In order to integrate EVC motions into the traditional SPC process, EV amplitudes needed to be incorporated ( $A_y = 2$   $\mu\text{m}$  and  $A_z = 2$   $\mu\text{m}$  in this model). Thus, three primary motions were required: spatial displacement along the  $Y$ -axis (similar to  $V_{SPC}$  in the SPC model) as well as two vibrational motions in the  $Y$  and  $Z$  directions ( $A_y$  and  $A_z$ , respectively). In order to achieve this, both the tool and the workpiece were given displacement BC's, Figure 4.25(b) and Figure 4.27. Ultimately, the combination of these motions produced the tool tip trajectory identical to that seen in Chapter 2.

For the EVASPC model, each elliptical revolution was divided into six evenly spaced  $Y$  and  $Z$  displacement data points that described the tool motion. In ABAQUS/explicit, these data points defined the incremental displacement and corresponding time steps ( $1.21951\text{e-}05$ ) between each incremental movement of the tool throughout the cutting process.

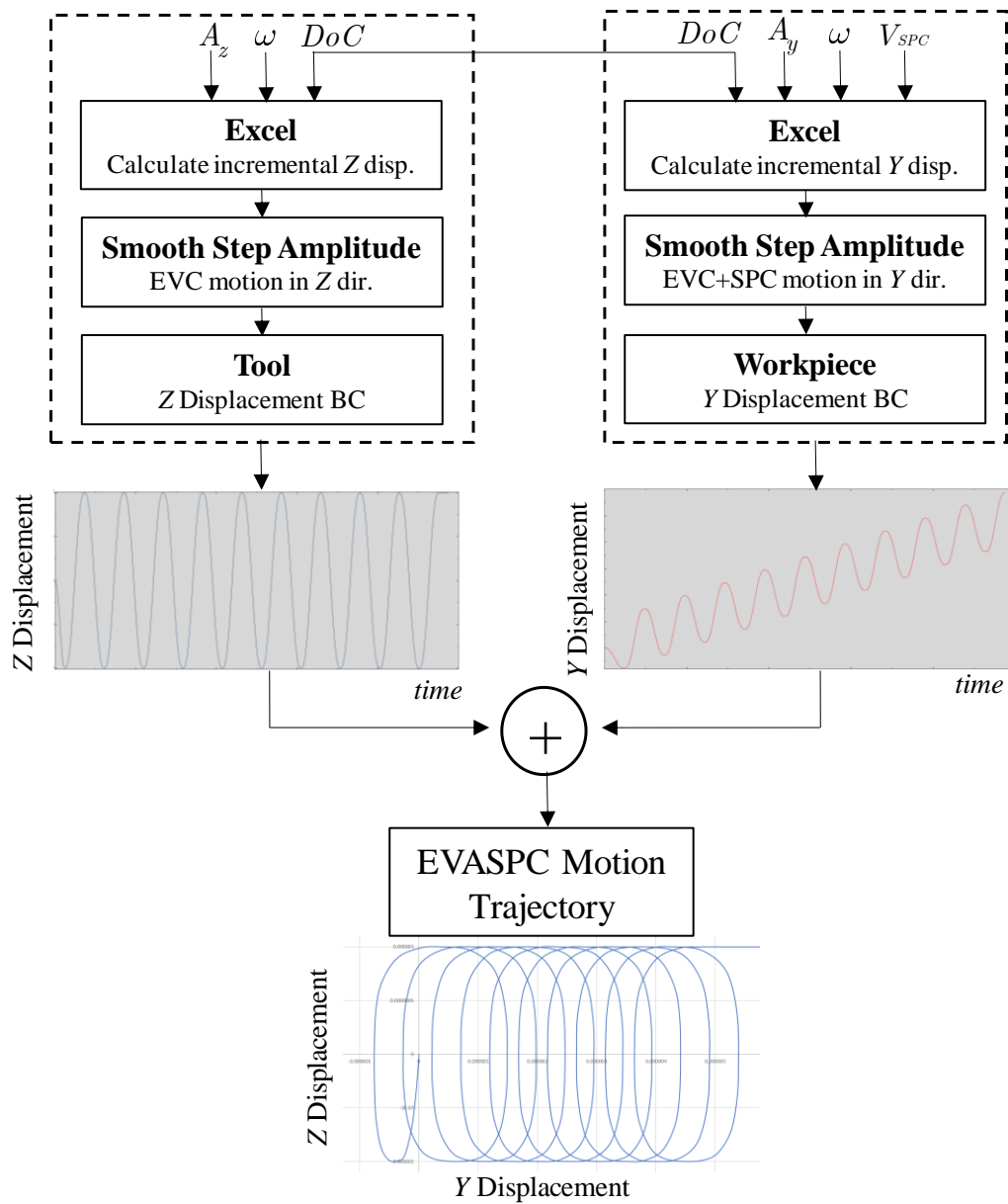


**Figure 4.27:** EVC and SPC boundary conditions that produce governing EVASPC motion trajectory.

The workpiece provided the  $Y$  motions (both translation and vibration), and this was done using an advanced displacement BC that was placed at the workpiece reference point (RP), Figure 4.25(b). This RP was associated with a rigid body definition on the bottom section of the workpiece which allowed for a clean and simplified BC definition. As mentioned, the  $Y$  motion was defined as a displacement BC, however, was ultimately driven by an advanced smooth-step amplitude multiplier that described the vibrational



and translational  $Y$  motions based on the DoC, vibrational frequency ( $\omega$ ), and the cutting speed ( $V_{SPC}$ ). First, the amplitude multiplier values were calculated in Excel for each simulation time increment and then imported into the Amplitude table in CAE, from which point it was linked to the governing workpiece displacement BC. The combination of translational ( $V_{SPC} = 1200$  mm/min) and vibrational ( $A_y = 2$   $\mu\text{m}$ )  $Y$  motion eventually creates a sloped sinusoidal displacement trajectory, Figure 4.27.

On the other hand, the tool instance provided the  $Z$  direction elliptical vibrations ( $A_z = 2$   $\mu\text{m}$ ) through simple amplitude modulation that vibrated from  $-1$   $\mu\text{m}$  to  $+1$   $\mu\text{m}$  with respect to the nominal DoC, as seen through the sinusoidal motion in Figure 4.27.

#### 4.8.5 *Friction consideration*

Finally, once the EVASPC motions were defined, the interaction between tool and workpiece were defined using a general body contact pair. More specifically, the tool surface and workpiece ‘cut surface’ interacted according to a penalty contact method with constant frictional coefficient ( $\mu = 0.30$ ), based on popular literature [66]. It is important to note that the author understands the classical Coulomb’s friction model isn’t the most appropriate model for micromachining, let alone EVASPC. Literature has demonstrated that LuGre’s dynamic friction model provides the most accurate representation of EVASPC’s intermittent contact, in which the friction coefficient ( $\mu$ ) varies based on the relative velocity between the tool and workpiece cutting surfaces [67]. This formulation is based on the theoretical deflection of so-called ‘bristles’ as the tool shears through the workpiece. This bristle deflection, and consequently the friction coefficient, comes as a function of the interactive elastic, viscoelastic, and the high temperature behaviors in the cutting region [68]. All this being said, in order to utilize this friction model in ABAQUS/Explicit, an external subroutine was programmed and linked to ABAQUS CAE. This proved to introduce various complications when linking the external compiler with the CAE model, and following successful execution, the cutting force results were affected by a negligible amount. Thus, the traditional Coulombs friction model is deemed adequately appropriate for modeling micromachining using EVASPC.

#### 4.8.6 ABAQUS Results and analysis

The ABAQUS/explicit models were used to obtain three primary results for comparison: The Von Mises stress distribution, the chip formation, and the Reaction Forces produced by cutting motion. First and foremost, Figure 4.28 illustrates a comparative depiction of the simulation results for conventional SPC (Figure 4.28(a)) and EVASPC cutting (Figure 4.28(b)).

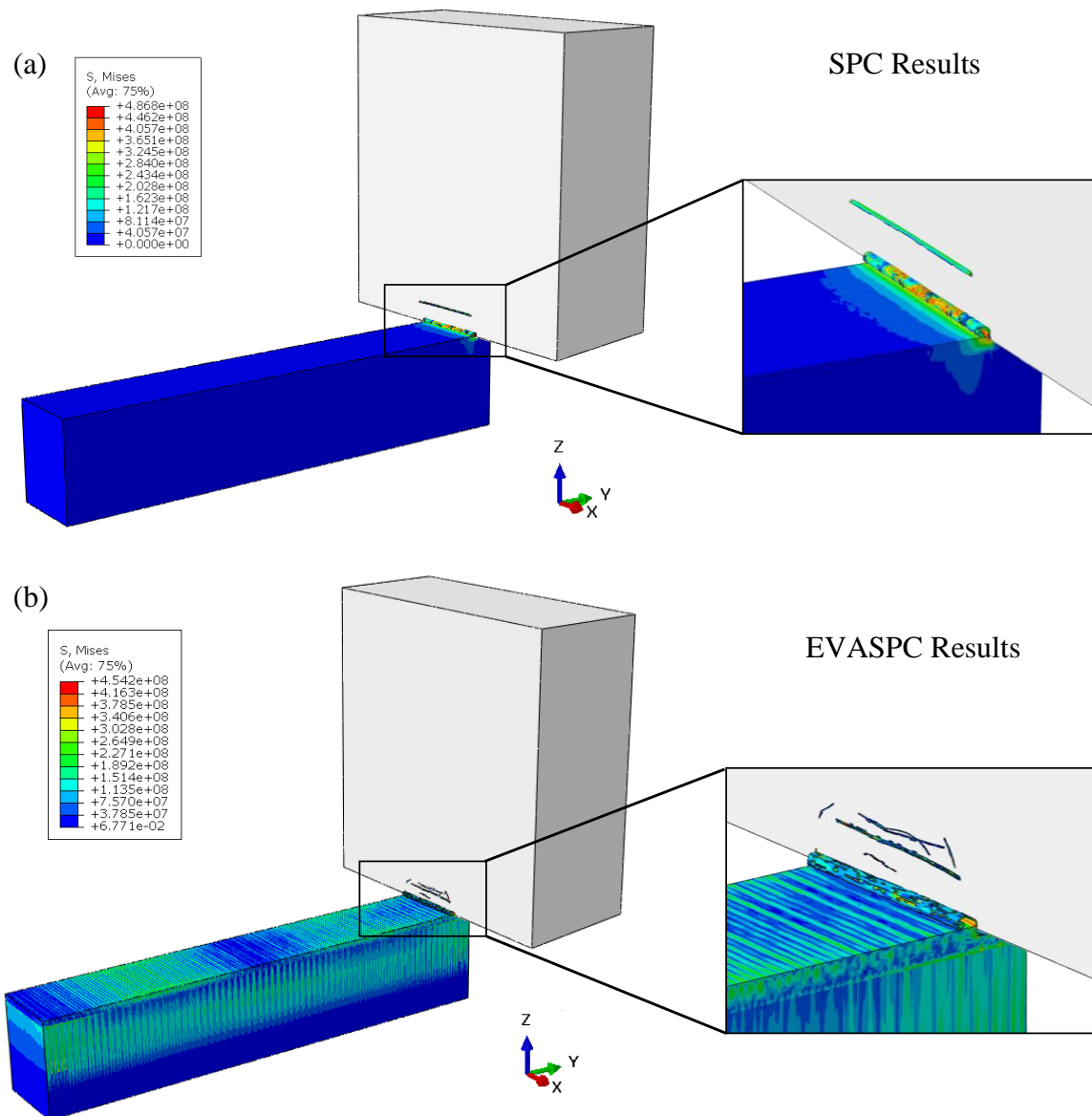


**Figure 4.28:** FEM simulation results.

Furthermore, the two simulations aim to mimic the comparison plot in Figure 4.12, in which the first simulation is done using CC, while the second simulation inherits EV amplitudes  $A_y = 2 \mu\text{m}$  and  $A_z = 2 \mu\text{m}$ . Both simulations were completed using the experimental parameters in Table 4.2, and contained the common process variables of DoC =  $10 \mu\text{m}$  and cutting speed,  $V_{\text{SPC}} = 1200 \text{ mm/min}$ .

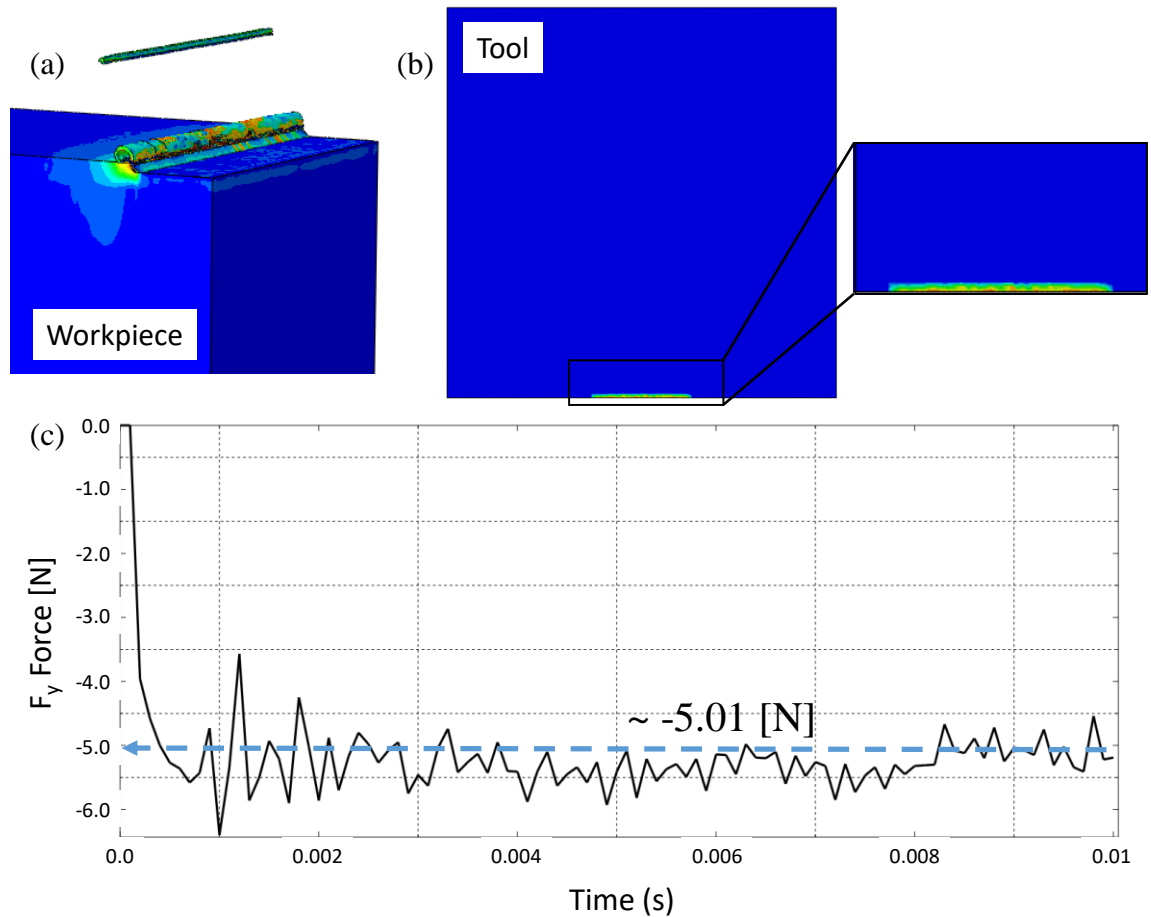


**Figure 4.29:** SPC FEM simulation results: (a) Workpiece, (b) cutting tool contact stress, and (c) cutting forces ( $F_y$ ).

The first simulation was done using conventional SPC in the absence of EVC, Figure 4.29. As hypothesized, a relatively continuous chip was produced, with the exception of a small sliver that was observed to separate, Figure 4.29(a). Through animation, this separation came as a result of initial contact between the tool and workpiece. This being said, the continuous behavior of the chip during SPC agreed with common machining theory, and chip fracture was ultimately triggered by the predefined

damage evolution parameters. Likewise, the corresponding contact stress distribution along the tool face demonstrated the minute contact area that contributes to overall cutting, Figure 4.29(b). Cutting force analysis showed acceptable compliance with experimental CC results. There is an initial spike due to high impact pressure followed by relatively constant force magnitude, generating an average of  $-5.01$  N (as opposed to the experimental magnitude,  $-5.14$  N). Ultimately, simulation results comply with experimental data and numerical force values lay well below 10% error, and are thus deemed acceptable for comparison.

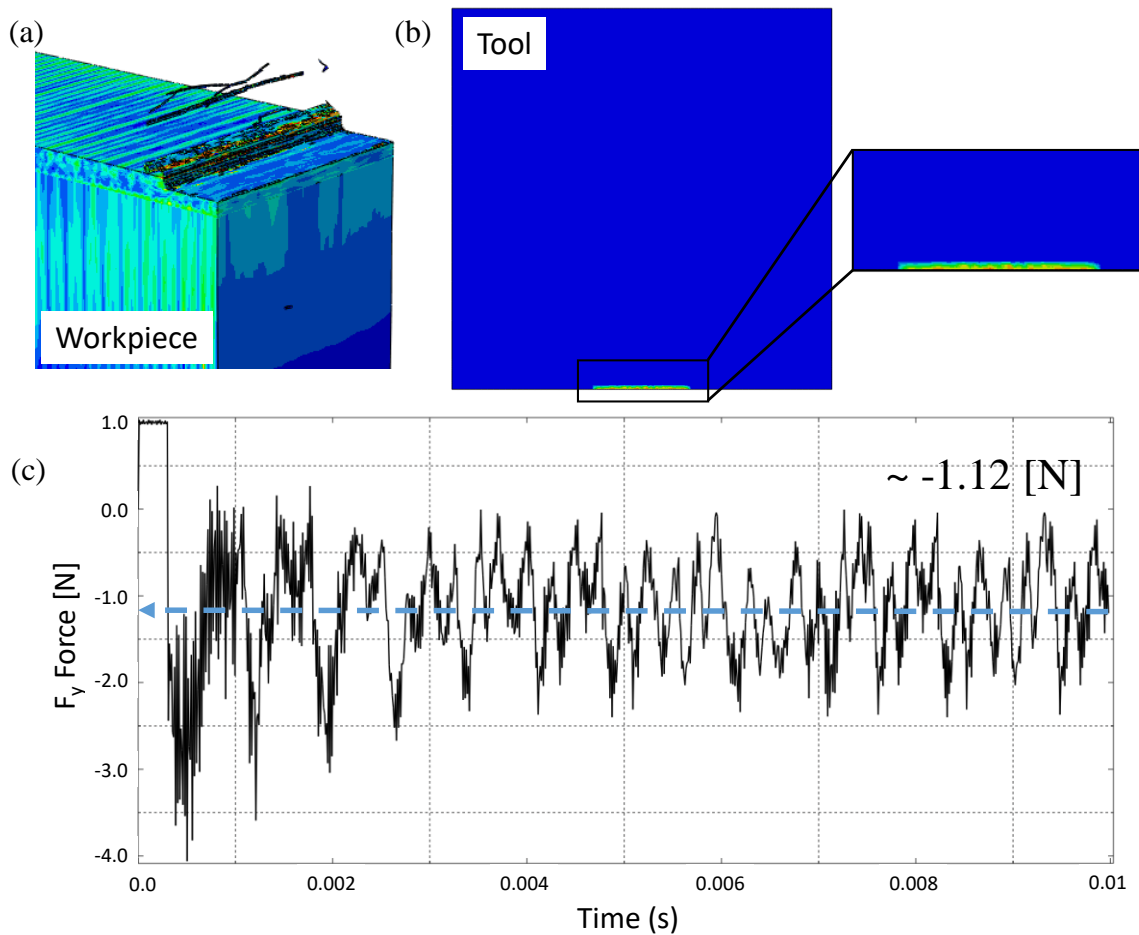


**Figure 4.30:** EVASPC FEM simulation results: (a) Workpiece, (b) cutting tool contact stress, and (c) cutting forces ( $F_y$ ).

Conversely, the second simulation consisted of the EVASPC experiment with EV amplitudes,  $A_y = 2 \mu\text{m}$  and  $A_z = 2 \mu\text{m}$ . The same general methods of analysis were done

on simulation results, however, the number of field output intervals was increased from 200 to 700 in order to observe EVC-induced force profiles. The intermittent contact between tool and workpiece generated discontinuous chip generation that was driven by mesh density, Figure 4.30(a). The model had some difficulties accurately generating the serrated chips discussed earlier, however Figure 4.30 moderately describes the EVC-induced chip formation. Furthermore, Figure 4.30(b) demonstrates a frozen frame snapshot of the EVC transient the contact stress depicted on the tool. On this note, the reduction in cutting forces is once again modeled following the introduction of EVC, as seen earlier in Figure 4.12. ABAQUS/explicit demonstrated average Reaction Forces ( $F_y$ ) of  $-1.12$  N (as opposed to the experimental magnitude,  $-1.27$  N), and additional force stability.

It should be noted however, that the simulation capabilities of this study were limited. For one, the preceding ABAQUS models neglected the appropriate friction and heating effects generated between the diamond tool and workpiece material interaction (which is one of primary reasons for the implementation of elliptical vibrations). Rather, the primary mechanism of analysis came from the influence that chip formation has on cutting forces when comparing traditional SPC to EVASPC. Another limitation came from the computing power available. The computer used for these simulations had 16 GB of RAM and a 3.40 GHz CPU. As a result, the computing time was quite extensive for a simulation time of 0.01 seconds. Both models used the automatic time step increment feature when defining the spacing between time steps. The conventional SPC simulation used 106,077 time increments (with average time step =  $3.05e-05$  sec), visualized with field output requests set to 200 intervals, resulting in 36,352 seconds of CPU time and nearly 16 hours of real time. On the other hand, the EVASPC simulation used 152,534 time increments (average time step =  $1.22e-05$  sec), and field output requests set to 700 intervals, resulting in 66,454 seconds of CPU time and 3 days and 4 hours of real time. The increase in data output resolution was used in the EVASPC simulation to observe cutting force characteristics throughout a single EV revolution, Figure 4.30(c), however due to software capabilities, computing time, and power these results were limited. All this being said, based on the current CAE setup, the simulation results were

considered acceptable, while further enhancements in mesh quality, cutting force plot resolution, and temperature effect would be desirable.

## 4.9 Summary and conclusions

This parametric study investigated the effects that elliptical vibration amplitudes have on cutting forces and surface topography for orthogonal EVASPC micromachining. For this purpose, fifteen EVASPC experiments were created to cover an array of ellipse shapes, from which point the average cutting forces and surface roughness were captured for each trial. These results were then used for comparative analysis, demonstrating how they change with the manipulation of EV amplitudes. The following conclusions were drawn from the cutting force analysis:

- The addition of high-frequency elliptical vibrations to orthogonal single point cutting demonstrated significant reduction in the  $F_y$  cutting force amplitude (> 75%). EVASPC also demonstrated enhanced cutting force stabilization when compared to ‘no-EVC’ cutting, reducing the deviation from 0.1651 N to 0.0125 N.
- The comparative analysis demonstrated that the EVC ellipse size is negatively related to the average cutting force. This observation was supported by the fact that the overall increase in horizontal amplitude ( $A_y$ ) possessed an  $F_y$  reduction of 33%, while the increase in vertical amplitude ( $A_z$ ) reduced cutting forces by 22%.
- Regression modeling demonstrated the functional dependence of EVC cutting parameters on resulting average cutting forces, from which point, ellipse area and the tool-workpiece engaged length proved to be the most significant predictors.

Similarly, the following conclusions were drawn from the surface roughness analysis:

- The comparative analysis demonstrated that the EV amplitude is, again, negatively related to the surface roughness ( $S_a$ ). This observation was supported by the fact that the overall increase in horizontal amplitude ( $A_y$ ) possessed an average  $S_a$  reduction of 30%. This being said, there was no such conclusions drawn from the vertical amplitude ( $A_z$ ).

- High-frequency elliptical vibration motions were transformed into high-frequency surface profiles, ultimately responsible for roughness formation. However, no such correlations between EVASPC and surface waviness formation were observed.
- Regression modeling demonstrated the functional dependence of EVC cutting parameters on resulting average surface roughness, from which the horizontal amplitude ( $A_y$ ) proved to be the most significant predictor—supporting the original hypothesis.

In summary, it is anticipated that this parametric study will provide a metric from which EVASPC process predictability and efficiency can be enhanced. In Addition, more refinement and validation in FEM modeling could assist in enhanced time and resource efficient analysis. Ultimately, the results above could constitute the premise of several new scientific directions related to deep learning-based analysis, optimization, and control of the cutting-based material removal at micro/nano-scale for surface functionality and/or optical surface quality

# Chapter 5

Summary, Conclusions, and Future Directions



## 5 Summary, Conclusions, and Future Directions

### 5.1 Summary and conclusions

The work outlined in this thesis aimed to develop a better understanding of the elliptical vibration assisted single point cutting process, characterized by the integration of traditional single point cutting with external elliptical vibration cutting. More specifically, this study aimed to provide further explanation of this technology through three pillars of investigation: (1) analytical modeling of EVASPC motion kinematics and cutting force mechanics, (2) experimental EVASPC cutting force analysis via V-groove fabrication, and (3) parametric study focused on EVC parameters (EV amplitudes) and their effect on the SPC process.

The first objective aimed to develop an overarching mathematical model of EVASPC tool motion trajectory through the summation of tool motion in the  $X$ ,  $Y$ , and  $Z$  directions. This ultimately established an intuitive understanding of the cutting process motion kinematics and the contribution provided by each cutting parameter. Furthermore, these governing equations of motion solidified the foundation upon which preliminary EVASPC implementations were conceived. It was observed that the EV amplitudes ( $A_y$  and  $A_z$ ) and cutting speed ( $V_{SPC}$ ) are relatively easy parameters to manipulate, introducing a large amount of flexibility to the cutting process that can alone influence the surface topographical profile and cutting force generation. Furthermore, a detailed explanation of the modified Merchant's Circle outlined the theoretical cutting forces reduction as a result of EVC, and was narrowed down to two key factors: (1) tool-workpiece material interaction via shear deformation properties, and (2) the influence that cutting parameters have on force vector orientations. Ultimately, these two analytical models—motion kinematics and cutting force model—lay the foundation for EVASPC implementations and applications, and provided the structural framework upon which the proceeding experimental methodologies were conceived.

Following the numerical modeling of EV-assisted SPC, the experimental fabrication of V-grooves was completed using an axial constant-area cutting strategy. The employment of this implementation revealed the dramatic cutting force reduction as a result of

high-frequency elliptical vibrations. The constant-area strategy demonstrated important reductions in the  $Y$ -force, as high as 92% (from  $\sim -1.86$  N to  $\sim -0.1029$  N), when comparing conventional no-EVC cutting to EVASPC. Additionally, experimental results revealed enhanced force stabilization for each cutting pass when transitioning from traditional CC to EVASPC as a result of the quasi-static cutting force components generated through the constant-area cutting strategy. This being said, there were other effects of force production that potentially contributed to the observed results: tool wear, chip removal, initial contact stress, and unpredictable tool-workpiece thermochemical reactions.

Following this, an extensive parametric study was developed to investigate the effects that EV amplitudes ( $A_y$  and  $A_z$ ) have on cutting forces and surface topography during orthogonal EVASPC micromachining. After completing the comparative analysis, it was determined that the ellipse size is inversely related to the average cutting force—as  $A_y$  and  $A_z$  increase, the cutting force ( $F_y$ ) decreases. Similarly, for the surface roughness ( $S_a$ ), a clear trend demonstrated that the horizontal amplitude ( $A_y$ ) provided the most consistent influence on  $S_a$ , whereas  $A_z$  presented unexplainable ambiguities. More specifically, as the  $A_y$  increased and the ellipse orientation became predominantly horizontal, the surface roughness decreased. These observations come as a result of the unique reduction in cyclical duty cycle defined by the tool trajectory (engaged time vs. total process time). Furthermore, these results were supported through the formulation of a regression model which demonstrated the functional dependence between input cutting parameters and output metrics (cutting forces and surface roughness). In addition, primitive FEM modeling was introduced to provide a supportive role in the validation of experimental results, with the future aim of reliably predicting untested scenarios.

## 5.2 Research limitations

While the experimental results throughout the preceding sections were insightful, there was one primary limitation regarding the discrepancy between elliptical vibration frequency of the cutting tool motion and the dynamometer sampling frequency. The sampling frequency provided by the Kistler 9256C-2 dynamometer (2 kHz) was much smaller than that of the EVASPC vibrational frequency (41 kHz); therefore, nearly one

data point was being captured for every 20 elliptical revolutions, detrimentally restricting the accuracy of the overall cutting force results. The transient cutting force profiles are unique to EVASPC and its ultra-high frequency periodic engagement between the tool and workpiece; therefore, the dynamometers limited sampling rate ultimately restricted the ability to consistently and predictably know which point along the force profile is being reflected in the captured data, which can inaccurately skew the results. However, at this time, there is no dynamometer with a sufficient sampling frequency capable of capturing multiple data points throughout an elliptical revolution, to the best of the authors knowledge.

However, it should be noted that, similar to existing studies, the dynamometer was placed on the workpiece side and not on the tool side of the experimental setup; therefore, this may be a reason for which the mismatch between frequencies is less important. If the dynamometer was placed on the tool side, the potential for additional dynamic vibrations and harmonic effects from the tool motion could produce convoluted results. However, with the dynamometer being placed under the workpiece, the forces are attenuated through the elastic properties of the workpiece material, and the analyzed results come from the forces translated to the workpiece, which is more representative of the overall cutting mechanisms.

Another limitation to the dynamometer sensing capabilities came through the calibration method used. Various calibration techniques, depending on the researcher, can affect the accuracy of the cutting force results. The calibration method used throughout this thesis remained constant, however, when attempting to compare results to existing literature there could be differences due to calibration and other systematic error.

Furthermore, it should be noted that a single test was completed for each experimental trial. This provides limited insight regarding repeatability, variability, and additional sources of dynamic process effects that could be influential to the cutting process. In order to make any meaningful conclusions regarding EVASPC's influence on single point diamond cutting additional investigation will be required. This being said, the

completed studies can demonstrate preliminary trends in cutting forces and surface quality for the tested experiments.

And, as mentioned in the FEM section, there were assumptions and simplifications that could be improved upon in future work. Primarily, the ABAQUS models neglected the friction and heating effects generated between the diamond tool and workpiece material, and relied solely on the chip formation for cutting force results. Additionally, the computer used for simulation provided a significant source of restriction; ultimately, reducing the computing power, meshing capabilities, and overall, negatively affecting the simulation runtime. While the produced simulation results were relatively acceptable, further enhancements in mesh quality, cutting force plot resolution, and temperature effect would be desirable.

### **5.3 Future directions**

While EVASPC can be extended in multiple directions, the analysis presented in this thesis constitute an important foundation upon which further development can be made. One immediate priority involves the repeatability and validation of the parametric study results in order to strengthen the predictive regression model. Furthermore, the expansion of the parametric study could develop a deeper understanding of EVC and its parameters; this could be done by testing alternative cutting parameters such as cutting speed, DoC, and phase shift.

On another note, analysis of tool performance could introduce additional insight into the effect EVC has on the single point cutting process. Diamond tool wear has demonstrated critical limitations in SPC processes for the fabrication of ferrous and hard-to-cut materials; therefore, analyzing the correlation between accumulated tool damage and output process metrics (cutting force generation and surface topography) would be a beneficial research path.

In addition, there are numerous improvements that can be made to the proposed FEM model. Currently, the FEM cutting forces generated between the diamond tool and aluminum workpiece stand within an acceptable range of accuracy, however, such results

could be improved. Such improvement could be obtained through mesh sensitivity analysis in order to ensure convergence of simulation results while maintaining modeling efficiency. On another note, the LuGre friction model (deemed the most appropriate for EVC) introduced complications into the modeling process and seemed to generate results that were relatively indistinguishable from the conventional Coulomb friction model. This being said, additional effort can be made when integrating and validating this LuGre model for EVASPC. Proceeding the above consideration, more future attention could be directed towards the testing of the additional cutting conditions that were not studied through experimental trials.

## References

- [1] Xiang, J., Xie, L., Gao, F., Yi, J., Pang, S., and Wang, X., 2018, "Diamond tools wear in drilling of SiCp/Al matrix composites containing Copper," *Ceramics International*, 44(5), pp. 5341-5351.
- [2] Zou, L., Huang, Y., Zhou, M., and Xiao, G., 2017, "Thermochemical wear of single crystal diamond catalyzed by ferrous materials at elevated temperature," *Crystals*, 7(4), p. 116.
- [3] Zou, L., Dong, G., and Zhou, M., 2013, "Investigation on frictional wear of single crystal diamond against ferrous metals," *International Journal of Refractory Metals and Hard Materials*, 41, pp. 174-179.
- [4] Skelton, R., 1969, "Surface finish produced by a vibrating tool during turning," *International Journal of Machine Tool Design and Research*, 9(4), pp. 375-389.
- [5] Skelton, R., 1969, "Effect of ultrasonic vibration on the turning process," *International Journal of Machine Tool Design and Research*, 9(4), pp. 363-374.
- [6] Shamoto, E., and Moriwaki, T., 1994, "Study on elliptical vibration cutting," *CIRP annals*, 43(1), pp. 35-38.
- [7] Tan, R., Zhao, X., Zou, X., and Sun, T., 2018, "A novel ultrasonic elliptical vibration cutting device based on a sandwiched and symmetrical structure," *The International Journal of Advanced Manufacturing Technology*, 97(1-4), pp. 1397-1406.
- [8] Saito, H., Jung, H., and Shamoto, E., 2016, "Elliptical vibration cutting of hardened die steel with coated carbide tools," *Precision Engineering*, 45, pp. 44-54.
- [9] Kim, G. D., and Loh, B. G., 2007, "Characteristics of elliptical vibration cutting in micro-V grooving with variations in the elliptical cutting locus and excitation frequency," *Journal of micromechanics and microengineering*, 18(2), p. 025002.
- [10] Milliken, N., Hamilton, B., Hussein, S., Tutunea-Fatan, O. R., and Bordatchev, E., 2018, "Enhanced bidirectional ultraprecise single point inverted cutting of right triangular prismatic retroreflectors," *Precision Engineering*, 52, pp. 158-169.
- [11] DeVries, W. R., 1991, *Analysis of material removal processes*, Springer Science & Business Media.
- [12] Rusinek, R., Wiercigroch, M., and Wahi, P., 2015, "Orthogonal cutting process modelling considering tool-workpiece frictional effect," *Procedia CIRP*, 31, pp. 429-434.
- [13] Obata, K., 2016, "Single-crystal diamond cutting tool for ultra-precision processing," *Sei Tech Rev*, 82, p. 83.

- [14] Shamoto, E., and Moriwaki, T., 1999, "Ultrprecision diamond cutting of hardened steel by applying elliptical vibration cutting," *CIRP Annals-Manufacturing Technology*, 48(1), pp. 441-444.
- [15] Davim, J. P., 2010, *Surface integrity in machining*, Springer.
- [16] Suzuki, N., Yokoi, H., and Shamoto, E., 2011, "Micro/nano sculpturing of hardened steel by controlling vibration amplitude in elliptical vibration cutting," *Precision Engineering*, 35(1), pp. 44-50.
- [17] Guo, P., Lu, Y., Ehmann, K. F., and Cao, J., 2014, "Generation of hierarchical micro-structures for anisotropic wetting by elliptical vibration cutting," *CIRP Annals*, 63(1), pp. 553-556.
- [18] Xia, D., Johnson, L. M., and López, G. P., 2012, "Anisotropic wetting surfaces with one-dimensional and directional structures: fabrication approaches, wetting properties and potential applications," *Advanced Materials*, 24(10), pp. 1287-1302.
- [19] Ionov, L., Houbenov, N., Sidorenko, A., Stamm, M., and Minko, S., 2006, "Smart microfluidic channels," *Advanced Functional Materials*, 16(9), pp. 1153-1160.
- [20] Bhushan, B., and Jung, Y. C., 2011, "Natural and biomimetic artificial surfaces for superhydrophobicity, self-cleaning, low adhesion, and drag reduction," *Progress in Materials Science*, 56(1), pp. 1-108.
- [21] Zhang, J., Cui, T., Ge, C., Sui, Y., and Yang, H., 2016, "Review of micro/nano machining by utilizing elliptical vibration cutting," *International Journal of Machine Tools and Manufacture*, 106, pp. 109-126.
- [22] Loewen, E. G., and Popov, E., 2018, *Diffraction gratings and applications*, CRC Press.
- [23] Fisher, M., and Burt, T., 2018, "Rapid, Automated, Quality Control Measurements of Diffraction Grating Efficiency," *Agilent Technologies*.
- [24] Yang, Y., Pan, Y., and Guo, P., 2017, "Structural coloration of metallic surfaces with micro/nano-structures induced by elliptical vibration texturing," *Applied Surface Science*, 402, pp. 400-409.
- [25] Yang, Y., and Guo, P., 2018, "Effect of elliptical vibration trajectories on grating structure formation and its application in structural coloration," *Procedia Manufacturing*, 26, pp. 543-551.
- [26] Yang, Y., and Guo, P., 2019, "Global tool path optimization of high-resolution image reproduction in ultrasonic modulation cutting for structural coloration," *International Journal of Machine Tools and Manufacture*, 138, pp. 14-26.

- [27] Ma, C., Shamoto, E., Moriwaki, T., and Wang, L., 2004, "Study of machining accuracy in ultrasonic elliptical vibration cutting," *International Journal of Machine Tools and Manufacture*, 44(12-13), pp. 1305-1310.
- [28] Zhang, X., Kumar, A. S., Rahman, M., Nath, C., and Liu, K., 2012, "An analytical force model for orthogonal elliptical vibration cutting technique," *Journal of manufacturing processes*, 14(3), pp. 378-387.
- [29] Bai, W., Sun, R., Gao, Y., and Leopold, J., 2016, "Analysis and modeling of force in orthogonal elliptical vibration cutting," *The International Journal of Advanced Manufacturing Technology*, 83(5-8), pp. 1025-1036.
- [30] Merchant, M. E., 1945, "Mechanics of the metal cutting process. I. Orthogonal cutting and a type 2 chip," *Journal of applied physics*, 16(5), pp. 267-275.
- [31] Shamoto, E., and Moriwaki, T., 1999, "Ultraprecision diamond cutting of hardened steel by applying elliptical vibration cutting," *CIRP Annals*, 48(1), pp. 441-444.
- [32] Joao, D., Milliken, N., Bordatchev, E. V., and Tutunea-Fatan, O. R., 2019, "Axial strategy for ultraprecise single point cutting of V-grooves Case 1: constant chip thickness," *Procedia Manufacturing*, 34, pp. 440-445.
- [33] Zhang, J., Suzuki, N., and Shamoto, E., 2013, "Investigation on machining performance of amplitude control sculpturing method in elliptical vibration cutting," *Procedia Cirp*, 8, pp. 328-333.
- [34] Zhang, J., Suzuki, N., Wang, Y., and Shamoto, E., 2015, "Ultra-precision nano-structure fabrication by amplitude control sculpturing method in elliptical vibration cutting," *Precision Engineering*, 39, pp. 86-99.
- [35] Guo, P., and Ehmann, K. F., 2013, "An analysis of the surface generation mechanics of the elliptical vibration texturing process," *International Journal of Machine Tools and Manufacture*, 64, pp. 85-95.
- [36] Zakovorotny, V., and Bordatchev, E., "Prediction and Diagnostics of Work Piece Machining Quality in Machine Tools, Based on Dynamic Simulation," *Proc. Proceedings of the Thirty-First International Matador Conference*, Springer, pp. 315-320.
- [37] Bordatchev, E. V., and Orban, P. E., "Machining process as a subject of automatic control," *Proc. Sensors and Controls for Intelligent Machining and Manufacturing Mechatronics*, International Society for Optics and Photonics, pp. 57-66.
- [38] Moriwaki, T., Suzuki, H., Mizugaki, J., Maeyasu, Y., Higashi, Y., and Shamoto, E., "Ultraprecision cutting of Molybdenum by ultrasonic elliptical vibration cutting," *Proc. Proceedings of the 19th annual meeting of the ASPE*, Orlando, USA, pp. 621-624.



- [39] Kim, G. D., and Loh, B. G., 2010, "Machining of micro-channels and pyramid patterns using elliptical vibration cutting," *The International Journal of Advanced Manufacturing Technology*, 49(9-12), pp. 961-968.
- [40] Klocke, F., 2011, *Manufacturing Processes 1: Cutting*, Springer.
- [41] Kolar, P., Fojtu, P., and Schmitz, T., 2015, "On cutting force coefficient model with respect to tool geometry and tool wear," *Procedia Manufacturing*, 1, pp. 708-720.
- [42] Kai-Uwe Sattler, D. C. N., Ngoc Pi Vu, Banh Tien Long, Horst Puta, 2019, *Advances in Engineering Research and Applications: Proceedings of the International Conference on Engineering Research and Applications, ICERA 2019*, Springer.
- [43] Lin, C.-Y., Su, C.-H., Hsu, C.-M., and Lin, C.-R., 2008, "Improvement of the microcrystalline cube corner reflective structure and efficiency," *Japanese Journal of Applied Physics*, 47(7R), p. 5693.
- [44] Chen, Y.-C., Nian, S.-C., and Huang, M.-S., 2016, "Optical design of the Fresnel lens for LED-driven flashlight," *Applied optics*, 55(4), pp. 712-721.
- [45] Wei, A.-C., Hsiao, S.-Y., Sze, J.-R., and Lee, J.-Y., 2019, "V-groove and parabolic array for enlarging the acceptance angle of a side-absorption concentrated photovoltaic system," *Optics & Laser Technology*, 112, pp. 426-435.
- [46] Luo, Y., Liu, Y., Anderson, J., Li, X., and Li, Y., 2015, "Improvement of water-repellent and hydrodynamic drag reduction properties on bio-inspired surface and exploring sharkskin effect mechanism," *Applied Physics A*, 120(1), pp. 369-377.
- [47] Abdulbari, H. A., Mahammed, H. D., and Hassan, Z. B., 2015, "Bio-Inspired Passive Drag Reduction Techniques: A Review," *ChemBioEng Reviews*, 2(3), pp. 185-203.
- [48] Brinksmeier, E., Gläbe, R., and Schönemann, L., 2012, "Review on diamond-machining processes for the generation of functional surface structures," *CIRP Journal of Manufacturing Science and Technology*, 5(1), pp. 1-7.
- [49] Zhao, Z. L., Yu, H. P., Wu, D. M., Liu, Y., Zheng, X. T., Zhuang, J., and Jing, P. S., "Research on the Key Technology in Ultra-Precision Machining of Optical Micro V-Groove Mold Roller," *Proc. Advanced Materials Research, Trans Tech Publ*, pp. 1563-1567.
- [50] Moriya, T., Nakamoto, K., Ishida, T., and Takeuchi, Y., 2010, "Creation of V-shaped microgrooves with flat-ends by 6-axis control ultraprecision machining," *CIRP annals*, 59(1), pp. 61-66.
- [51] Forfang, W. B. D., Conner, T. G., You, B. H., Park, T., and Song, I.-H., 2014, "Fabrication and characterization of polymer microprisms," *Microsystem technologies*, 20(10-11), pp. 2071-2077.

- [52] To, S., and Zhang, G., 2014, "Study of cutting force in ultra-precision raster milling of V-groove," *The International Journal of Advanced Manufacturing Technology*, 75(5-8), pp. 967-978.
- [53] Guo, J., Zhang, J., Wang, H., Liu, K., and Kumar, A. S., 2018, "Surface quality characterisation of diamond cut V-groove structures made of rapidly solidified aluminium RSA-905," *Precision Engineering*, 53, pp. 120-133.
- [54] Li, Z., Fang, F., Gong, H., and Zhang, X., 2013, "Review of diamond-cutting ferrous metals," *The International Journal of Advanced Manufacturing Technology*, 68(5-8), pp. 1717-1731.
- [55] Kim, G. D., and Loh, B. G., 2007, "Characteristics of chip formation in micro V-grooving using elliptical vibration cutting," *Journal of micromechanics and microengineering*, 17(8), p. 1458.
- [56] Son, S.-M., Lim, H.-S., Paik, I.-H., and Ahn, J.-H., 2003, "A study on critical depth of cuts in micro grooving," *KSME international journal*, 17(2), pp. 239-245.
- [57] Lee, J.-M., Je, T.-J., Choi, D.-S., Lee, S.-W., Le, D., and Kim, S.-J., 2010, "Micro grooving simulation and optimization in the roughing stage," *International Journal of Precision Engineering and Manufacturing*, 11(3), pp. 361-368.
- [58] Joao, D., Milliken, N., Tutunea-Fatan, O. R., and Bordatchev, E. V., 2019, "One-Side Cutting Strategy for Ultraprecise Single Point Cutting of V-grooves Case 1: Constant Chip Thickness," *IFAC-PapersOnLine*, 52(10), pp. 306-310.
- [59] Farris, N., Joao, D., Milliken, N., Tutunea-Fatan, O. R., and Bordatchev, E., 2020, "Reduction of cutting forces by elliptical vibration in multi-pass ultraprecise single point axial cutting of V-grooves," *Procedia Manufacturing*, 48, pp. 570-578.
- [60] Lin, J., Guan, L., Lu, M., Han, J., and Kan, Y., 2017, "Modeling and analysis of the chip formation and transient cutting force during elliptical vibration cutting process," *AIP Advances*, 7(12), p. 125101.
- [61] Xu, W.-X., and Zhang, L.-C., 2015, "Ultrasonic vibration-assisted machining: principle, design and application," *Advances in Manufacturing*, 3(3), pp. 173-192.
- [62] ABAQUS, I., 2005, "Overview of ABAQUS/Explicit."
- [63] Opoz, T. T., and Chen, X., 2016, "Chip formation mechanism using finite element simulation," *Strojniški vestnik-Journal of Mechanical Engineering*, 62(11).
- [64] Akram, S., Jaffery, S. H. I., Khan, M., Fahad, M., Mubashar, A., and Ali, L., 2018, "Numerical and experimental investigation of Johnson–Cook material models for aluminum (Al 6061-T6) alloy using orthogonal machining approach," *Advances in Mechanical Engineering*, 10(9), p. 1687814018797794.

- [65] Systemes, D., 2014, "Abaqus 6.14: Abaqus/CAE User's Guide," Providence, USA.
- [66] Markopoulos, A., and Manolakos, D., 2010, "Finite element analysis of micromachining," *J Manuf Technol Res*, 2(1-2), pp. 17-30.
- [67] Nosouhi, R., Behbahani, S., Amini, S., and Khosrojerdi, M., 2014, "Experimental and analytical study of the elliptical vibration-assisted turning process with the dynamic friction model," *Proceedings of the Institution of Mechanical Engineers, Part B: Journal of Engineering Manufacture*, 228(6), pp. 837-846.
- [68] Nosouhi, R., Behbahani, S., Amini, S., and Khosrojerdi, M. R., 2016, "Development of a New Dynamic Friction Model for Analytical Modeling of Elliptical Vibration Assisted Turning Process," *Journal of Modern Processes in Manufacturing and Production*, 5(3), pp. 69-78.

## Curriculum Vitae

**Name:** Nikolai Farrus

**Post-secondary Education and Degrees:** Western University  
London, Ontario, Canada  
2014-2018 B.E.Sc.

Western University  
London, Ontario, Canada  
2018-2020 M.E.Sc.

**Honours and Awards:** Dean's Honor List  
2016-2017, 2017-2018

Western University Athletic-Scholar Award  
2016-2017, 2017-2018, 2018-2019

**Related Work Experience:** Teaching Assistant  
Western University  
2018-2020

Research Assistant  
Western University  
2018-2020

### Publications:

**Farrus, N.,** Milliken, N., Tutunea-Fatan, O.R., & Bordatchev, E. V. (2020). Parametric Analysis of EVASPC Characteristics and their Effect on Process Performance. Submitted in Aug. 2020 to *The International Journal of Advanced Manufacturing Technology*.

**Farrus, N.,** Tutunea-Fatan, O.R., & Bordatchev, E. V. (2019). CAD/CAM Framework for Generation of Surface Microstructures through Elliptical Vibration Assisted Single Point Cutting. Accepted for publication in *Computer-Aided Design and Applications*.

**Farrus, N.,** Joao, D., Milliken, N., Tutunea-Fatan, O.R., & Bordatchev, E. V. (2019). Reduction of cutting forces by elliptical vibration in multi-pass ultraprecise single point axial cutting of V-grooves. *Procedia Manufacturing*, 48, pp. 570-578.

**Farrus, N.,** Tutunea-Fatan, O.R., Bordatchev, E.V., 2020, "Framework for Determination of Surface Topography Generated Through Elliptical Vibration Assisted Single Point Cutting," *Proceedings of the CAD'20 Conference*, Jul. 2020, Barcelona, Spain, pp. 209-213.

**Farrus, N.,** Milliken, N., Tutunea-Fatan, O.R., & Bordatchev, E. V., 2019, Implementations and Applications of Elliptical Vibration Micro/Nano-Cutting. USB Proceedings of the 2019 International Congress of Canadian Society for Mechanical Engineering (CSME 2019), June 2019, Canada, pp. 149.